1974

A comparative analysis of the capabilities of three stereo radar techniques when operating in the presence of system errors

George L. Bair

Department:

A COMPARATIVE ANALYSIS OF THE CAPABILITIES OF THREE STEREO RADAR TECHNIQUES WHEN OPERATING IN THE PRESENCE OF SYSTEM ERRORS

BY

GEORGE LESLIE BAIR, JR., 1948-

A THESIS

Presented to the Faculty of the Graduate School of the

UNIVERSITY OF MISSOURI-ROLLA

In Partial Fulfillment of the Requirements for the Degree

MASTER OF SCIENCE IN ELECTRICAL ENGINEERING

1974

Approved by


(Advisor)


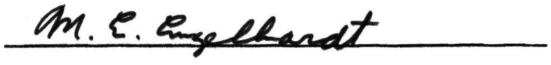

ABSTRACT

Three stereo radar techniques for producing stereo images from which topographic data and maps may be obtained are described and their performance in the presence of system errors is determined. The techniques are: an improved single flight technique which uses a combination of two antenna beam characteristics which permits terrain illumination from nearly the same aircraft position, a previously proposed single flight technique which uses two horizontal linear arrays generating vertical fan beams at different azimuth angles, and an existing two flight technique which uses a horizontal array generating a side-looking fan beam.

Error analyses are performed to determine the feasibility of the two single flight techniques. Comparisons are made of the error performance of all three techniques.

The analyses show that: (1) both single flight techniques are feasible and could be employed using present day state-of-the-art sensing devices, (2) the most significant error sources for the single flight techniques are the aircraft angular errors, conical beam cone angle error, and imaging errors, while the two flight technique is in general most sensitive to aircraft position and ranging errors, (3) the improved single flight technique has the best performance with errors and the previously proposed single flight technique performs better than the two flight technique when errors are present.

ACKNOWLEDGEMENT

The research covered by this thesis was performed by the author as a research assistant to Dr. Gordon E. Carlson at the University of Missouri-Rolla and was supported by the Office of Naval Research under Contract NOOl4-69-A-0141-008, Task NR387-069, entitled "Single Flight Stereo Radar." The author wishes to express his sincere gratitude to Dr. Gordon E. Carlson for helpful counsel and guidance during the course of this work.

TABLE OF CONTENTS

Table of Contents (Continued)

LIST OF ILLUSTRATIONS

List of Illustrations (Continued)

List of Illustrations (Continued)

List of Illustrations (Continued)

List of Illustrations (Continued)

Figure Page

LIST OF TABLES

I. INTRODUCTION

Topographic maps are maps which describe the surface of the earth in relief. This makes the hills, valleys, plains, and other natural features recognizable and locatable by both orthographic location and elevation. Maps of this type were originally devised to meet military needs for maps which could accurately portray the terrain.[1] Since their early introduction, topographic maps have been used extensively by engineers in planning highway and railroad locations. Geologists have also found them invaluable for mapping the distribution of rock formations and mineral resources and for searching for new mineral deposits. Other major uses of topographic maps include preparation of aeronautical charts, planning hydroelectric, flood control, drainage, and many other major construction projects. State and Federal agencies use topographic maps as an aid in forestry, reclamation, and related projects.[2]

Topographic maps were originally produced from data taken by field surveys. Since the development of aerial photography during the 1920's, the aerial photograph has become one of the important sources from which present day topographic maps are constructed. A single aerial photograph does not constitute a map. There is no height information and the perspective view shown on the aerial photograph is not the same as the orthographic projection of the terrain. To obtain information necessary for the production of

topographic maps from vertical aerial photographs it is necessary to take several succesive overlapping photographs. The adjacent overlapping areas of two photographs possess differential image displacement (parallax) and constitute a stereo pair. This stereo pair can be viewed using photogrammetric instruments to obtain a stereoscopic image from which terrain orthographic location and height measurements can be made.

In recent years airborne radar has been brought into use as an aid to producing topographic maps. As with aerial photography, it is possible to combine two radar images to form a stereo pair suitable for viewing stereoscopically and for obtaining terrain orthographic location and height measurements. It is unlikely that airborne radar methods will progress to the point where they supersede the use of aerial photography for producing topographic maps, but this is not the primary purpose for the present research and development effort for radar mapping techniques. Airborne radar is currently used as a supplement to aerial photography.

There are applications for which airborne radar is better suited than aerial photography for producing topographic maps and data. For about five million square miles of the earth's surface, the weather conditions are such that little or no photographic mapping data can be obtained. These areas are generally in tropic latitudes, and radar may be the only means by which complete mapping coverage can be obtained.[3,4] The recognition of terrain features on

aerial photographs is based on the actual counterparts of the images. In contrast, the appearance of radar images is based primarily on the reflective properties of the materials comprising the terrain. This enables the trained observer to obtain not only topographic data but also unique geological data from radar images.[5] Airborne radar methods also have the advantage of aiding the military in obtaining topographic map data in order to obtain immediate update in contingency or critical areas and for crisis management even when weather or light conditions are not satisfactory for aerial photography.[4]

The first attempts at using airborne radar in mapping applications were early small-scale charts compiled from low resolution plan-position indicator (PPI) radars in the late 1940's. These charts are not topographic maps but the possibility of obtaining the topographic data to construct such maps was immediately realized. Attempts were made to obtain the visual stereo effect with the radar images as had been done with aerial photography. However, most of these attempts used radar images produced primarily for unrelated purposes which were not very satisfactory for stereo viewing.

Beginning in the early 1960's, attention was focussed on the possibility of developing a radar system primarily for the purpose of obtaining topographic data from radar imagery.[6] Work continued and at the present time there is at least one airborne radar mapping system designed primarily for acquisition of stereo radar images to be used

specifically for obtaining topographic data and constructing topographic maps.[7,8]

The radar system currently available for stereo radar data acquisition uses a single side-looking airborne radar (SLAR) to obtain the radar images. The system is comprised of an aircraft to which a long narrow array antenna is attached. The antenna is mounted beneath the aircraft and lies along the flight path. The antenna produces a radar beam which is very narrow in the azimuth direction and planar in the vertical direction (vertical fan beam). The terrain is scanned by the aircraft motion. Two flights are made past the terrain being mapped. The flight paths are parallel and the flights are flown in such a manner that each portion of the terrain is illuminated twice by the radar and the distance from the aircraft to the terrain (stand-off distance) for each illumination is different. The flights are flown at different stand-off distances in order to obtain images which possess parallax and thus constitute a stereo pair. The two images, when properly processed, can be viewed in a manner similar to that used for aerial photographs to obtain a stereoscopic image from which terrain orthographic location and height measurements can be made.

The method of stereo radar mapping described above has been used successfully but it possesses several distinct disadvantages. The primary disadvantage is the requirement for double flight coverage. This requires twice the man hours, equipment use, and time required by aerial photography

techniques. This also introduces the problem of synchronizing the aircraft position and flight path between adjacent flights. The two images must be obtained at significantly different stand-off distances in order to obtain the parallax information necessary to the determination of terrain height information. This introduces the problem of illumination of the terrain at different illumination angles and causes two types of degradation in the radar images. First, the radar shadows of the two images comprising the stereo pair are quite different. This results in a reduction of the information available from the imagery and makes stereoscopic viewing difficult. Secondly, the difference in illumination angle results in different backscatter characteristics for each image which reduces image quality and viewability.

Two single flight techniques for obtaining stereo radar images have been proposed. The first of these techniques uses two vertical fan beam antennas mounted on a single aircraft at different azimuth angles to generate images containing the image parallax necessary for obtaining topographic data and maps. The method is an improvement over the presently implemented method in that it requires only a single flight past the terrain being mapped. However, this is the only improvement since illumination angles are significantly different for each image of the stereo pair and so the degradations mentioned above are still present. The other single flight technique for obtaining stereo radar

image pairs uses a unique combination of two different radar antenna beams mounted aboard an aircraft to obtain stereo radar pairs.[9] The system is designed in a manner such that portions of the terrain are illuminated from very nearly the same aircraft location. This results in radar shadow and backscatter characteristics which are nearly identical for each of the images comprising the stereo pair. This technique is also capable of improved image registration.

A distinction must be made between the two single flight techniques. This is done by denoting the technique which uses two vertical fan beams at different azimuth angles as the previous single flight technique and the technique which uses a combination of two different antenna beam patterns as the improved single flight technique.

An analysis of the characteristics and capabilities of the improved single flight technique has been performed and a comparison of the theoretical operating capabilities of the three stereo radar techniques has been made.[10,11] These analyses show that the improved single flight technique is theoretically capable of producing stereo images which are easier to interpret and view stereoscopically than the existing two flight and previous single flight techniques, while maintaining improved performance characteristics.

The primary purpose of this study is a comparative analysis of the capability of the three stereo radar techniques when operating in the presence of system errors. Of interest is the feasibility of the two proposed stereo radar

mapping techniques from a practical standpoint when operating with system errors present. Also of importance is the comparison of the capabilities of the three stereo radar mapping techniques with errors present. These feasibility and comparison analyses are accomplished by means of a computer simulation in which a generalized solution for the radar imagery of each of the three techniques, including the effects of all errors, is used. From this simulation, sensitivities are determined for each terrain point coordinate with respect to each individual error. The errors are assumed random and statistically independent and values for error standard deviations are assigned according to currently available equipment and sensor capabilities. These assumed error values are used with the sensitivity values to obtain the resulting standard deviations of the terrain image orthographic location and height coordinates.

To accomplish this task the analysis is carried out in the following manner:

1. Stereo radar image geometry and characteristics are discussed and each of the three stereo radar techniques are described.

2. The types of system errors which can occur are analyzed and a general set of errors applicable to any radar mapping technique is defined.

3. A generalized set of system equations including the effect of errors is developed for each of the stereo radar techniques.

4. Reconstruction of terrain coordinates from radar image data is considered for each of the radar techniques. Sets of equations to perform the reconstruction are developed, a criterion is established for, and a choice is made of the best reconstruction equations.

5. Computer programs are developed and determination is made of the overall system sensitivities to errors for each of the radar techniques.

6. A comparison of the overall system accuracy of the three stereo radar techniques is made.

II. REVIEW OF RELATED LITERATURE

The literature essential to the analysis of this thesis topic can be categorized into four main areas. These areas are radar theory, radargrammetry (the science of obtaining reliable measurements by means of radar), photogrammetry (the science of obtaining reliable measurements by means of photography), and stereo radar mapping.

Only a limited knowledge of radar theory is necessary for much of this analysis and so only the very essential radar characteristics and terminology are considered. There are many books available which are devoted to radar theory and application. Thorough treatments of all radar theory necessary to this analysis are presented in Refs. 12 and 13.

The methods of radargrammetry are vital to considering radar mapping techniques. A detailed account of this subject is available in Ref. 14. Of particular importance to this analysis are the discussions of relief displacement, radar parallax, and error sources which are contained in this book.

There are many similarities between stereo radar and aerial photography mapping techniques and so some knowledge of photogrammetric methods is an aid to working with stereo radar. All aspects of aerial photography, analytic photogrammetric methods, stereoscopy (the science which deals with stereoscopic effects, and the methods by which they are produced), and topographic map construction are covered in Ref. 1. Much of this material is directly applicable

to the stereo radar techniques which are considered in this analysis. An excellent treatment of radar mapping techniques is also given in Ref. 1.

There are no formal texts available on stereo radar mapping. The primary sources of information on this subject are journal articles, conference proceedings, and advertising literature. Journals which frequently contain articles on stereo radar analysis and applications are Photogrammetric Engineering[3,6] and IEEE Transactions on Geoscience Electronics.[9,15] Conferences which deal with photogrammetry, remote sensing, aerospace, and geology are likely to have presentations given concerning radar mapping and applications.[4,16] At least one company is presently operating a stereo radar mapping system and distributes literature describing their system's operation and capabilities.[7] Another company has a radar system capable of producing stereo radar imagery although this is not the system's primary purpose and also distributes literature describing their system's performance.[8]

The primary source of reference for this analysis are Refs. 10 and 11. These two reports are the result of a research program performed by the author and Dr. Gordon E. Carlson, University of Missouri-Rolla. These reports contain a requirements analysis and feasibility study of the improved single flight stereo radar technique and a comparative analysis of the three stereo radar mapping techniques. This thesis is an outgrowth of this work.

III. STEREO RADAR IMAGE CHARACTERISTICS

Radar theory and characteristics of imaging radars must be considered briefly prior to discussing the specific techniques for obtaining stereo radar images. Only the most essential points are covered here. For a more detailed analysis of these topics refer to Refs. 12 and 13. After presentation of the basic concepts in the first part of this section, a detailed description of each stereo radar technique is presented.

A. RADAR THEORY AND IMAGING RADAR CHARACTERISTICS

A block diagram of a typical imaging radar system is shown in Fig. 1. The components perform the following functions:

1. The pulse generator produces a steady train of pulses which drive the transmitter and synchronize the sweep generator with the transmitted pulse.

2. The transmitter converts each pulse from the pulse generator into a burst of radio-frequency (RF) energy.

3. The duplexer acts as a switch and connects the transmitter to the antenna during the period of transmission, and connects the receiver to the antenna for the rest of the time.

4. During transmission the antenna focusses the RF energy provided by the transmitter and radiates it into space in a narrow, shaped beam.

5. The receiver detects and amplifies the backscattered

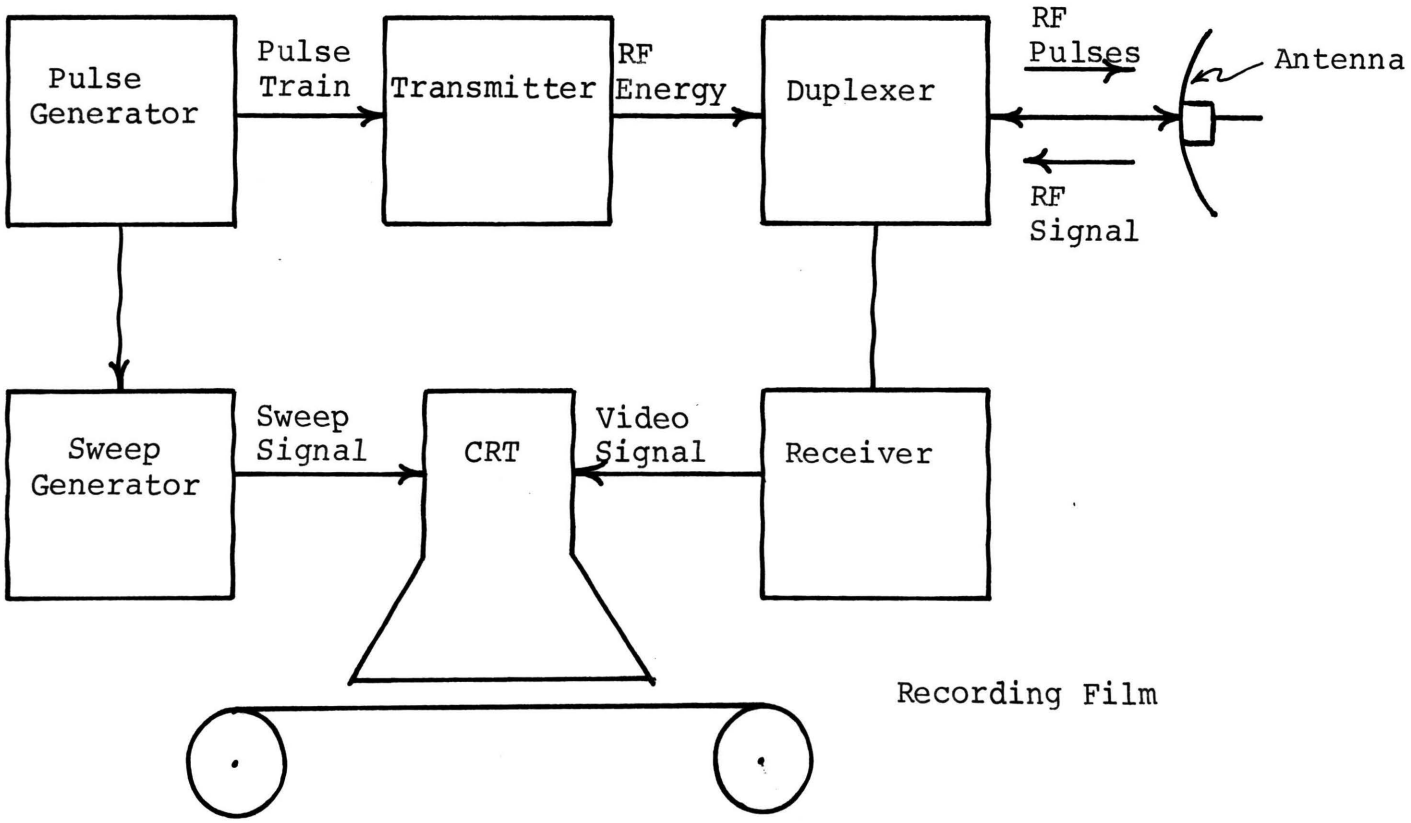

Fig. 1 Block Diagram of an Imaging Radar System

radar energy from the terrain and provides a video signal to the cathode ray tube (CRT). This signal is proportional to the intensity of the backscattered radar energy.

6. The sweep generator produces a voltage sweep, in synchronization with the pulse generator, which is linear or nonlinear as required, to drive the CRT display.

7. The CRT display produces a range trace for each pulse by modulating the intensity of an electron beam by the video output of the receiver and using the sweep signal from the sweep generator to position the electron beam.

8. The recording film is rolled past the CRT display, in synchronization with the aircraft's forward motion, and forms a permanent image of the radar return.

To obtain radar imagery the aircraft is flown past the terrain as shown in Fig. 2. This figure shows illumination for an imaging radar using a nearly side-looking vertical fan beam antenna. Fig. 3 gives a more detailed elevation view in the illumination plane showing the way a pulse of RF energy propagates radially, within the antenna beam, and strikes the terrain. When the pulse of energy strikes the terrain it is scattered and a portion of it is backscattered in the direction of the radar antenna. The figure shows the backscatter from the terrain segment A-A' (the terrain segment is also shown in Fig. 2). The return signal is detected by the radar receiver and converted to a video signal. The resulting range trace produced by the CRT display and recorded by the photographic film contains the

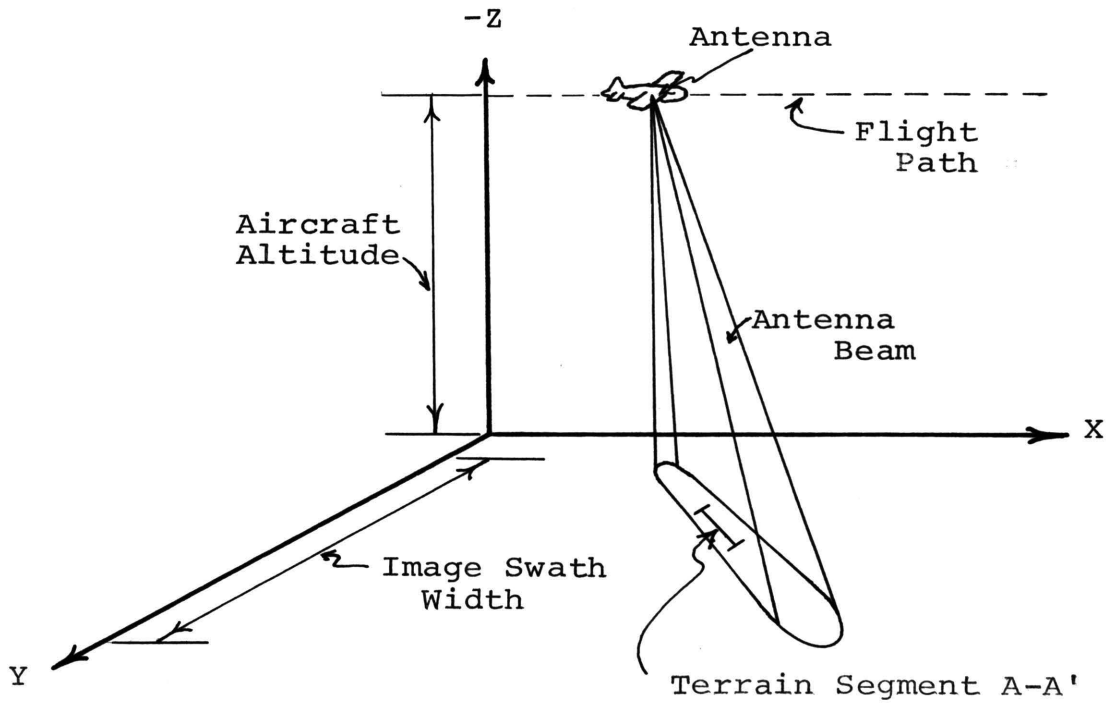

Fig. 2 Geometry for a Nearly Side-Looking Imaging Radar

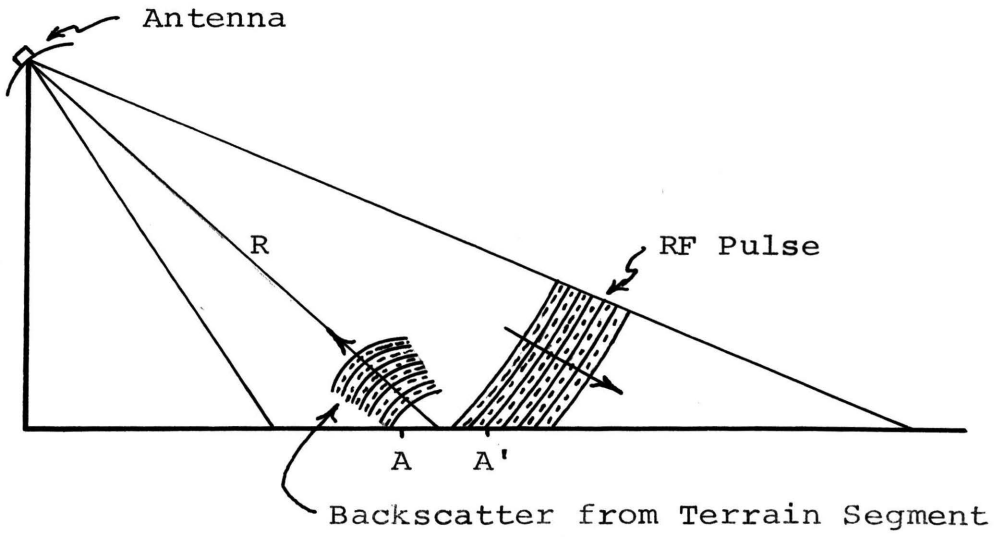

Fig. 3 Elevation View in the Illumination Plane Showing RF Pulse and Backscatter Return

information describing R, the slant range to the terrain segment A-A', and the aircraft location when the terrain segment is illuminated. A more convenient method of representing terrain points and the resulting information obtained when they are illuminated by imaging radars is the use of the flagpole target. This technique is used extensively in the sections that follow and an example is shown in Fig. 4.

An example to clarify the discussion of imaging radar characteristics is given in Fig. 5. For simplicity, a system using a side-looking vertical fan beam antenna is assumed. Several terrain points (A_1, A_2, and A_3) are shown. Note that terrain point A_1 is located on the reference plane, A_2 is elevated, and A_3 is depressed. The resulting radar image is shown in Fig. 6. A linear range sweep has been used to display the radar return and the radar image is shown at the same scale as that of Fig. 5. Note that since the antenna used is side-looking and a vertical fan beam, the terrain point orthographic along-track location corresponds to the aircraft position during illumination. It should also be noted that the radar return is shown in slant-range coordinates, i.e., the terrain point cross-track dimension does not correspond to the true orthographic location and thus corresponds to a nonconstant image scale. The nonconstant image scale can be corrected for terrain on a flat reference plane and the image presented in ground-range coordinates by using a nonlinear sweep after acquisition. This format leads to a more satisfactory presentation of radar images.

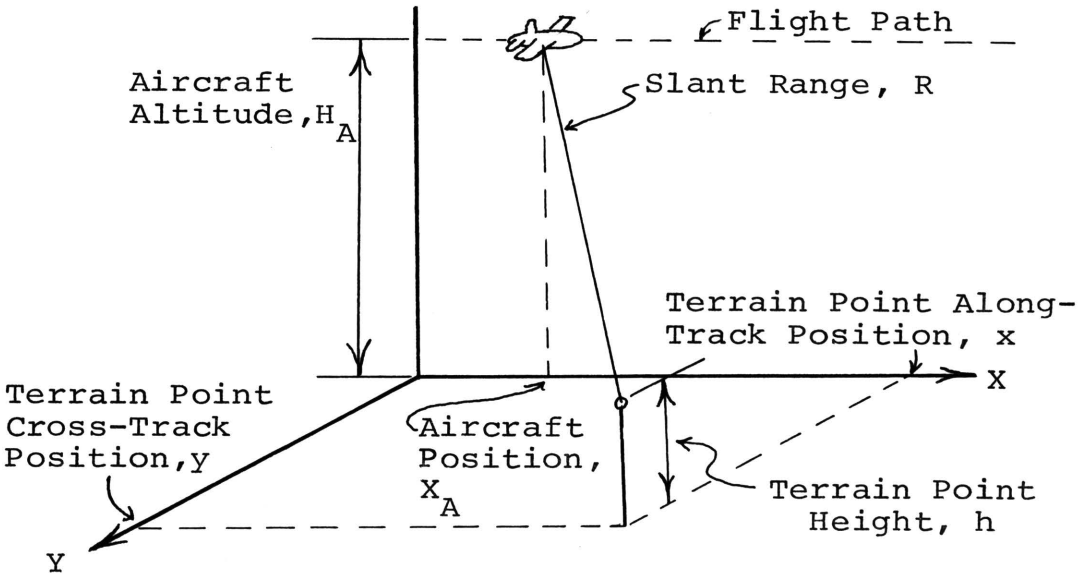

Fig. 4 Imaging Radar Illumination of the Flagpole Target

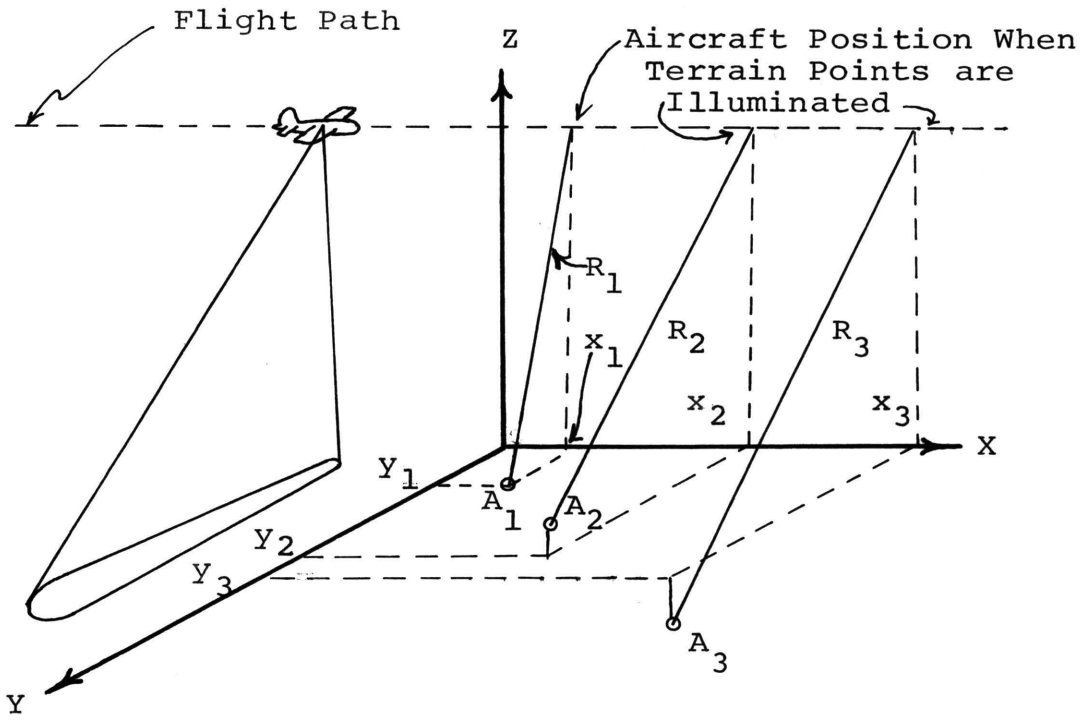

Fig. 5 Example of an Imaging Radar Which Employs a Side-Looking Vertical Fan Beam Antenna

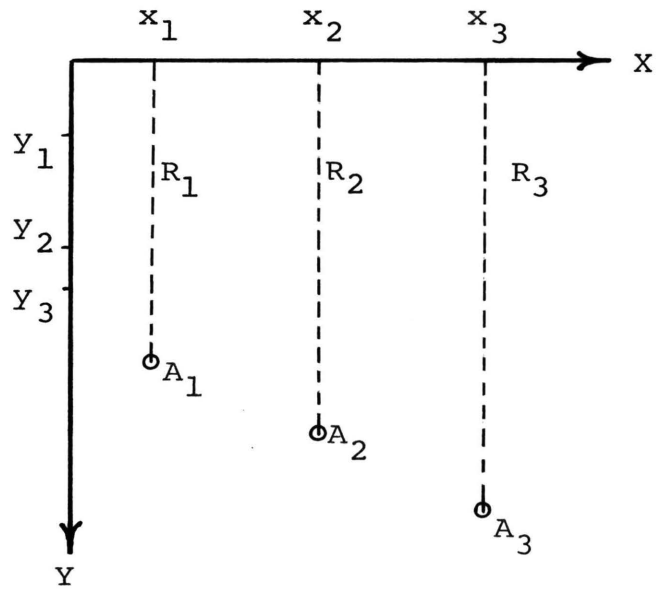

Fig. 6 Radar Image of the Terrain Points in Fig. 5 Obtained Using a Linear Range Sweep

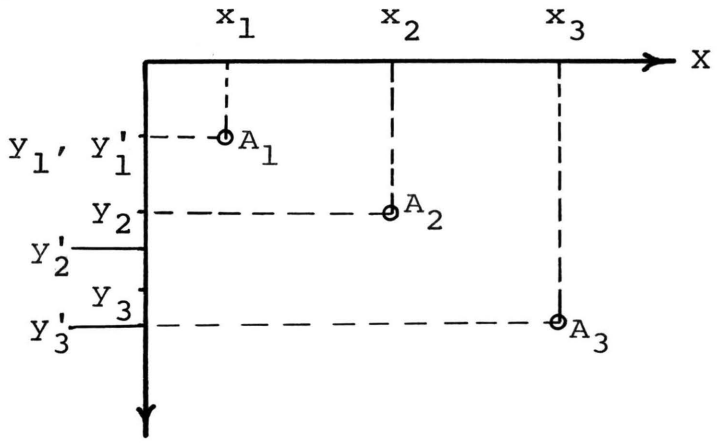

Fig. 7 Radar Image of the Terrain Points in Fig. 5 Obtained Using a Nonlinear Range Sweep

The mathematical form of the nonlinear sweep used to put the data in ground-range coordinates is dependent on the shape of the antenna beam and is considered in later sections. The result of applying a nonlinear sweep to this example is shown in Fig. 7. The coordinates y_1, y_2, and y_3 represent the true orthographic location as in Fig. 5 and y'_1, y'_2, and y'_3 represent the ground-range coordinates. It should be noted that point A_1 is the only point for which $y' = y$. This is because of the phenomenon of relief displacement (parallax) which causes the image location to differ from the true orthographic location for all points except those lying on the reference plane. This characteristic enables height information to be obtained, and will be covered in more detail in later sections. For this particular example it is seen that the terrain points above the reference plane are shifted toward the aircraft flight path and terrain points located below the reference plane are shifted away from the aircraft flight path. This result is true in general, no matter what type of antenna beam pattern and placement is used, but the geometry of this displacement for each radar technique must be considered individually because they differ. This is discussed in the following sections when the characteristics of each stereo radar technique are described.

B. IMPROVED SINGLE FLIGHT TECHNIQUE

The characteristics of the improved single flight technique for obtaining stereo radar images are discussed in this

section. Only aspects necessary for this analysis are covered. Much of this information is also described in Ref. 10 and the reader is referred to it for a more detailed discussion.

The improved single flight technique uses a combination of two different radar beam patterns to obtain the stereo imagery. One of the antennas is a horizontal linear array mounted at an angle $90^{\circ} - \theta_1$ with respect to the aircraft flight path as shown in Fig. 8. This antenna produces a vertical fan beam pattern at an angle θ_1 from the aircraft flight path as also shown in Fig. 8. The antenna beam is pointed horizontally in this figure to better describe the beam shape. In practice the beam is pointed slightly downward in order to intercept the terrain. The other antenna is a horizontal linear array with elements which are electronically linearly phased, and is mounted parallel to the flight path. This produces a beam pattern which is conical in shape and has a cone angle ϕ_2. The antenna beam and pattern are shown in Fig. 9. Again, the figure is a simplification and in practice the antenna beam is designed to intercept the terrain. Also, the cone angle ϕ_2 has been exaggerated. In practice this angle is quite large and the antenna beam is close to a planar surface.

For the remainder of this analysis, whenever reference is made to some aspect concerning the illumination by the antenna producing the vertical fan beam it will be called the fan beam case. Similarly, when reference is made to some

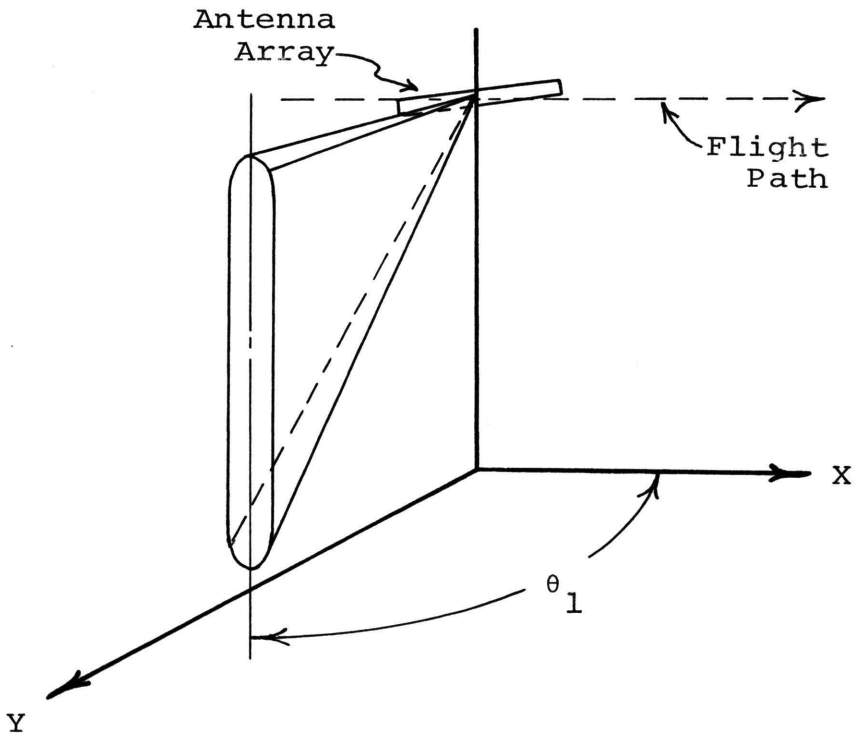

Fig. 8 Vertical Fan Beam Antenna and Pattern Used by the Improved Single Flight Technique

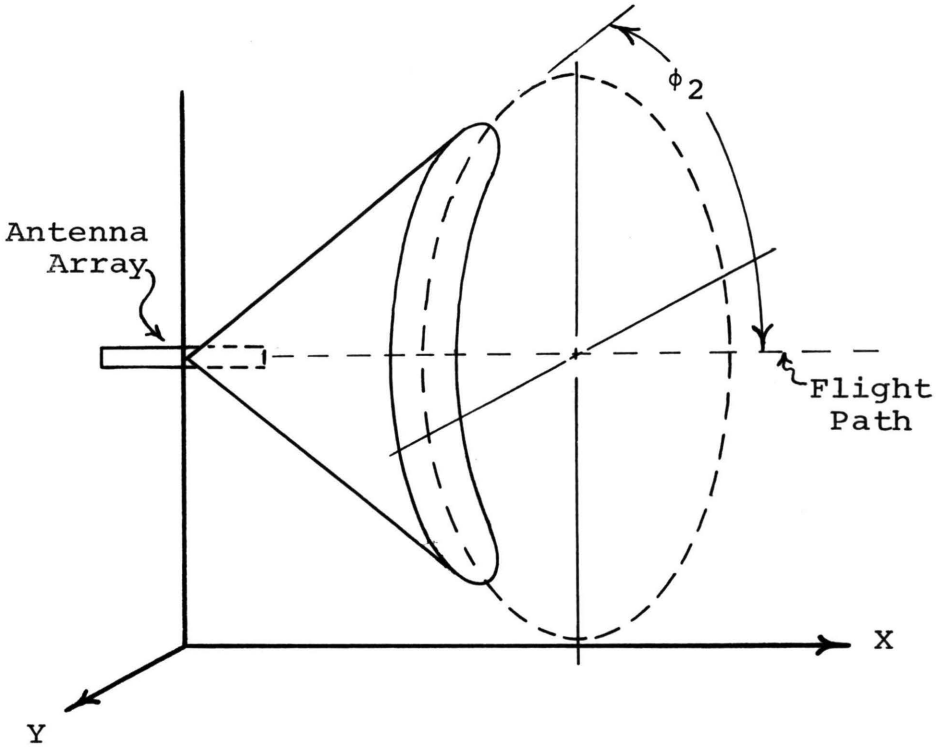

Fig. 9 Conical Beam Antenna and Pattern Used by the Improved Single Flight Technique

aspect concerning the illumination by the antenna producing the conical beam it will be called the conical beam case. Also, most quantities concerning the conical beam illumination are identified by a subscript 2 (e.g., ϕ_2) and most quantities concerning the fan beam illumination are identified by a subscript 1 (e.g., θ_1).

The geometry for image recording by the fan beam is described now and Fig. 10 is shown to aid in the discussion. Fig. 10 also defines the coordinate system used for the remainder of this analysis. The terrain point along-track orthographic location defines the Y axis and the nominal (errorless) aircraft flight track (the projection of the flight path on the X,Y plane) defines the X axis. The vertical defines the Z axis. The positive Z axis is chosen as pointing down so that the coordinate system is righthand. This allows conventional vector operations to be performed. The nominal aircraft altitude, H_A, and the terrain point height, h, are defined in a manner such that they are positive as shown in the figure. R_1 is the slant range and X_{A1} is the aircraft position along the flight track during terrain point illumination by the fan beam.

The quantities R_1 and X_{A1} are sensed by the radar system and recorded on the recording film. For the purposes of this analysis it is assumed that these quantities are initially recorded using a linear sweep and are displayed as shown in Fig. 11. As noted previously the slant-range format is not desirable and the data must be reimaged in a ground-range

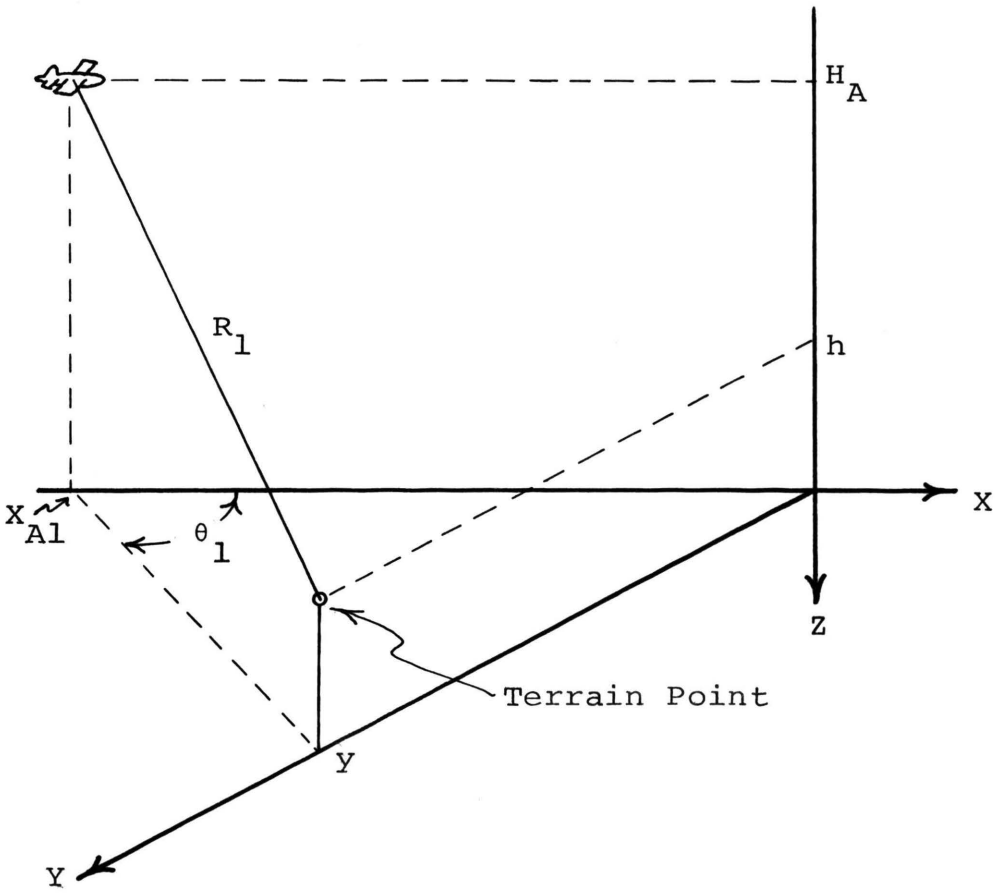

Fig. 10 Image Recording Geometry for the Fan Beam Illumination

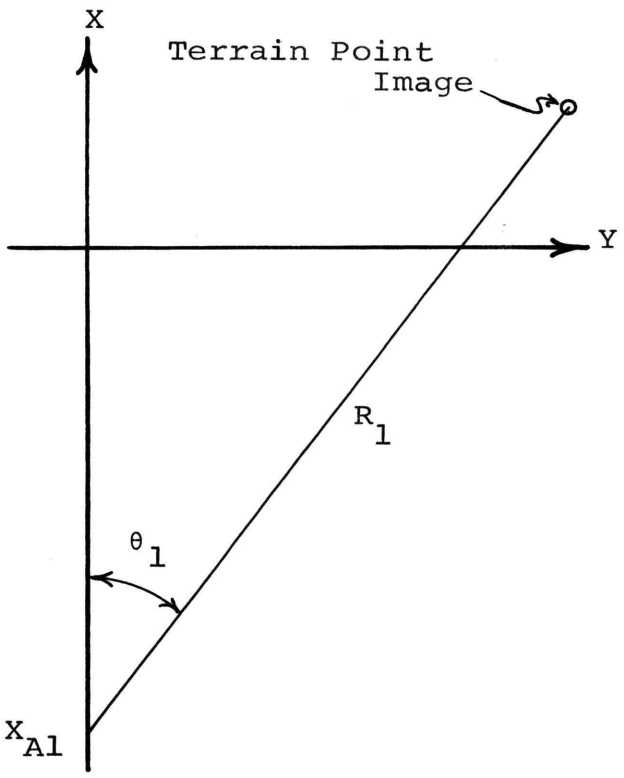

Fig. 11 Recorded Image of the Fan Beam Illumination of the Terrain Point in Fig. 10 Obtained Using a Linear Range Sweep

format. This reimaging converts the slant-range distance, R_1, to the corresponding ground-range distance for a reference plane which is at a distance H_A below the aircraft. To accomplish this it is necessary to determine R_{G1} which is the reference plane ground range to the terrain point as determined by the fan beam illumination. This quantity is shown in Fig. 12 and can be expressed as

$$R_{G1} = (R_1^2 - H_A^2)^{\frac{1}{2}} . \qquad (1)$$

To aid in interpretation, the ground range can be thought of as the distance to the point lying on the reference plane which is illuminated at the same instant that the elevated terrain point is illuminated since these two points result in radar return at the same time and thus cannot be distinguished. The reimaged radar image produced by the fan beam illumination is shown in Fig. 13. The effect of relief displacement on the location of the terrain point on the radar image is apparent in Fig. 13. The terrain point is not displayed at the true orthographic location but instead has been displaced toward the aircraft. Had the terrain point been located below the reference plane the location on the radar image would be shifted in the opposite direction, away from the aircraft. For later calculations it is desirable to determine the coordinates for the fan beam image which are designated (X_1, Y_1). Using Fig. 13 the expressions are

$$X_1 = X_{A1} + R_{G1} \text{Cos } \theta_1 \qquad (2)$$

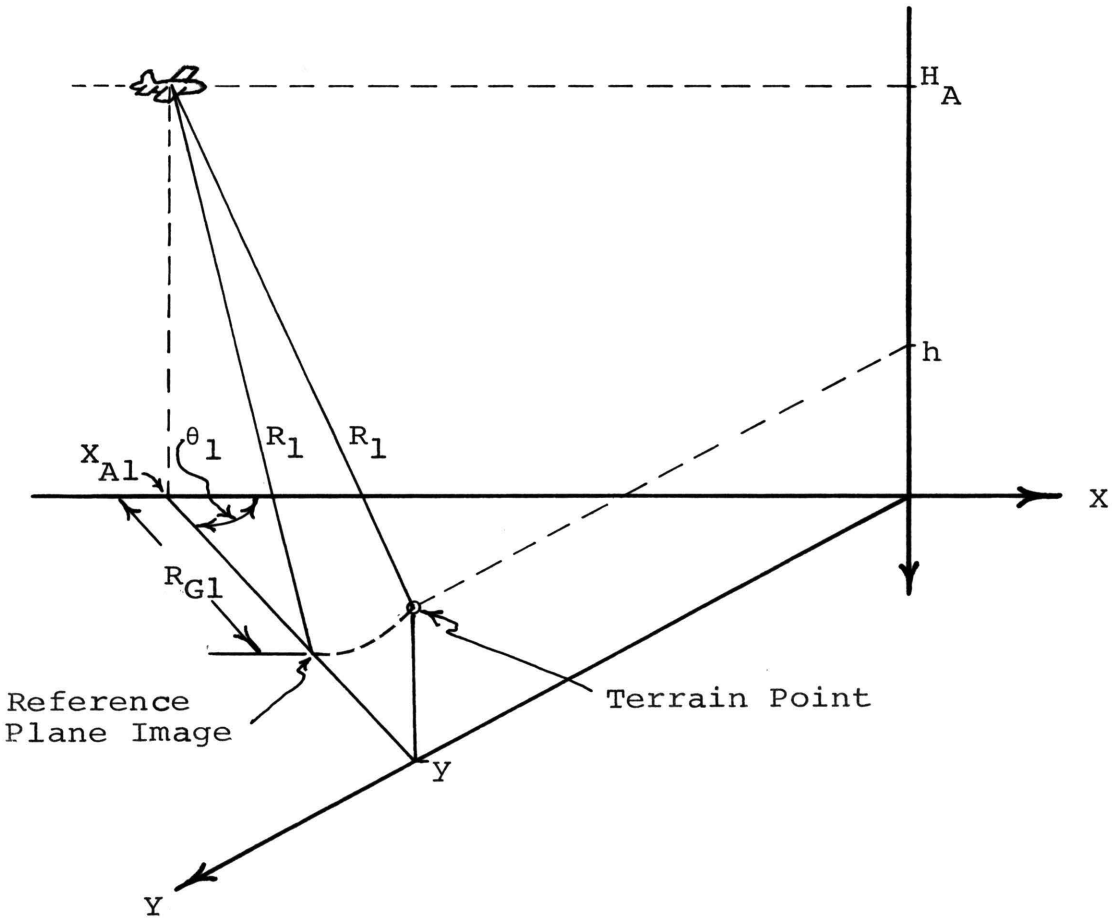

Fig. 12 Conversion From Slant-Range to Ground-Range Coordinates for the Fan Beam Illumination

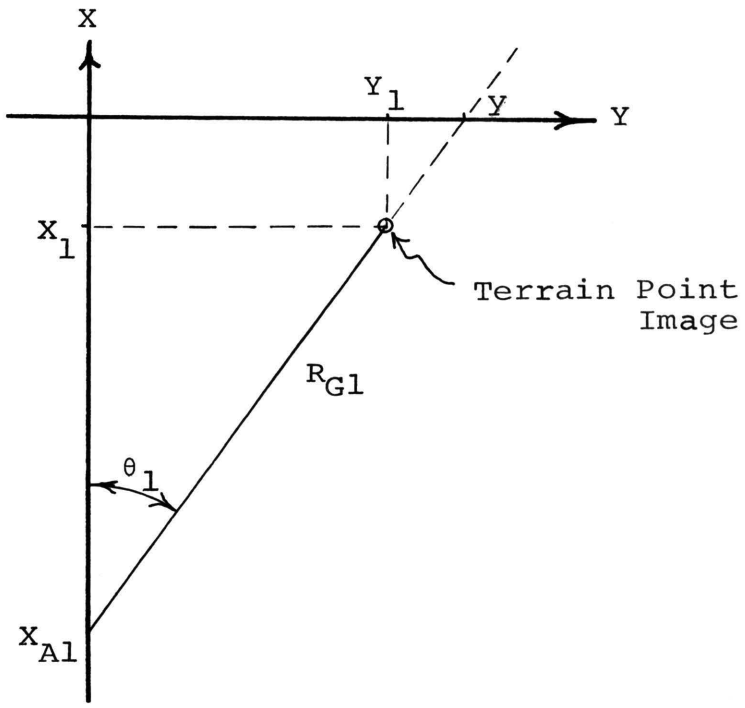

Fig. 13 Fan Beam Radar Image of the Terrain Point in Fig. 12 After Reimaging to Ground-Range Coordinates

$$Y_1 = R_{G1} \text{Sin } \theta_1 \ . \qquad (3)$$

The geometry for image recording by the conical beam is described next, and Fig. 14 is shown to aid in the discussion. The coordinate system used in this figure is the same as that used in Fig. 10 for the fan beam case. R_2 is the slant range to the terrain point and X_{A2} is the aircraft position during illumination by the conical beam. The quantities R_2 and X_{A2} are sensed by the radar system and recorded on the recording film. The quantities are initially recorded using a linear sweep and are displayed as shown in Fig. 15.

The transition between slant-range and ground-range format for the conical beam case is more difficult to visualize than the transition for the fan beam case. To aid in this, Fig. 16 is shown and it is reemphasized that the ground-range image can be thought of as that point lying on the reference plane which is illuminated at the same time that the elevated terrain point is illuminated. To obtain R_{G2}, a right triangle is formed using R_B, defined in the figure, as the hypotenuse and the aircraft altitude as one side. The triangle is solved for the other side which is R_{G2}. This gives

$$R_{G2} = (R_B^2 - H_A^2)^{\frac{1}{2}} \qquad (4)$$

where $R_B = R_2 \text{Sin } \phi_2$. R_{G2} is defined as the distance from the ground-range image point to the flight track instead of

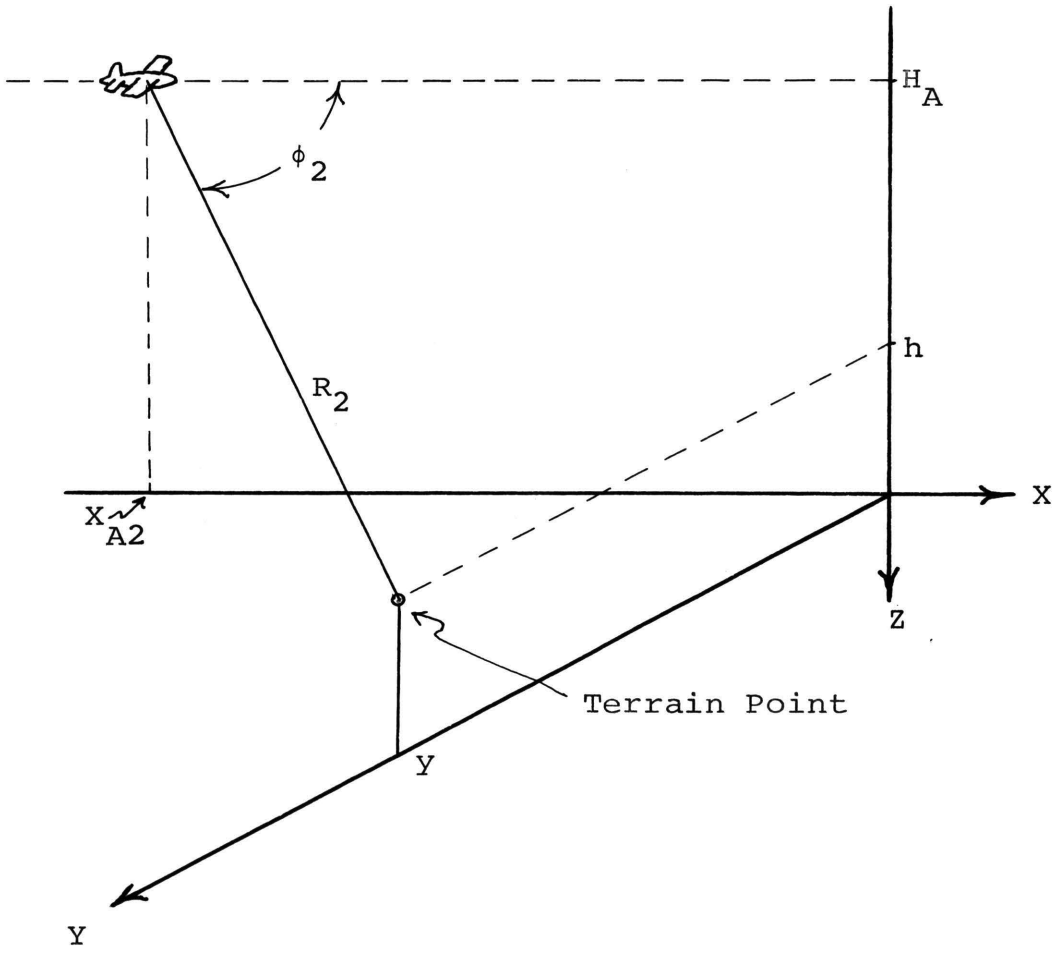

Fig. 14 Image Recording Geometry for the Conical Beam Illumination

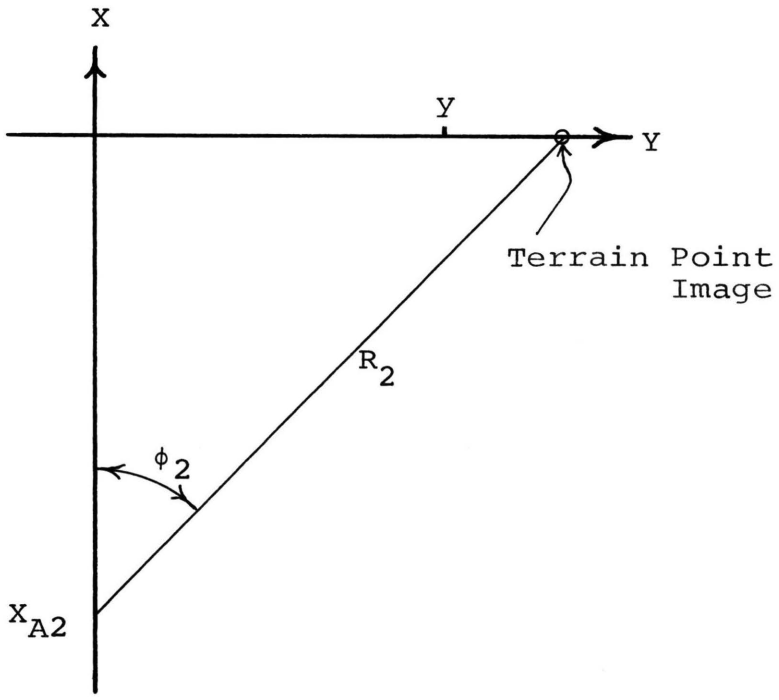

Fig. 15 Recorded Image of the Conical Beam Illumination of the Terrain Point in Fig. 14 Obtained Using a Linear Range Sweep

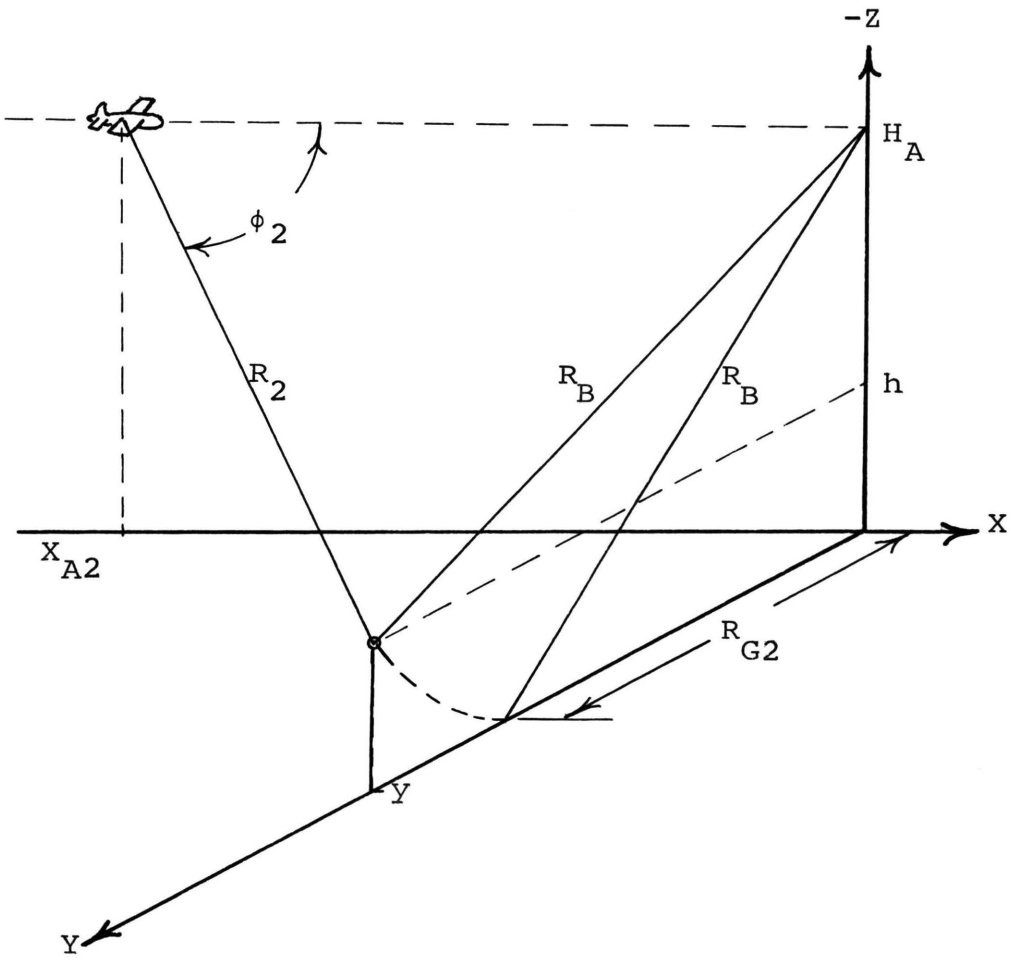

Fig. 16 Conversion From Slant-Range to Ground-Range Coordinates for the Conical Beam Illumination

the distance from the ground-range image point to the aircraft location at the time of illumination as for R_{G1}. This is done for convenience since the image displacement is perpendicular to the flight track. The resulting ground-range image for the conical beam illumination is shown in Fig. 17. The terrain point conical beam image coordinates (X_2, Y_2) are simply

$$X_2 = 0 \tag{5}$$

$$Y_2 = R_{G2} \, . \tag{6}$$

X_2 is identically zero (in the errorless case) since the conical beam illumination introduces no relief displacement in the along-track direction.

As a final point, it should be noted that the conical beam cone angle ϕ_2 does not enter directly into the evaluation of R_{G2}. For any choice of ϕ_2 the value of R_{G2} is the same. However, ϕ_2 does determine the aircraft position during illumination and so can be chosen in such a manner that X_{A1} and X_{A2} are very nearly equal for all terrain in the image swath. This allows the terrain to be illuminated from very nearly the same location for both illuminations and results in very desirable image characteristics. Specifically, the backscatter and shadow locations and sizes are nearly the same for both illuminations.

The radar image coordinates, (X_1, Y_1) and (X_2, Y_2), for the improved single flight technique have been obtained with

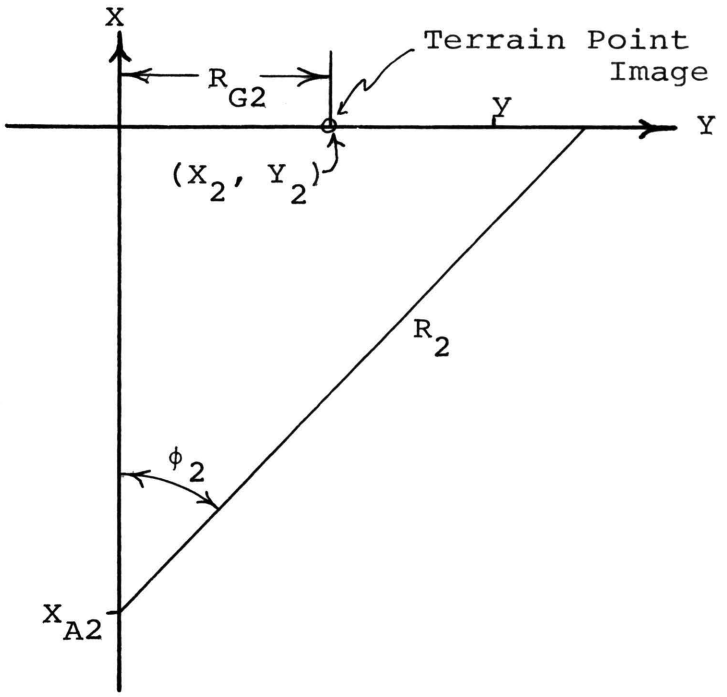

Fig. 17 Conical Beam Radar Image of the Terrain Point of Fig. 14 After Reimaging to Ground-Range Coordinates

the above analysis in terms of the system parameters, the slant range, and aircraft position during illumination. The superimposed image containing these coordinates is shown in Fig. 18. It will be shown in a later section that this information is sufficient to obtain the true orthographic location and height of the terrain point, (x,y,h). The methods of solution are also considered.

C. PREVIOUSLY PROPOSED SINGLE FLIGHT TECHNIQUE

A previously proposed technique for obtaining stereo radar images which requires only a single flight is described below. The technique uses two horizontal linear arrays which generate vertical fan beams (shown in Fig. 8), mounted at different azimuth angles aboard a single aircraft. The antenna mounting angles are arbitrary but must be sufficiently different in order to obtain the image relief displacement difference (parallax) necessary to produce a satisfactory stereo radar image.

In the analysis that follows the same quantity identifiers used for the improved single flight technique are used for the previous single flight technique and in the next section they are also used to describe the existing two flight technique. This is done for convenience due to the similarities between the techniques but does not mean that values are the same for all three techniques.

For the purpose of this analysis the previous single flight technique is assumed to use a forward slewed array mounted at an angle $90^\circ - \theta_1$ with respect to aircraft flight

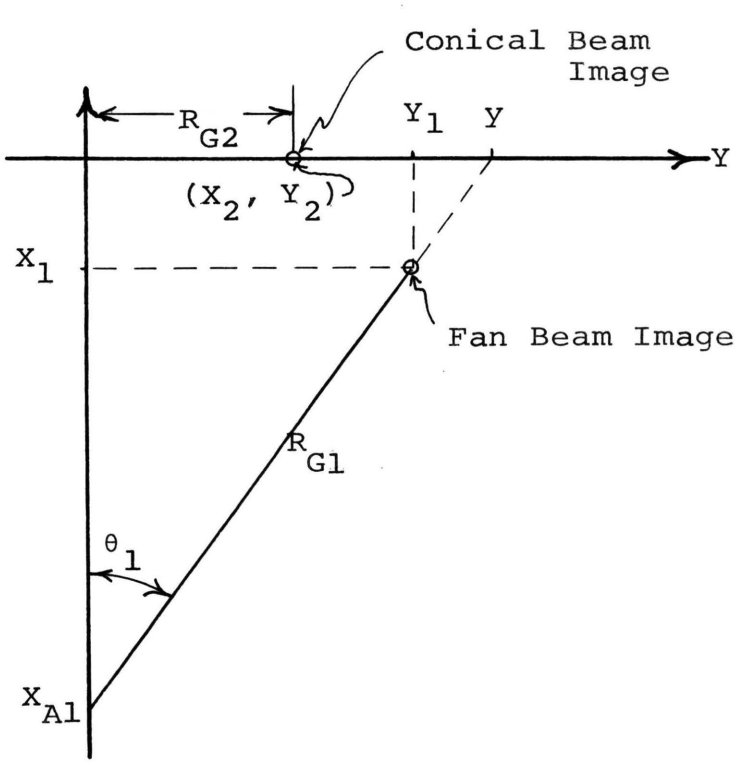

Fig. 18 Superimposed Radar Images Obtained Using the Improved Single Flight Technique

path so as to produce a vertical fan beam pattern at an angle θ_1 with respect to the aircraft flight path and a nearly side-looking array mounted at an angle $90^\circ - \theta_2$ with respect to the aircraft flight path so as to produce a vertical fan beam pattern at an angle θ_2 with respect to the aircraft flight path. When reference is made to illumination of a terrain point by the nearly side-looking antenna beam it will be called the rear beam case and most quantities concerning this illumination will be identified with the subscript 2. Similarly, when reference is made to illumination of a terrain point by the forward slewed beam it will be called the forward beam case, and the quantities concerning this illumination identified with the subscript 1.

Since both radar antenna beams for the previously proposed single flight technique are vertical fan beams, the analysis of the improved single flight fan beam illumination is applicable to both illuminations by the previous single flight technique. The analysis involves no new ideas; therefore, the calculations for each illumination are performed simultaneously. The geometry for image recording for both the forward and the rear beam illuminations is shown in Fig. 19. The slant ranges, R_1 and R_2, and the aircraft positions during illumination, X_{A1} and X_{A2}, are sensed by the radar system and recorded using a linear sweep as shown in Fig. 20. This data can be reimaged to ground-range coordinates using the method used for the improved single flight technique fan beam. For both forward

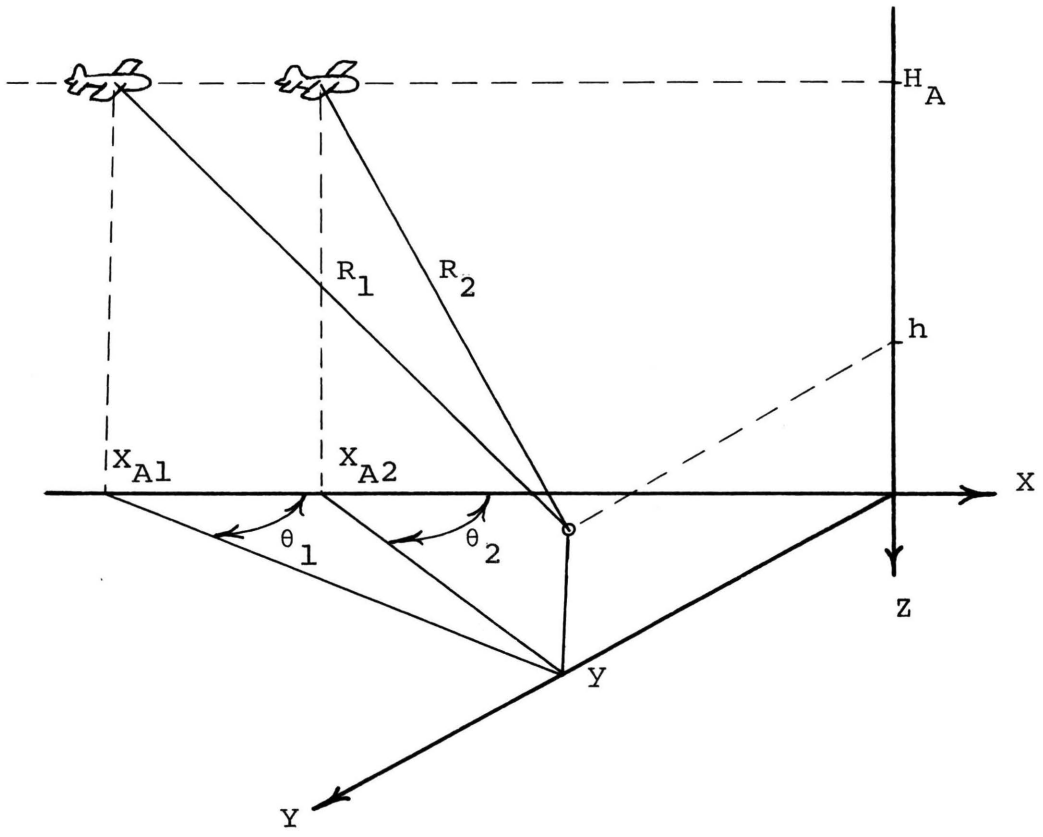

Fig. 19 Image Recording Geometry for Both Illuminations for the Previous Single Flight Technique

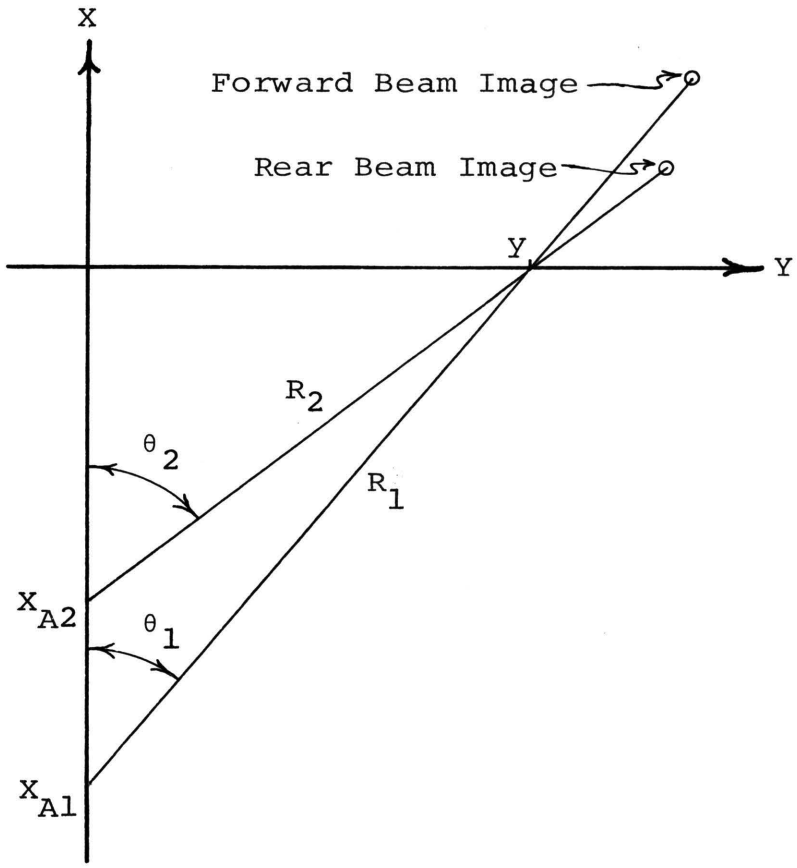

Fig. 20 Recorded Image of Both Illuminations of the Terrain Point in Fig. 19 Obtained Using a Linear Range Sweep

and rear beam illuminations the method can be described by using Fig. 12 and Eqn. 1 and replacing the fan beam quantities with appropriate forward or rear beam quantities. This results in the expressions

$$R_{G1} = (R_1^2 - H_A^2)^{\frac{1}{2}} \tag{7}$$

$$R_{G2} = (R_2^2 - H_A^2)^{\frac{1}{2}} , \tag{8}$$

where R_{G1} is the forward beam ground range and R_{G2} is the rear beam ground range. These quantities are shown in Fig.21. The terrain point image positions, (X_1, Y_1) and (X_2, Y_2), are obtained using Eqns. 2 and 3 to give

$$X_1 = X_{A1} + R_{G1}\text{Cos } \theta_1 \tag{9}$$

$$X_2 = X_{A2} + R_{G2}\text{Cos } \theta_2 \tag{10}$$

$$Y_1 = R_{G1}\text{Sin } \theta_1 \tag{11}$$

$$Y_2 = R_{G2}\text{Sin } \theta_2 . \tag{12}$$

In this section image coordinate expressions have been developed for the previous single flight technique. In a later section it is shown that this information is sufficient to obtain the true orthographic coordinates of the terrain point and methods for obtaining them are considered.

D. EXISTING TWO FLIGHT TECHNIQUE

The existing technique for obtaining stereo radar images uses a horizontal linear array which is mounted

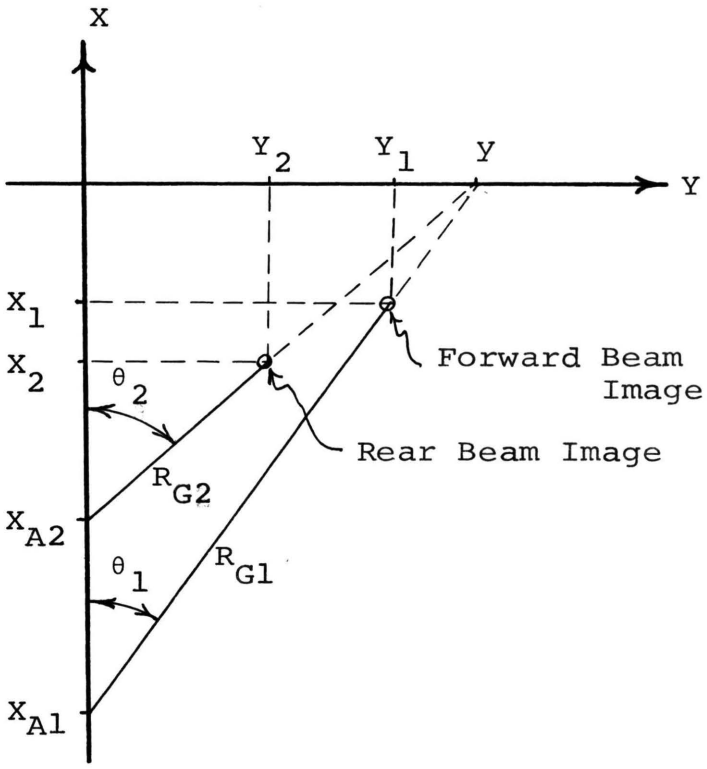

Fig. 21 Superimposed Radar Image of the Terrain Point in Fig. 19 After Reimaging to Ground-Range Coordinates

parallel to the aircraft flight path and produces a side-looking vertical fan beam. Two flights are made past the terrain being mapped. Terrain relief displacement suitable for producing stereo radar pairs can be obtained by making the two flights over the same flight track at different altitudes or over different flight tracks. Either of these methods cause terrain point illumination at different elevation angles which in turn produces characteristics which allow the determination of terrain point orthographic location and height from the radar data.

For the purposes of this analysis, it is assumed that the two flights past the terrain being mapped are made on different aircraft flight tracks. This is illustrated in Fig. 22. As shown, the terrain is illuminated at two different offset distances. The first flight path is used as a reference as with the two previously discussed methods. The second flight path is offset a distance Y_0 farther away from the terrain. The shaded area in the figure is the overlapping area which results in two images that comprise the stereo pair. When reference is made to some aspect concerning the illumination of a terrain point from the first flight path it is referred to as the near pass case and most quantities concerning this illumination are identified by a subscript 1 (e.g., R_1). Similarly, illumination from the second flight path is referred to as the far pass case and most quantities concerning this illumination are identified by a subscript 2.

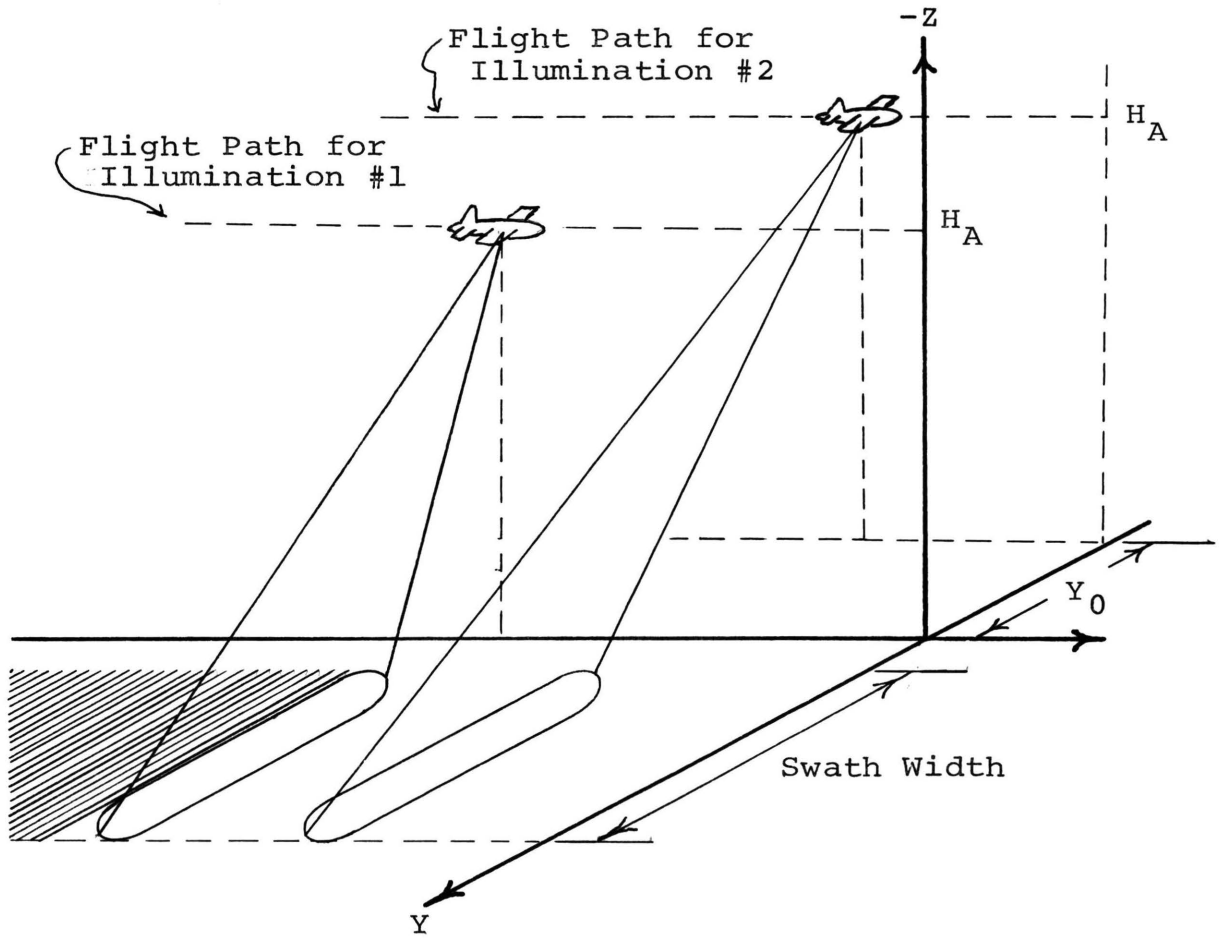

Fig. 22 Existing Two Flight Technique Illumination Scheme

The analysis of the improved single flight technique fan beam illumination is applicable to both illuminations by the two flight technique. The only difference is that $\theta_1 = \theta_2 = 0$ for the side-looking beam used. Since the illuminations are made by a side-looking beam it is possible to describe the image recording geometry with a two dimensional elevation view. This is shown in Fig. 23. It should be noted that the aircraft positions during illumination, X_{A1} and X_{A2}, are both zero with reference to the terrain point, for the errorless case being considered. The slant ranges, R_1 and R_2, and the aircraft positions during illumination, X_{A1} and X_{A2}, are sensed by the radar system and recorded in a slant-range format using a linear range sweep as shown in Fig. 24. This data can be reimaged in ground-range coordinates. Fig. 25 shows the graphical solution for the ground ranges, R_{G1} and R_{G2}. The analytic expressions are

$$R_{G1} = (R_1^2 - H_A^2)^{\frac{1}{2}} \tag{13}$$

$$R_{G2} = (R_2^2 - H_A^2)^{\frac{1}{2}} - Y_0 \, . \tag{14}$$

The ground-range images are shown superimposed in Fig. 26. The terrain point positions (X_1, Y_1) and (X_2, Y_2) are

$$X_1 = X_{A1} \tag{15}$$

$$X_2 = X_{A2} \tag{16}$$

$$Y_1 = R_{G1} \tag{17}$$

$$Y_2 = R_{G2} \quad . \tag{18}$$

In this section the radar image coordinates have been expressed in terms of the radar return data for the existing two flight technique. It will be shown in a later section that these coordinates can be used to determine the true orthographic location and height of the terrain point and methods for obtaining these quantities will be developed.

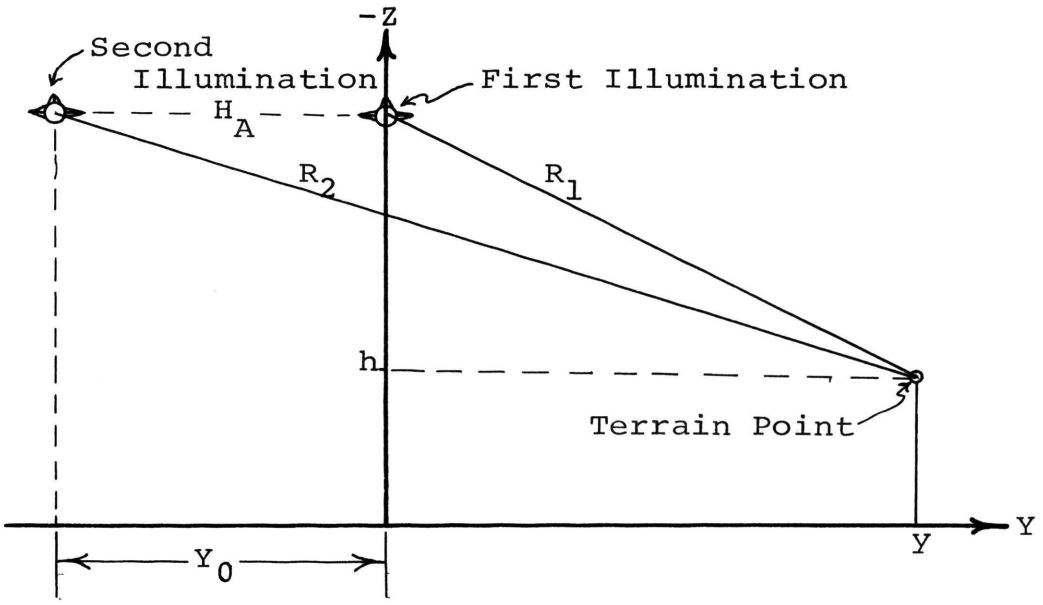

Fig. 23 Elevation View in the Illumination Plane Showing the Image Recording Geometry for the Two Flight Technique

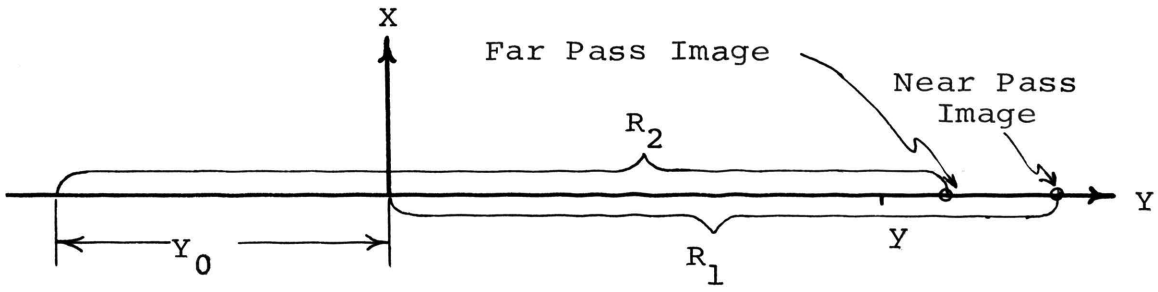

Fig. 24 Recorded Image of Both Illuminations of the Terrain Point in Fig. 23 Obtained Using a Linear Range Sweep

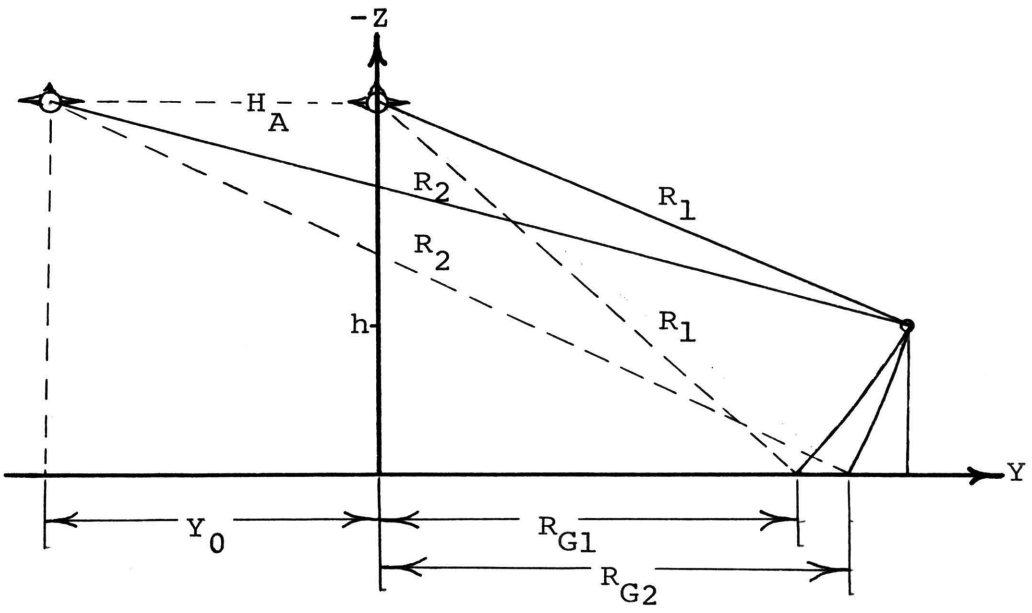

Fig. 25 Plan View of the Illumination Plane Showing the Conversion From Slant-Range to Ground-Range Coordinates for the Two Flight Technique

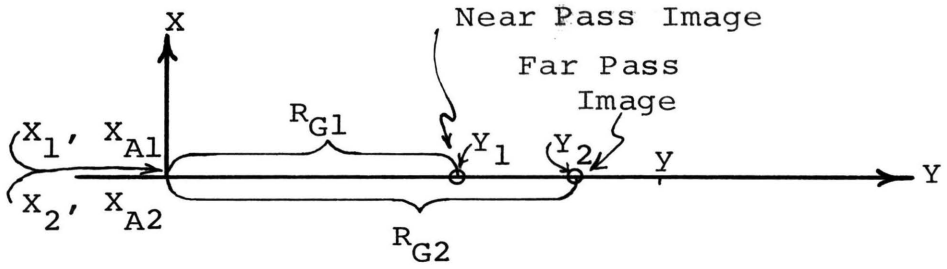

Fig. 26 Superimposed Radar Image of the Terrain Point in Fig. 23 After Reimaging to Ground Range Coordinates

IV. IMAGE MEASUREMENT TECHNIQUES AND STEREO MODEL RECONSTRUCTION

This section of the analysis is concerned with the methods available for measuring the image coordinates of the stereo images and the solution for the reconstruction of the terrain model from the image measurements. The reconstruction equations for each of the three stereo radar mapping techniques are considered first. For most cases the reconstruction equations lead to more than one solution for the terrain point coordinates. Final selection of the best equations is made after the system error analysis data are presented since it is desirable to use that set which is least sensitive to system errors. Next the techniques available for measuring the image coordinates are presented and it is shown that conventional analytic photogrammetric methods can be used.

A. STEREO MODEL RECONSTRUCTION

In the previous sections, stereo radar image characteristics are discussed and the three radar techniques for obtaining stereo radar images are described. For each technique it is shown that it is possible to process the radar return and obtain a pair of radar images. For each terrain point which is illuminated there corresponds a set of image coordinates (X_1, Y_1) and (X_2, Y_2). It is the purpose of this section to analyze the relation between the terrain point orthographic location and height and these image coordinates.

That is, the equations to determine the terrain point coordinates from the image coordinates are determined for each of the radar techniques. These equations are called the reconstruction equations. The reconstructed terrain point position is designated (x_r, y_r, h_r) to distinguish it from the original terrain point position (x, y, h). For the errorless case, these sets of coordinates are the same. For most cases there exists several solutions for each terrain point coordinate. Final selection of the best set of equations is made after the error analysis data are presented.

1. IMPROVED SINGLE FLIGHT TECHNIQUE

The equations required to determine the terrain point coordinates (x_r, y_r, h_r) from the image coordinates (X_1, Y_1) and (X_2, Y_2) for the improved single flight technique are considered here. To accomplish this a general coordinate system is used and equations for the terrain point image coordinates are determined. These expressions are then solved simultaneously to give expressions for x_r, y_r, and h_r in terms of X_1, Y_1, X_2, and Y_2.

Figs. 27 and 28 show the geometry for the illuminations for the improved single flight technique. It should be noted that the coordinate system has been left general and not tied to the terrain point. Also, the terrain point displacements, ΔR_{G1} and ΔR_{G2}, are defined such that

$$\Delta R_{G1}, \Delta R_{G2} < 0 \text{ when } h_r > 0 \ .$$

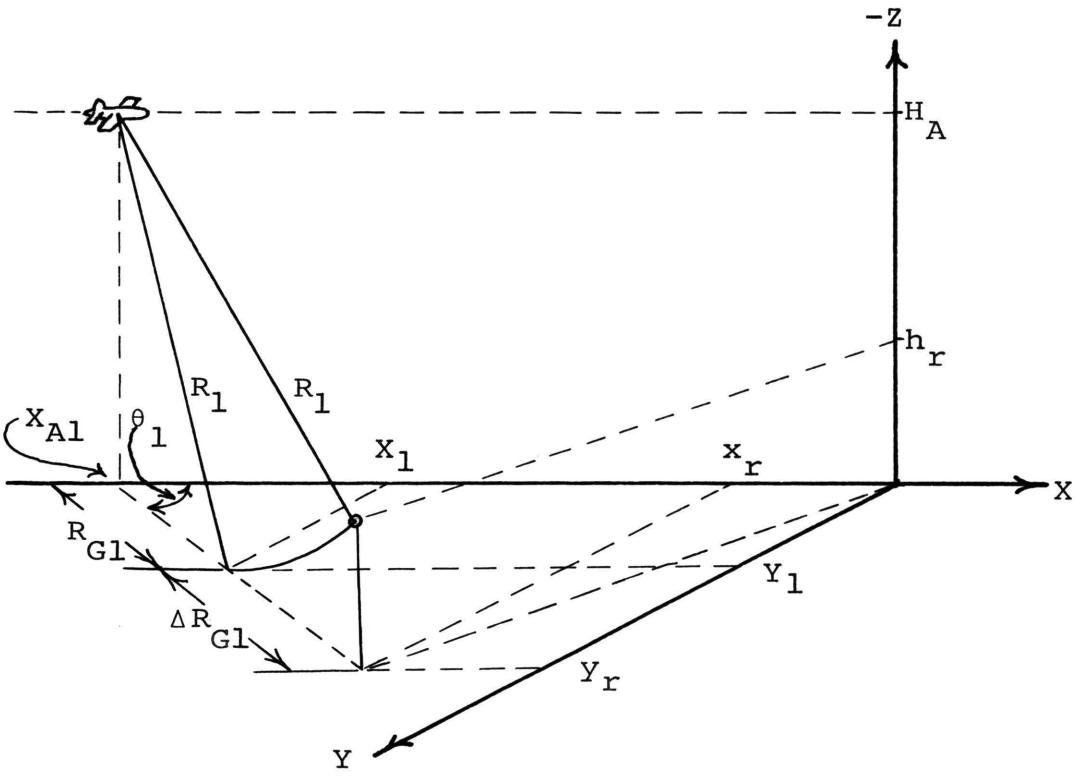

Fig. 27 Fan Beam Geometry

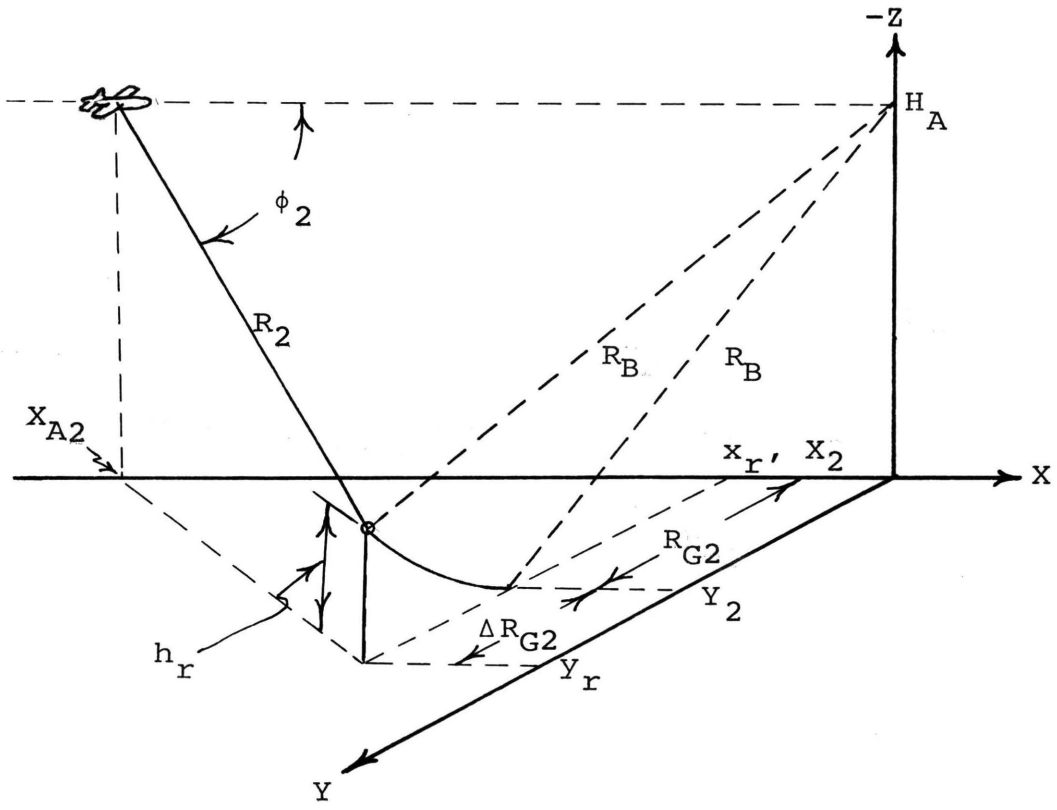

Fig. 28 Conical Beam Geometry

From Fig. 27 the expressions for the fan beam image coordinates can be written

$$\Delta R_{G1} = \{(y_r/\text{Sin } \theta_1)^2 - 2H_A h_r + h_r^2\}^{\frac{1}{2}} - y_r/\text{Sin } \theta_1 \tag{19}$$

$$X_1 = x_r + \Delta R_{G1}\text{Cos } \theta_1$$

$$= x_r - y_r\text{Cot } \theta_1 + \{y_r^2\text{Cot}^2 \theta_1 + (h_r^2 - 2H_A h_r)\text{Cos}^2 \theta_1\}^{\frac{1}{2}} \tag{20}$$

$$Y_1 = y_r + \Delta R_{G1}\text{Sin } \theta_1$$

$$= \{y_r^2 + (h_r^2 - 2H_A h_r)\text{Sin}^2 \theta_1\}^{\frac{1}{2}} . \tag{21}$$

Similarly from Fig. 28 the expressions for the conical beam image coordinates can be written

$$\Delta R_{G2} = -y_r + (y_r^2 + h_r^2 - 2H_A h_r)^{\frac{1}{2}} \tag{22}$$

$$X_2 = x_r \tag{23}$$

$$Y_2 = y_r + \Delta R_{G2} = (y_r^2 + h_r^2 - 2H_A h_r)^{\frac{1}{2}} . \tag{24}$$

Note that there are four independent equations containing the three unknowns x_r, y_r, and h_r and so there is not a unique solution. The equations for Y_1 and Y_2 are independent of x_r. This results because in the ideal errorless case the conical beam and fan beam illumination time have a definite relationship between them and this relationship does not vary with terrain point along-track position. Also, X_2 is independent of y_r and h_r because the geometry of the conical beam is such that no along-track parallax is introduced. Further analysis of this group of equations shows that there

exists two independent solutions for x_r, three independent solutions for y_r, and three independent solutions for h_r. In the development of the reconstruction equations, a specific solution is described by noting the equations from which it is derived. For example, if a solution is derived for y_r from Eqns. 20 and 24 then it is described as y_r from X_1 and Y_2, and is expressed symbolically as $y_r(X_1, Y_2)$.

First consider the solutions for y_r. The first solution considered is for y_r in terms of Y_1 and Y_2 and is designated $y_r(Y_1, Y_2)$. Squaring Eqns. 21 and 24 and solving for y_r gives

$$y_r^2 = Y_1^2 - (h_r^2 - 2H_A h_r)\text{Sin}^2\ \theta_1 \tag{25}$$

$$y_r^2 = Y_2^2 - (h_r^2 - 2H_A h_r)\ . \tag{26}$$

Solving Eqn. 26 for the quantity $(h_r^2 - 2H_A h_r)$ gives

$$h_r^2 - 2H_A h_r = Y_2^2 - y_r^2\ . \tag{27}$$

Substituting Eqn. 27 into Eqn. 25 gives

$$y_r^2 = Y_1^2 - (Y_2^2 - y_r^2)\text{Sin}^2\ \theta_1\ . \tag{28}$$

Solving Eqn. 28 for y_r yields the solution

$$y_r(Y_1, Y_2) = (Y_1^2 - Y_2^2\text{Sin}^2\ \theta_1)^{\frac{1}{2}}\text{Sec}\ \theta_1\ . \tag{29}$$

The second solution for y_r is in terms of X_1, X_2, and Y_2. Combining Eqns. 20 and 23 to eliminate x_r gives

$$X_1 = X_2 - y_r\text{Cot}\ \theta_1 + \{y_r^2\text{Cot}^2\ \theta_1 + (h_r^2 - 2H_A h_r)\text{Cos}^2\ \theta_1\}^{\frac{1}{2}}\ . \tag{30}$$

The quantity $(h_r^2 - 2H_A h_r)$ given by Eqn. 27 is substituted into Eqn. 30 to give

$$X_1 - X_2 + y_r \text{Cot } \theta_1 = \{y_r^2 \text{Cot}^2 \theta_1 + (Y_2^2 - y_r^2) \text{Cos}^2 \theta_1\}^{\frac{1}{2}} . \quad (31)$$

Eqn. 31 is squared and rearranged and results in the quadratic equation

$$y_r^2 + 2(X_1 - X_2) \text{Csc } \theta_1 \text{Sec } \theta_1 y_r + (X_1 - X_2)^2 \text{Sec}^2 \theta_1 - Y_2^2 = 0 . \quad (32)$$

Eqn. 32 is solved using the quadratic formula and results in the solutions

$$y_r(X_1, X_2, Y_2) = (X_2 - X_1) \text{Csc } \theta_1 \text{Sec } \theta_1 \pm \{(X_2 - X_1)^2 \text{Csc}^2 \theta_1 + Y_2^2\}^{\frac{1}{2}} . \quad (33)$$

The solution with the plus sign is the correct one. This is readily verified by letting $X_1 = X_2$ (i.e., $h = 0$), and noting that $y_r = Y_2$ is the correct answer. The final solution for y_r is in terms of X_1, X_2, and Y_1. Eqn. 25 is solved for $(h_r^2 - 2H_A h_r)$ to give

$$h_r^2 - 2H_A h_r = (Y_1^2 - y_r^2) \text{Csc}^2 \theta_1 . \quad (34)$$

Eqn. 34 is substituted into Eqn. 30 to give

$$X_1 - X_2 + y_r \text{Cot } \theta_1 = \{y_r^2 \text{Cot}^2 \theta_1 + (Y_1^2 - y_r^2) \text{Cot}^2 \theta_1\}^{\frac{1}{2}} . \quad (35)$$

Rearranging Eqn. 35 gives the solution

$$y_r(X_1, X_2, Y_1) = Y_1 + (X_2 - X_1) \text{Tan } \theta_1 . \quad (36)$$

Secondly, consider the three solutions for h_r. The first solution considered is for h_r in terms of Y_1 and Y_2. Eqns. 21 and 24 are squared and result in the expressions given by Eqns. 25 and 26. Eqns. 25 and 26 are combined and rearranged to give the quadratic equation

$$h_r^2 - 2H_A h_r + (Y_1^2 - Y_2^2)\mathrm{Sec}^2\,\theta_1 = 0 \ . \qquad (37)$$

Solving Eqn. 37 gives

$$h_r(Y_1, Y_2) = H_A \pm \{H_A^2 - (Y_1^2 - Y_2^2)\mathrm{Sec}^2\,\theta_1\}^{\frac{1}{2}} \ . \qquad (38)$$

The minus sign gives the correct solution and can be verified by letting $Y_1 = Y_2$ (i.e., $h = 0$) and noting that $h_r = 0$.

Analysis of the remaining solutions for h_r, specifically h_r in terms of X_1, X_2, and Y_2, and h_r in terms of X_1, X_2, and Y_2 shows that the direct solution for h_r requires the solution of a high order polynomial equation. To overcome this difficulty these two solutions are written in terms of y_r where y_r represents the solution using the same source equations.

The second solution for h_r is in terms of X_1, X_2, and Y_2. It is obtained by solving Eqn. 26 for h_r. This results in the quadratic equation

$$h_r^2 - 2H_A h_r + Y_2^2 - y_r^2 = 0 \ . \qquad (39)$$

The resulting solution is

$$h_r(X_1, X_2, Y_2) = H_A \pm (H_A^2 - y_r^2 + Y_2^2)^{\frac{1}{2}} \ , \qquad (40)$$

where y_r is given by Eqn. 33. Again, the minus sign gives the correct solution by arguments similar to those above. The third solution for h_r is in terms of X_1, X_2, and Y_1. It is obtained by solving Eqn. 25 for h_r and results in the quadratic equation

$$h_r^2 - 2H_A h_r + (Y_1^2 - y_r^2)\mathrm{Csc}^2\,\theta_1 = 0 \ . \qquad (41)$$

The resulting solution is

$$h_r(X_1, X_2, Y_1) = H_A \pm \{H_A^2 + (Y_1^2 - y_r^2)\mathrm{Csc}^2\,\theta_1\}^{\frac{1}{2}} \ , \qquad (42)$$

where y_r is given by Eqn. 36. Again, the minus sign gives the correct solution by arguments similar to those given previously.

Finally, the two solutions for x_r are considered. The first solution is in terms of X_2 and from Eqn. 23 is

$$x_r(X_2) = X_2 \ . \qquad (43)$$

The second solution for x_r is in terms of X_1, Y_1, and Y_2. To obtain this solution, the expression for $(h_r^2 - 2H_A h_r)$ given by Eqn. 34 is substituted into Eqn. 20 to give

$$x_r = X_1 + (Y_1 - y_r)\mathrm{Cot}\,\theta_1 \ . \qquad (44)$$

Substituting the expression for y_r given by Eqn. 29 into Eqn. 44 gives the solution

$$x_r(X_1, Y_1, Y_2) = X_1 + \mathrm{Csc}\,\theta_1 (Y_1^2 - Y_2^2\mathrm{Sin}^2\,\theta_1)^{\frac{1}{2}} - Y_1\mathrm{Cot}\,\theta_1 \ . \qquad (45)$$

The reconstruction equations for the improved single flight

technique have been derived in this section. These equations are summarized in Table I.

2. PREVIOUSLY PROPOSED SINGLE FLIGHT TECHNIQUE

The previously proposed single flight technique is analyzed next to determine the solution for the terrain point coordinates x_r, y_r, and h_r in terms of the image coordinates X_1, Y_1, X_2, and Y_2. As noted previously, this technique uses two vertical fan beams mounted at different azimuth angles. The expressions for image coordinates for both of the illuminations are the same as those for the fan beam illumination of the improved single flight technique. Thus Fig. 27 and Eqns. 19, 20, and 21 can be used to obtain the expressions

$$X_1 = x_r - y_r \text{Cot}\ \theta_1 + \{y_r^2 \text{Cot}^2\ \theta_1 + (h_r^2 - 2H_A h_r)\text{Cos}^2\ \theta_1\}^{\frac{1}{2}} \quad (46)$$

$$Y_1 = \{y_r^2 + (h_r^2 - 2H_A h_r)\text{Sin}^2\ \theta_1\}^{\frac{1}{2}} \quad (47)$$

for the forward beam image coordinates and the expressions

$$X_2 = x_r - y_r \text{Cot}\ \theta_2 + \{y_r^2 \text{Cot}^2\ \theta_2 + (h_r^2 - 2H_A h_r)\text{Cos}^2\ \theta_2\}^{\frac{1}{2}} \quad (48)$$

$$Y_2 = \{y_r^2 + (h_r^2 - 2H_A h_r)\text{Sin}^2\ \theta_2\}^{\frac{1}{2}} \quad (49)$$

for the rear beam image coordinates where each of the variables are as previously defined.

It is possible to solve Eqns. 46, 47, 48, and 49 to obtain multiple solutions for each terrain point coordinate. However, this is much more difficult than the previous solutions determined for the improved single flight technique.

Table I Terrain Point Reconstruction Equations for the Improved Single Flight Technique

Image Coords. Used	x_r	Y_r	h_r
X_1, Y_1, Y_2	$X_1 - Y_1 \text{Cot}\ \theta_1 + \text{Csc}\ \theta_1 (Y_1^2 - Y_2^2 \text{Sin}^2\ \theta_1)^{\frac{1}{2}}$	$(Y_1^2 - Y_2^2 \text{Sin}^2\ \theta_1)^{\frac{1}{2}} \text{Sec}\ \theta_1$	$H_A - \{H_A^2 - (Y_1^2 - Y_2^2) \text{Sec}^2\ \theta_1\}^{\frac{1}{2}}$
X_1, X_2, Y_1	X_2	$Y_1 + (X_2 - X_1) \text{Tan}\ \theta_1$	$H_A - \{H_A^2 + (Y_1^2 - y_r^2) \text{Csc}^2\ \theta_1\}^{\frac{1}{2}}$ where $y_r = y_r(X_1, X_2, Y_1)$
X_1, X_2, Y_2		$(X_2 - X_1) \text{Csc}\ \theta_1 \text{Sec}\ \theta_1 + \{(X_2 - X_1)^2 \text{Csc}^2\ \theta_1 + Y_2^2\}^{\frac{1}{2}}$	$H_A - (H_A^2 - y_r^2 + Y_2^2)^{\frac{1}{2}}$ where $y_r = y_r(X_1, X_2, Y_2)$

This is because each of the images contain relief displacement in both along-track and cross-track directions. In a later section, a discussion of system parameters to be used for the error analysis is given and it is determined that for comparison purposes θ_2 should be chosen to be 90°. This makes the rear beam side-looking. Using $\theta_2 = 90°$, Eqns. 48 and 49 reduce to

$$X_2 = x_r \tag{50}$$

$$Y_2 = \{y_r^2 + (h_r^2 - 2H_A h_r)\mathrm{Sin}^2\ \theta_2\}^{\frac{1}{2}} . \tag{51}$$

Comparison of these image coordinate equations (Eqns. 46, 47, 50, and 51) with the improved single flight coordinate equations (Eqns. 20, 21, 23, and 24) shows that they are exactly the same. Thus the resulting solutions for the terrain point coordinates in terms of the improved single flight technique quantities, summarized in Table I, are also applicable to the previous single flight technique for the case $\theta_2 = 90°$.

3. EXISTING TWO FLIGHT TECHNIQUE

The equations for determining the terrain point coordinates from the image coordinates for the existing two flight technique are developed in this section. The geometry for each of the illuminations is shown in Figs. 29 and 30. The expressions for the near pass illumination image coordinates can be written using the geometry shown in Fig. 29 and are

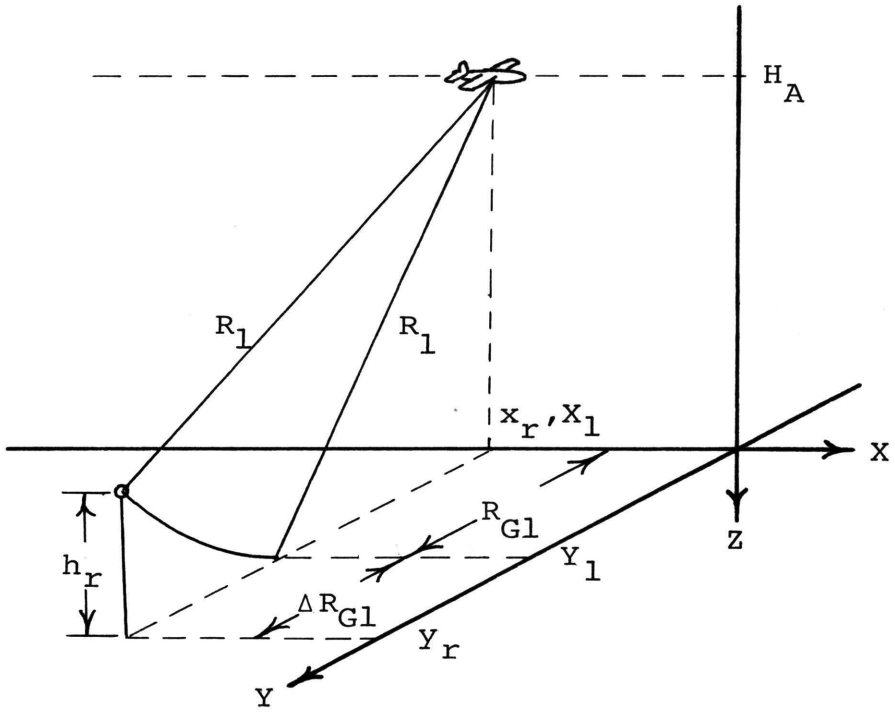

Fig. 29 Near Pass Illumination Geometry

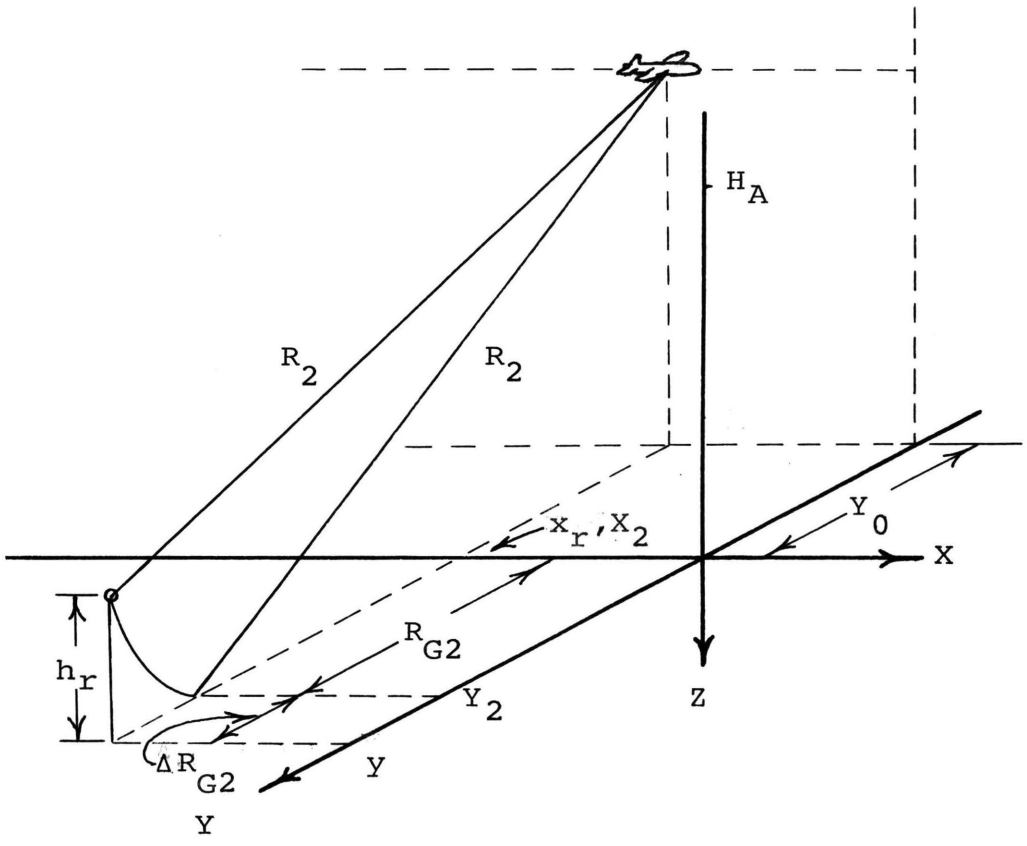

Fig. 30 Far Pass Illumination Geometry

$$X_1 = x_r \tag{52}$$

$$Y_1 = (y_r^2 - 2H_A h_r + h_r^2)^{\frac{1}{2}} . \tag{53}$$

Similarly, from Fig. 30, the expressions for the far pass illumination image coordinates are

$$X_2 = x_r \tag{54}$$

$$Y_2 = \{(y_r + Y_0)^2 - 2H_A h_r + h_r^2\}^{\frac{1}{2}} - Y_0 . \tag{55}$$

Analysis of the image coordinate equations shows that there are two solutions for x_r and only one solution for y_r and h_r. From Eqns. 52 and 54 the solutions for x_r are

$$x_r(X_1) = X_1 \tag{56}$$

$$x_r(X_2) = X_2 . \tag{57}$$

The solution for y_r is obtained by first solving Eqn. 53 for the quantity $(h_r^2 - 2H_A h_r)$ to give

$$h_r^2 - 2H_A h_r = Y_1^2 - y_r^2 \tag{58}$$

and substituting this into Eqn. 55 to yield

$$Y_2 = \{(y_r + Y_0)^2 + Y_1^2 - y_r^2\}^{\frac{1}{2}} - Y_0 . \tag{59}$$

Eqn. 59 when simplified results in the solution

$$y_r(Y_1, Y_2) = (Y_2^2 - Y_1^2 + 2Y_2 Y_0)/2Y_0 . \tag{60}$$

The solution for h_r is obtained by squaring Eqn. 53 and rearranging to give the quadratic equation

$$h_r^2 - 2H_A h_r + y_r^2 - Y_1^2 = 0 \ . \qquad (61)$$

The solution of this equation gives

$$h_r(Y_1, Y_2) = H_A - (H_A^2 + Y_1^2 - y_r^2)^{\frac{1}{2}} \qquad (62)$$

where y_r is given by Eqn. 60.

The reconstruction equations which have been derived for the existing two flight technique are summarized in Table II.

B. IMAGE MEASUREMENT

The image coordinates previously defined (X_1, Y_1, X_2, Y_2) must be measured before the reconstruction equations derived above can be applied. It is the purpose of this section to explain the techniques used to measure the image coordinates. The measurement techniques are described briefly and the reader is referred to Refs. 1, 10, and 11 for more detailed discussions.

The measurement of the image positions on the two stereo images can be performed by making separate measurements on each of the images. However, more accurate results can be obtained if the images are view stereoscopically. In addition, the measurements can be made faster and more economically and with greater correlation of the images than is possible with separate measurements.

Stereo radar images can be viewed stereoscopically using conventional photogrammetric equipment. To explain the technique Figs. 31 and 32 are shown. Fig. 31 shows how

Table II Terrain Point Reconstruction Equations for the Two Flight Technique

Image Coords. Used	x_r	Y_r	h_r
X_1	X_1		
X_2	X_2		
Y_1, Y_2		$(Y_2^2 - Y_1^2 + 2Y_2Y_0)/2Y_0$	$H_A - (H_A^2 + Y_1^2 - Y_r^2)^{\frac{1}{2}}$

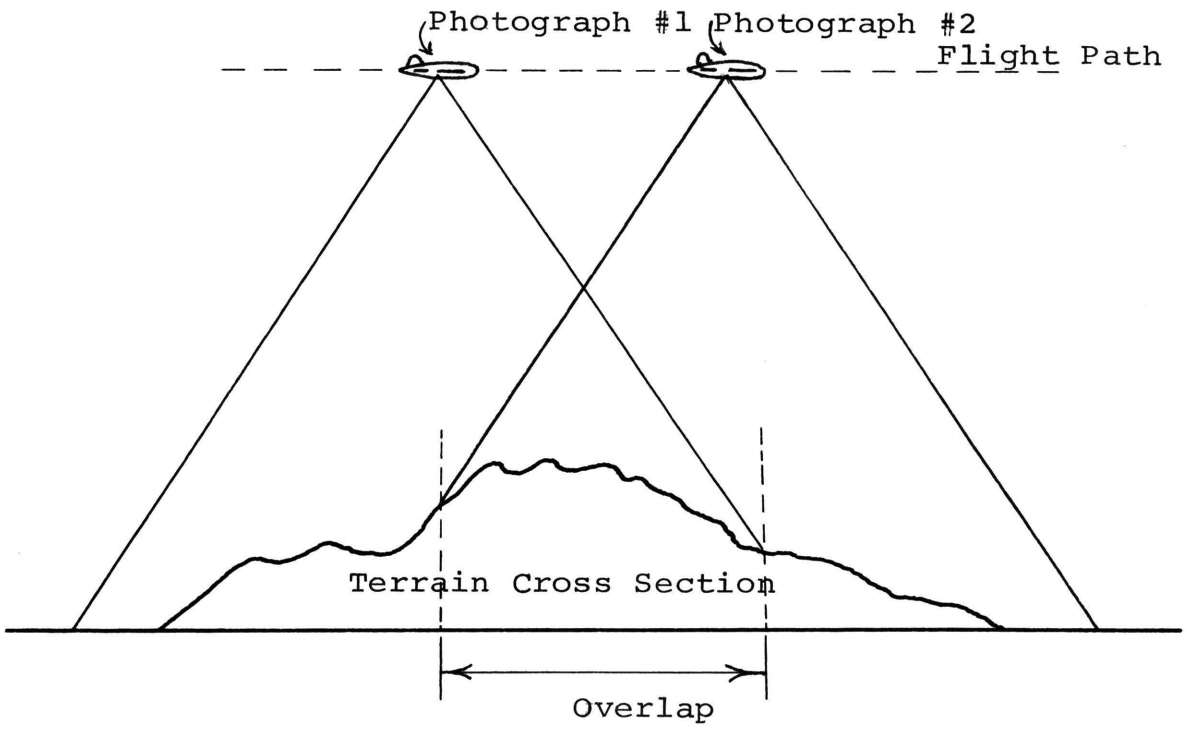

Fig. 31 Producing Photographs for Stereo Viewing

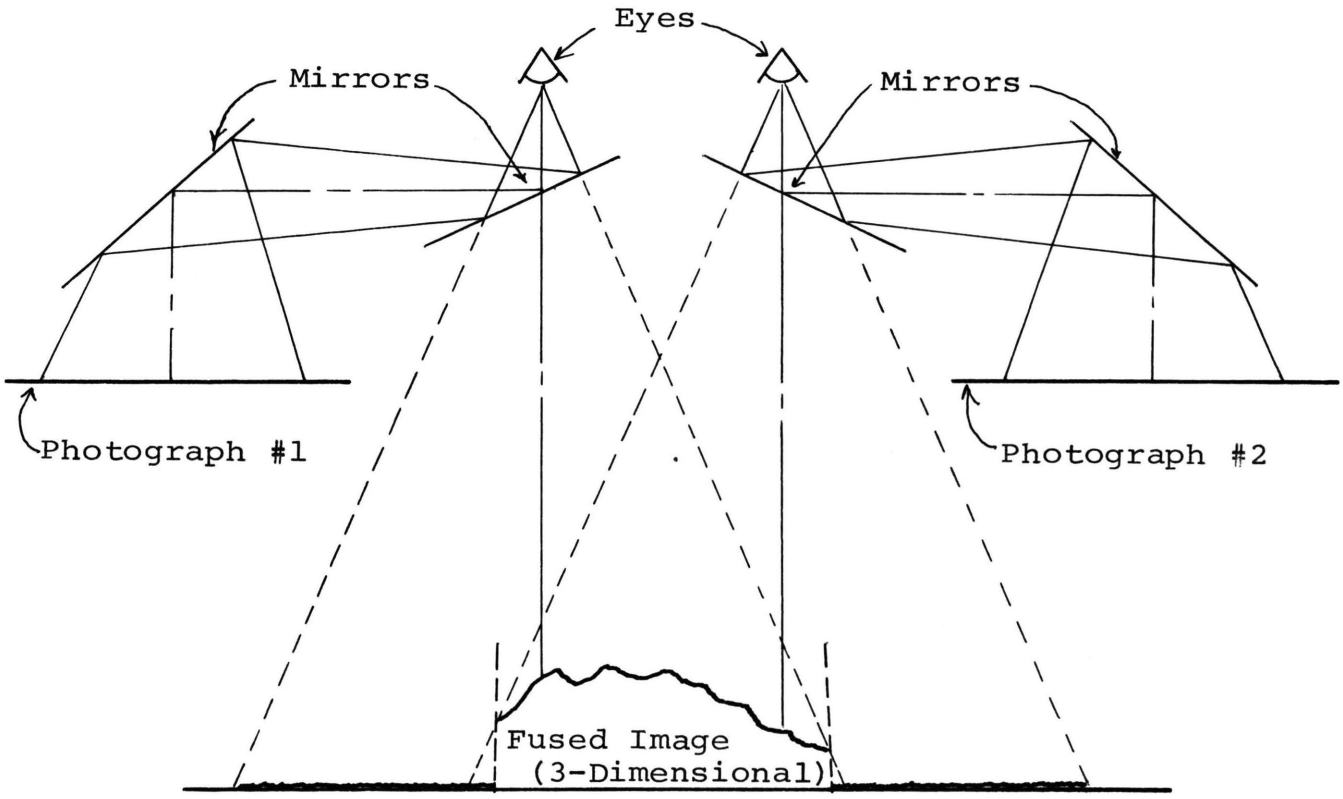

Fig. 32 Binocular Optical System for Stereoscopic Viewing

two overlapping photographs are taken. The images which result contain relief displacement which is radial with respect to the point directly beneath the aircraft at the time of each exposure. This causes the total parallax to lie in the same direction for all portions of the terrain. If the photographs are at an appropriate scale, positioned properly, and the relief displacement aligned with the axis lying parallel to the observer's eyes then a perception of depth is obtained. A simplified binocular optical system which allows stereoscopic observation of the photographs from Fig. 31 is shown in Fig. 32.

The stereocomparator is a machine which allows stereoscopic viewing as shown in Fig. 32. In addition, the machine is capable of simultaneous measurement of the coordinates of corresponding images on the stereo pair of photographs. This is accomplished by means of reference dots which are mounted in the optics of the machine. The reference dots fuse and appear as a single dot which appears to float in space and is at the same apparent elevation as the point being measured when the two reference dots correspond to the two image positions. When the correspondence is made the two image positions are recorded on a permanent medium (e.g., computer cards).

The method just described for aerial photographs is also applicable to stereo radar images provided that the relief displacement is in one direction. Fig. 26 shows the superimposed radar images for the existing two flight

technique. From the figure it is seen that the relief displacement is always in one direction and thus the photographic measurement methods apply for this technique. Figs. 18 and 21 show the superimposed radar images for the improved single flight technique and the previous single flight technique. From the figures it appears that the relief displacement might not lie in a single direction. However, if $\theta_2 = 90^\circ$ for the previous single flight technique so that the resulting images for both techniques are the same and are as shown in Fig. 33, then it can be shown that the angle β defined in Fig. 33 is approximately 90° for all practical values of terrain height.[10] This means that an auxillary U,V coordinate system can be defined as shown and the images oriented so that the operator's eyes are parallel to the U direction. Image measurements can be made using this reference frame and the data obtained can be transformed to the X,Y reference frame using a simple transformation.[11]

Thus, the radar images produced by all three of the stereo radar mapping techniques can be processed using conventional photogrammetric methods. In fact, pseudo-radar images have been produced for each of the radar techniques and have been viewed successfully.[11]

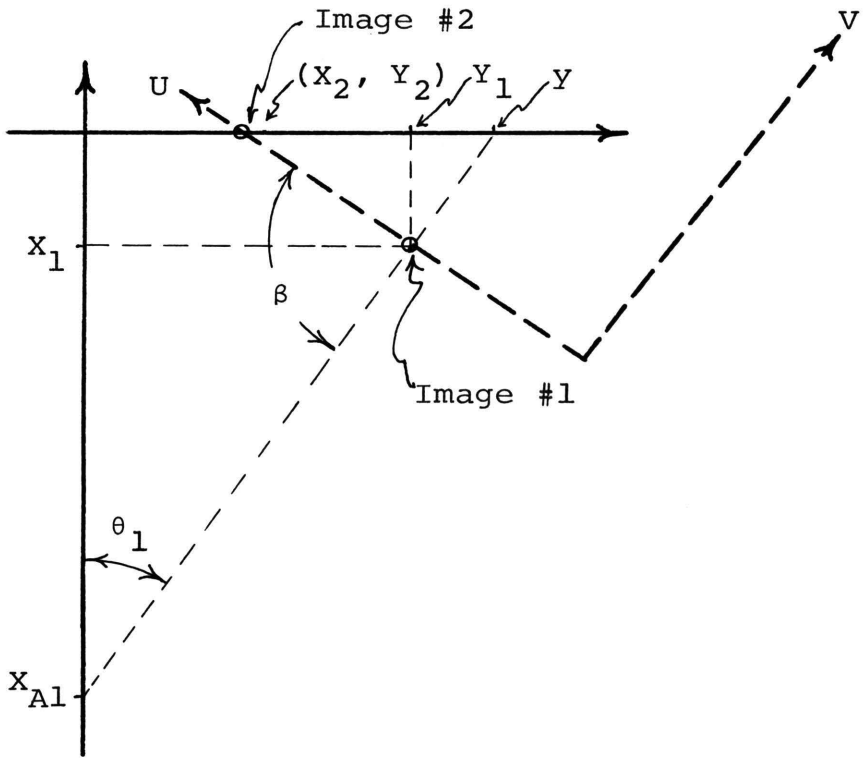

Fig. 33 Image Measurement Geometry for the Single Flight Techniques

V. ERROR ANALYSIS

A comparative analysis of the capability of the three stereo radar techniques when operating in the presence of system errors is described in this section. Of interest is the practical feasibility of the two proposed stereo radar techniques and the comparison of the capabilities of the three techniques with system errors present. This analysis is accomplished by means of a computer simulation in which a generalized solution for the radar images for each of the three techniques including the effects of all errors is used. From this simulation, sensitivities are determined for each image coordinate with respect to each individual error. The errors are assumed random and statistically independent and values for error standard deviations are assigned according to currently available equipment and sensor capabilities. These error values are used with the sensitivity values to obtain the standard deviations of the image coordinates.

Next, sensitivities of the reconstructed terrain point orthographic location and height coordinates to image coordinates are determined for each set of reconstruction equations. These sensitivities are used with the image coordinate standard deviations to determine the terrain point coordinate standard deviations for each reconstruction equation. From this, the optimum set of reconstruction equations are chosen. Computer programs are used to simulate a generalized solution for the radar images and the terrain

reconstruction, including the effect of errors, for each of the stereo radar techniques. From this simulation, the total system performance for each of the techniques in the presence of errors is determined. The results are analyzed, the feasibility of the two proposed techniques determined, and comparisons of the capabilities of the three techniques are made.

A. SELECTION OF SYSTEM PARAMETERS FOR COMPARISON PURPOSES

Prior to considering the error analysis calculations it is necessary to decide on a set of system parameter values for the three stereo radar techniques. These system parameters must be chosen so that the three techniques have the same theoretical performance capabilities to give error analysis results which can be used to give unbiased comparisons. Also, the theoretical terrain measurement capabilities of the single flight techniques must be known so that the magnitude of the reconstructed terrain point coordinate errors can be compared with the theoretical measurement capabilities to determine if the techniques are error limited.

In Ref. 10 a trade-off analysis of the improved single flight technique is performed to determine an optimum set of system parameters. These include aircraft altitude, swath width and location, elevation angles for both antennas, fan beam azimuth angle, and conical beam cone angle. These parameters are chosen to optimize parallax sensitivity (defined as the unit parallax per unit terrain height) across

the swath, aircraft position difference between subsequent illuminations of the same terrain point, illumination angle difference, shadow length difference, and radar resolution difference. The optimum system parameters and the resulting image parameter values are shown in Table III.

A trade-off analysis to determine the optimum system parameters for the previous single flight technique has not been performed. However, if it is assumed that this technique is implemented by replacing the conical beam of the improved single flight technique with a vertical fan beam looking perpendicular to the aircraft flight path then the images have the same geometries as the improved single flight technique. For the purpose of this analysis it is assumed that the improved single flight parameters can be used with this antenna beam change to give the optimum performance for this technique. The system parameters and the resulting image parameters are given in Table IV.

For comparison purposes the presently implemented two flight technique is not specified to have the same values for parameters as the improved single flight technique. Instead a set of parameters which has been used to obtain imagery with approximately the same parallax sensitivity and which gives about the same size swath as the other techniques is considered so that comparisons can be made with an existing imaging system. The system parameters used for this analysis and the resulting image parameters are shown in Table V.

Table III System and Image Parameters for the Improved Single Flight Technique

System Parameters	
Image Width (mi.)	2
Aircraft Altitude (ft.)	15,000
Beam #1	
Elevation Angle (deg.)	50.8 to 32.6
Azimuth Angle (deg.)	70
Beam #2	
Elevation Angle (deg.)	50.0 to 32.9
Azimuth Angle (deg.)	66.4 to 72.1
Cone Angle (deg.)	75.1

Image Parameters	
Parallax Sensitivity (unit parallax per unit terrain height)	0.445 to 0.232
Aircraft Position Difference (ft.)	-849 to 918
Illumination Angle Difference (deg.)	-3.71 to 2.13
Shadow Length Difference (%)	2.58 to -1.28
Resolution Difference (%)	-2.71 to 0.82

Table IV System and Image Parameters for the Previous Single Flight Technique

System Parameters	
Image Width (mi.)	2
Aircraft Altitude (ft.)	15,000
Beam #1	
Elevation Angle (deg.)	50.8 to 32.6
Azimuth Angle (deg.)	70
Beam #2	
Elevation Angle (deg.)	52.6 to 34.2
Azimuth Angle (deg.)	90
Image Parameters	
Parallax Sensitivity (unit parallax per unit terrain height)	0.445 to 0.232
Aircraft Position Difference (ft.)	4180 to 8040
Illumination Angle Difference (deg.)	15 to 17
Shadow Length Difference (%)	6.8 to 6.5
Resolution Difference (%)	0

Table V System and Image Parameters for the Two Flight Technique

System Parameters	
Image Width (mi.)	2.5
Aircraft Altitude (ft.)	30,000
Beam #1 (Flight #1)	
Elevation Angle (deg.)	38.0 to 30.2
Azimuth Angle (deg.)	90
Beam #2 (Flight #2)	
Elevation Angle (deg.)	50.0 to 38.0
Azimuth Angle (deg.)	90
Image Parameters	
Parallax Sensitivity (unit parallax per unit terrain height)	0.410 to 0.200
Aircraft Position Difference (ft.)	> 13,200
Illumination Angle Difference (deg.)	12.0 to 7.8
Shadow Length Difference (%)	52.5 to 34.4
Resolution Difference (%)	24.4 to 22.5

The various advantages and disadvantages for each technique as discussed previously in Sec. I are apparent from these tables. Also of importance for this analysis is the height measuring capability of the three techniques. This parameter is difficult to establish because there has been very little experimental work done with stereo radar images. The height measuring capability is primarily a function of the resolution of the radar images, the smallest measurable amount of resolution cell shift, and the parallax sensitivity. This topic is discussed in detail in Ref. 10. For the purpose of this analysis the average theoretical height measuring capability for the system parameters in Tables III, IV, and V is assumed to be 50 feet.

B. COORDINATE AND ERROR DEFINITIONS

Throughout this investigation, a reference coordinate system (X, Y, Z) is used as shown in Fig. 34. The X direction is defined by the aircraft's flight track with no error present. The X,Y plane is defined by the aircraft's altitude with no error present. The Y axis is perpendicular to the flight track. For some derivations, it will be convenient to have the Y axis pass through the orthographic location of the terrain point being investigated.

The errors inherent in any airborne radar mapping technique can be assigned to basic categories. These include aircraft angular errors, aircraft position errors, data imaging errors, data reconstruction errors, and hardware errors.

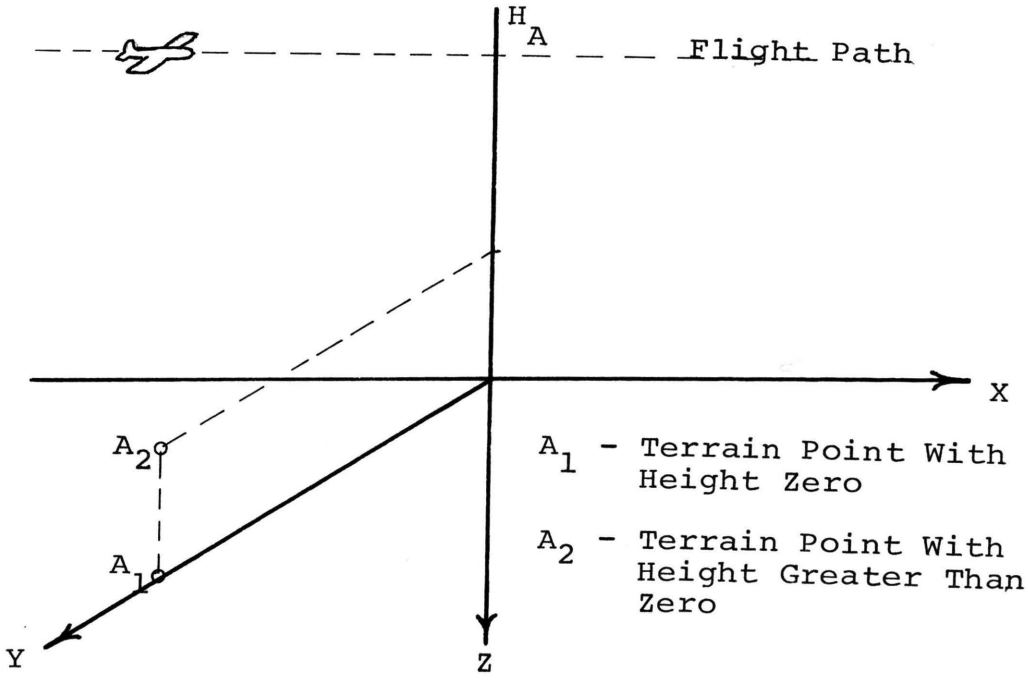

Fig. 34 Definition of the General Reference Frame

The aircraft angular errors occur when the aircraft encounters roll, pitch, and yaw angles which sensing instruments or stabilizing elements do not detect and/or correct exactly. In order to define these angles, a set of unit vectors is defined with respect to the aircraft. These vectors, $\hat{D}$, $\hat{C}$, and $\hat{P}$, are defined in Fig. 35. The aircraft angular errors are defined in Fig. 36. It is important to preserve the order when defining these angles. Changing the order results in a different set of angles. The order chosen here is yaw, θ_Y, pitch, θ_P, and roll, θ_R.

The aircraft position errors are due to errors in the aircraft's position which are undetected by the navigation system. These errors are shown in Fig. 37. The errors are: along-track aircraft position error ΔX_A, cross-track aircraft position error ΔY_A, and aircraft altitude error ΔH_A.

The data imaging errors occur because of the unknown inaccuracies in the sweep generating and film processing equipment. These are shown in Fig. 38, where a general image point is shown with and without error. As shown in the figure, ΔX_I represents the along-track imaging error and ΔY_I is the cross-track imaging error.

The data reconstruction errors occur because of the inability to physically interpret the data, i.e., measure the data coordinates without error. These errors are not considered individually, but are grouped together with the data imaging errors because their effect upon system performance is identical.

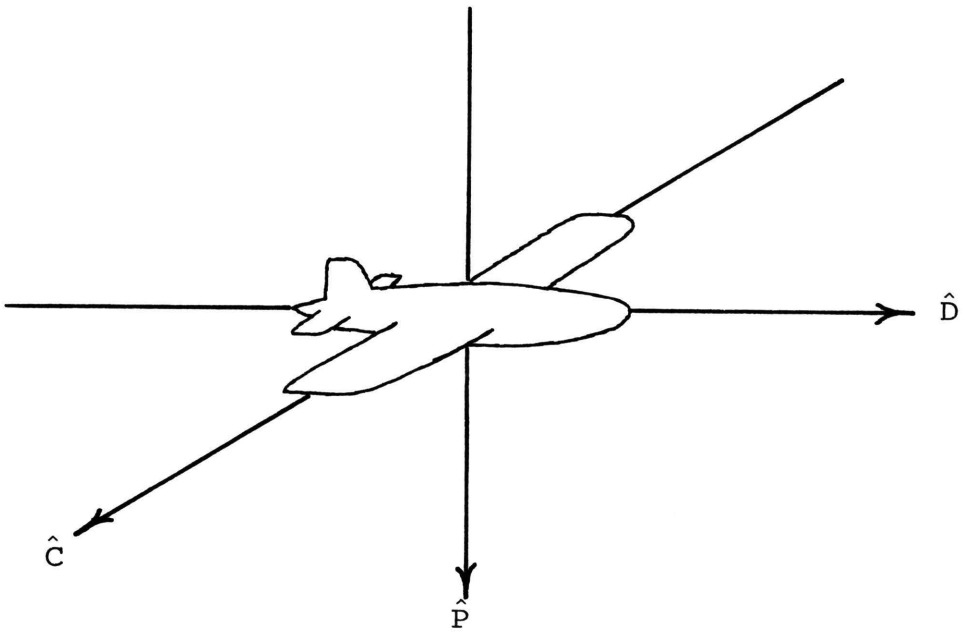

Fig. 35 Definition of $\hat{D}$, $\hat{C}$, and $\hat{P}$ Unit Vectors Referenced to the Aircraft Position

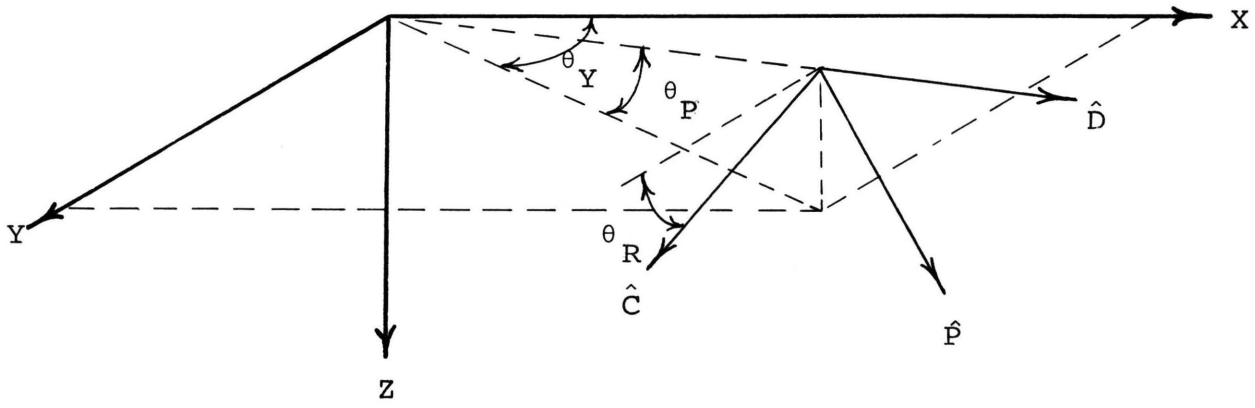

Fig. 36 Definition of the Aircraft Angular Errors θ_Y, θ_P, and θ_R

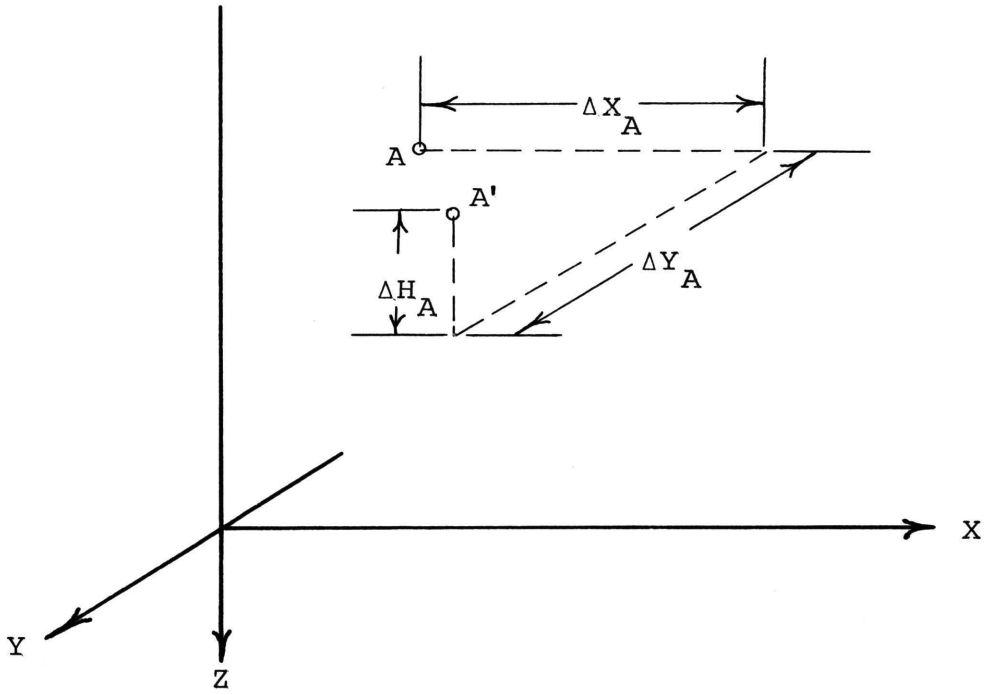

Fig. 37 Definition of the Aircraft Position Errors ΔX_A, ΔY_A, and ΔH_A

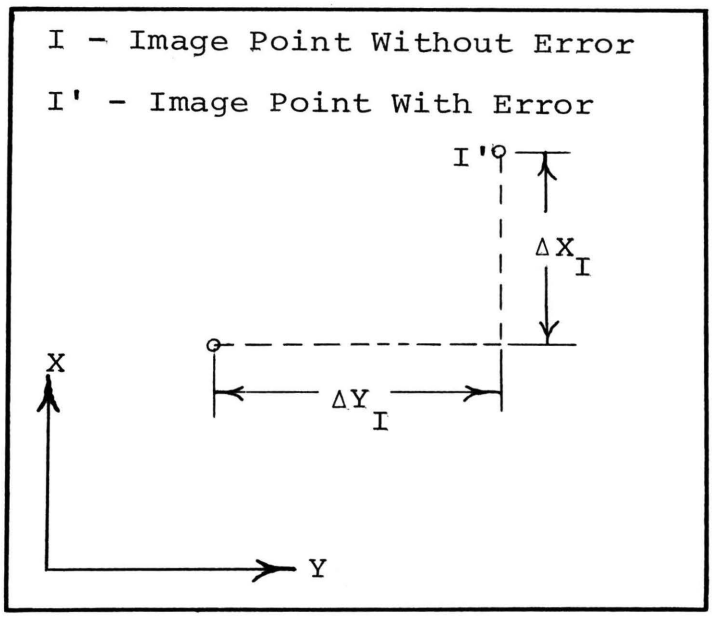

Fig. 38 Definitions of Data Imaging Errors ΔX_I and ΔY_I

Miscellaneous hardware errors include such things as array mounting errors, collimation, divergence of the radar beams from their ideal shapes, conical beam cone angle error (for the improved single flight technique), and slant range recording error. The effect of nonideal beam shapes is not investigated here. This should not prove to be a very large problem if the beams are appropriately calibrated. The slant-range error, ΔR, is shown in Fig. 39. Note that R' is the recorded slant range. The conical beam cone angle error $\Delta\phi$ and the resulting cone angle with error ϕ' are shown in Fig. 40. This error results from incorrect phasing of the electronically phased array used for the improved single flight technique.

In this discussion, the term undetected error has been used several times. The reason for this is that only undetected errors cause a degradation in the data. As will become apparent later when the error sensitivities are considered, corrections can be made for any detected error. Also, it is assumed that all errors except mounting and collimation errors can be modeled as the sum of two independent errors. The first of these is termed the short-term error and results from the inability of the sensing or stabilizing devices to detect and/or correct errors as they occur. The second term of the sum is called the long-term error and results from the inability of practical sensing devices to maintain as high a degree of accuracy over a long period of time as is possible over a short period of time

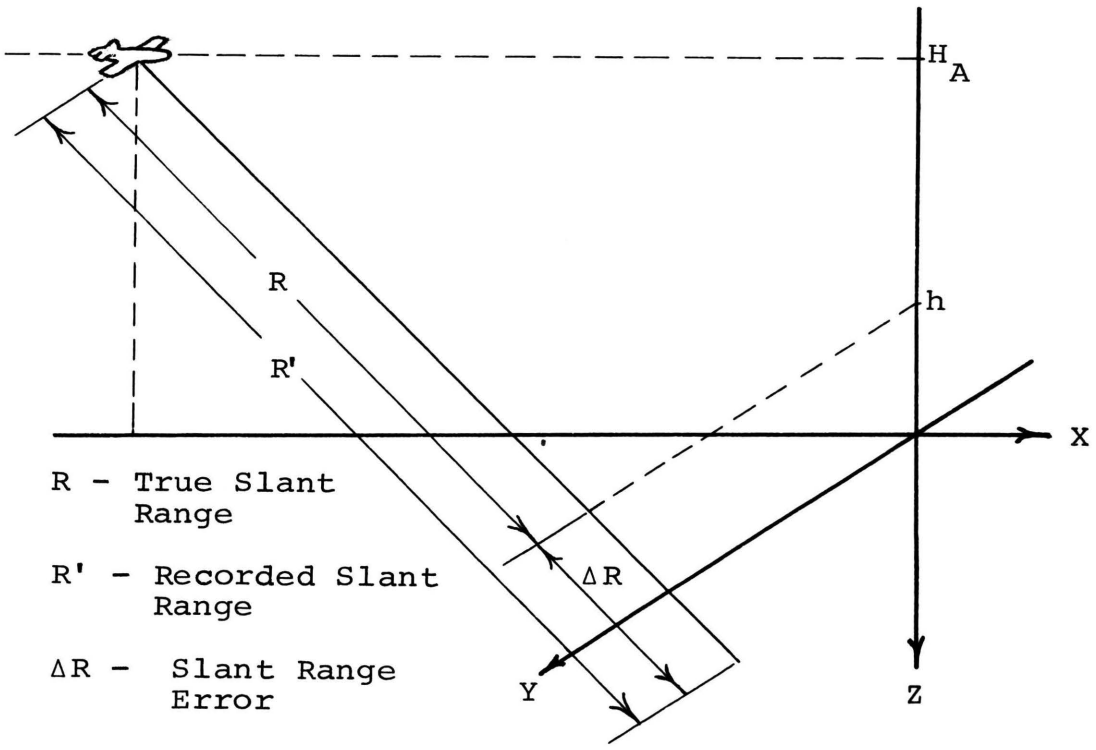

Fig. 39 Definition of Slant Range Error ΔR

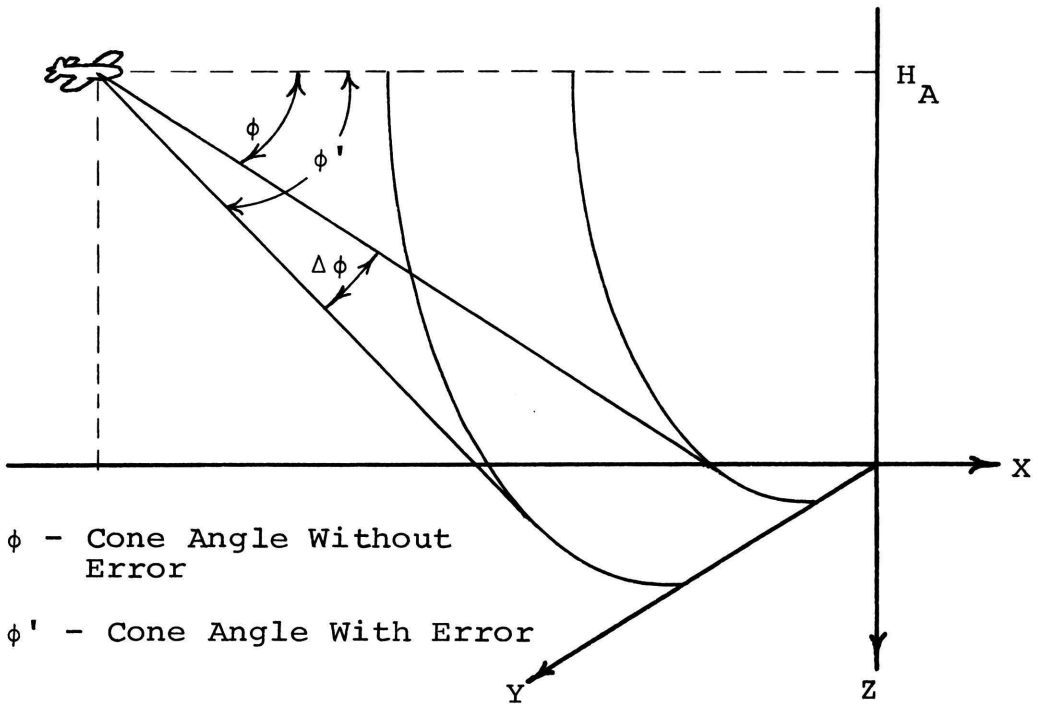

Fig. 40 Definition of Conical Beam Cone Angle Error, $\Delta\phi$

due to drifts. Each error source is considered separately for each illumination so short-term errors can be analyzed. As an example, the slant-range error ΔR will be present for both illuminations and will be termed ΔR_1 and ΔR_2 and will be treated as two separate error sources in the analysis.

It is not necessary to know the distributions for the errors. It is only necessary to be able to assign a standard deviation and mean to each individual error. This is true because all errors are assumed statistically independent with no single error predominating so the Central Limit Theorem may be applied and the resulting system performance may be defined by the mean and standard deviation of the error.

C. IMPROVED SINGLE FLIGHT TECHNIQUE

In this section the error analysis for the improved single flight technique is considered. The equations for the image coordinates including the effects of errors for both illuminations are derived. These are the equations used in the computer simulations to compute error sensitivities. The sensitivities are shown and also used to determine the optimum reconstruction equations and the resulting stereo model errors.

1. FAN BEAM AND CONICAL BEAM ERROR EQUATIONS

Prior to the consideration of the specific error analysis equations, the aircraft position with errors present must be described. To include the entire effect of these errors it

is necessary to calculate the conical beam and fan beam slant ranges using

$$H'_A = H_A + \Delta H_A \tag{63}$$

$$y' = y - \Delta Y_A \tag{64}$$

where ΔH_A represents the aircraft height error and ΔY_A represents the aircraft cross-track error as defined earlier in Fig. 37. Conversion of the slant-range data to ground-range coordinates does not involve the use of H'_A. This is because H'_A results from undetected and thus unknown error and the conversion is made with the height without error. Note that the terrain point position is altered instead of the aircraft position. This is done so that the aircraft cross-track position will remain identically zero and lead to simpler expressions for the image locations. The results are the same because the resulting image locations depend only on the terrain point offset which can be defined by the cross-track distance from the aircraft to the terrain point. The aircraft along-track position error ΔX_A does not enter into the error analysis equations, but is added after the image coordinates are determined by shifting the frame of reference appropriately.

To begin the analysis of the fan beam image, expressions for the unit vectors defined in Fig. 35 must be derived and several new quantities must be defined. It is seen in Fig.36 that $\hat{D}$ is a function only of θ_Y and θ_P and can be written

$$\hat{D} = \hat{X}(\text{Cos } \theta_P \text{Cos } \theta_Y) + \hat{Y}(\text{Cos } \theta_P \text{Sin } \theta_Y) - Z(\text{Sin } \theta_P) \quad . \quad (65)$$

The vectors $\hat{C}$ and $\hat{P}$ are affected by all three angles and are difficult to visualize. To aid in their derivation, the vectors $\hat{C}_0$ and $\hat{P}_0$ are defined. These vectors are equal to $\hat{C}$ and $\hat{P}$, respectively, when θ_R is equal to zero. Fig. 41 shows the X, Y plane to aid in writing $\hat{C}_0$. It is apparent that $\hat{P}_0$ follows in much the same manner. Thus

$$\hat{C}_0 = \hat{X}(-\text{Sin } \theta_Y) + \hat{Y}(\text{Cos } \theta_Y) \quad (66)$$

$$\hat{P}_0 = \hat{X}(\text{Sin } \theta_P \text{Cos } \theta_Y) + \hat{Y}(\text{Sin } \theta_P \text{Sin } \theta_Y) + \hat{Z}(\text{Cos } \theta_P) \quad . \quad (67)$$

Fig. 42 shows the C_0, P_0 plane. From this, it is possible to write expressions for $\hat{C}$ and $\hat{P}$:

$$\begin{aligned}
\hat{C} &= \hat{C}_0(\text{Cos } \theta_R) + \hat{P}_0(\text{Sin } \theta_R) \\
&= \hat{X}(-\text{Cos } \theta_R \text{Sin } \theta_Y + \text{Sin } \theta_P \text{Sin } \theta_R \text{Cos } \theta_Y) \\
&\quad + \hat{Y}(\text{Cos } \theta_R \text{Cos } \theta_Y + \text{Sin } \theta_P \text{Sin } \theta_R \text{Sin } \theta_Y) \\
&\quad + \hat{Z}(\text{Cos } \theta_P \text{Sin } \theta_R) \qquad (68)
\end{aligned}$$

$$\begin{aligned}
\hat{P} &= \hat{C}_0(-\text{Sin } \theta_R) + \hat{P}_0(\text{Cos } \theta_R) \\
&\quad + \hat{X}(\text{Sin } \theta_R \text{Sin } \theta_Y + \text{Cos } \theta_R \text{Sin } \theta_P \text{Cos } \theta_Y) \\
&\quad + \hat{Y}(-\text{Sin } \theta_R \text{Cos } \theta_Y + \text{Cos } \theta_R \text{Sin } \theta_P \text{Sin } \theta_Y) \\
&\quad + \hat{Z}(\text{Cos } \theta_P \text{Cos } \theta_R) \quad . \qquad (69)
\end{aligned}$$

It is possible to simplify these equations for $\hat{D}$, $\hat{C}$, and $\hat{P}$

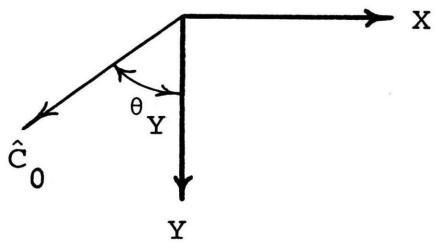

Fig. 41 Plan View to Aid in Deriving an Expression for $\hat{C}_0$ Unit Vector

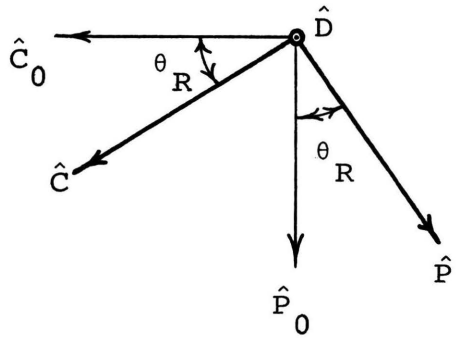

Fig. 42 Plan View to Aid in Deriving Expressions for $\hat{C}$ and $\hat{P}$ Unit Vectors

for simulation purposes by noting that only one error quantity will be allowed to be nonzero at any given time; therefore, the product of two or more sines of error angles is identically zero. Also, a mixed term such as $\text{Cos } \theta_R \text{Sin } \theta_Y$ can be written simply $\text{Sin } \theta_Y$ without loss of generality. Thus the expressions for the unit vectors become

$$\hat{D} = \hat{X}(\text{Cos } \theta_P \text{Cos } \theta_Y) + \hat{Y}(\text{Sin } \theta_Y) + \hat{Z}(-\text{Sin } \theta_P)$$

$$\equiv \hat{X}D_X + \hat{Y}D_Y + \hat{Z}D_Z \tag{70}$$

$$\hat{P} = \hat{X}(\text{Sin } \theta_P) + \hat{Y}(-\text{Sin } \theta_R) + \hat{Z}(\text{Cos } \theta_R \text{Cos } \theta_P)$$

$$\equiv \hat{X}P_X + \hat{Y}P_Y + \hat{Z}P_Z \tag{71}$$

$$\hat{C} = \hat{X}(-\text{Sin } \theta_Y) + \hat{Y}(\text{Cos } \theta_R \text{Cos } \theta_Y) + \hat{Z}(\text{Sin } \theta_R)$$

$$\equiv \hat{X}C_X + \hat{Y}C_Y + \hat{Z}C_Z \, . \tag{72}$$

Next, it is necessary to define a unit vector $\hat{B}$ which lies in the D, C plane and is perpendicular to the fan beam array as shown in Fig. 43. Note that θ_1 is the fan beam azimuth angle. It is seen that

$$\hat{B} = \hat{D}(\text{Cos } \theta_1) + \hat{C}(\text{Sin } \theta_1)$$

$$= \hat{X}(\text{Cos } \theta_1 \text{Cos } \theta_P \text{Cos } \theta_Y - \text{Sin } \theta_Y \text{Sin } \theta_1)$$

$$+ \hat{Y}(\text{Cos } \theta_1 \text{Sin } \theta_Y + \text{Sin } \theta_1 \text{Cos } \theta_R \text{Cos } \theta_Y)$$

$$+ \hat{Z}(-\text{Cos } \theta_1 \text{Sin } \theta_P + \text{Sin } \theta_1 \text{Sin } \theta_R)$$

$$\equiv \hat{X}B_X + \hat{Y}B_Y + \hat{Z}B_Z \, . \tag{73}$$

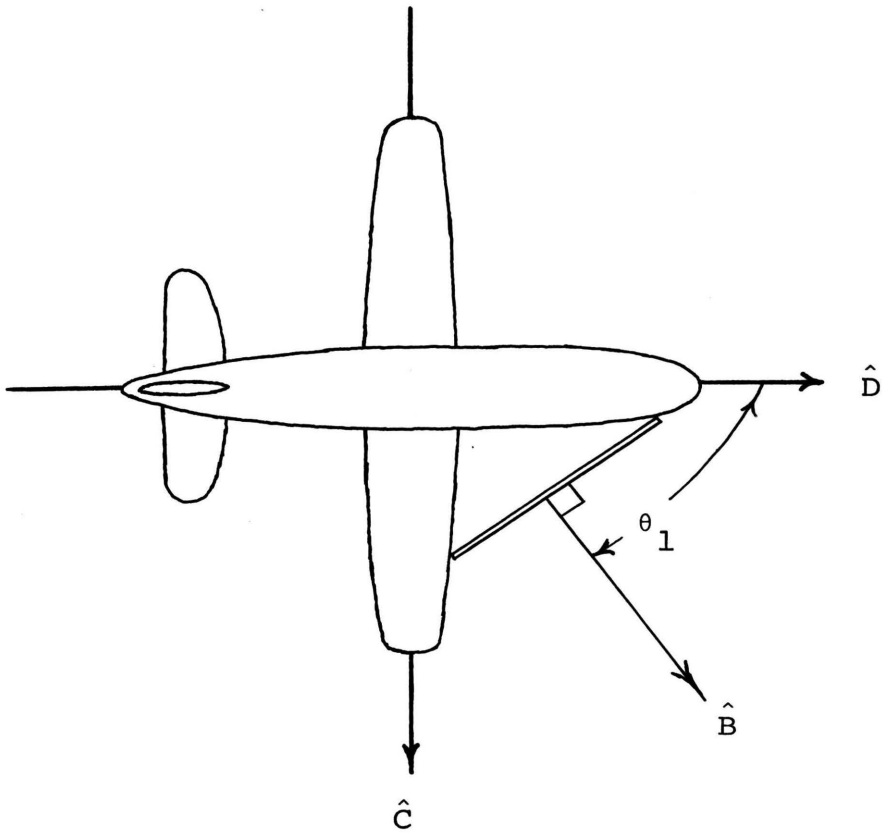

Fig. 43 Definition of $\hat{B}$, the Unit Vector Contained in Both the C, D Plane and the Fan Beam Illumination Plane

With the derivation of the unit vectors $\hat{B}$ and $\hat{P}$, expressions have been defined which uniquely describe the fan beam illumination plane relative to the X, Y reference plane, provided the aircraft position is known. This last constraint is necessary because definition of a plane requires two vectors and a point on the plane.

To arrive at the final solution, it is necessary only to constrain the terrain point to lie within the illumination plane. To demonstrate this, the aircraft position vector $\bar{H}$ and the terrain point position vector $\bar{A}$ are defined

$$\bar{A} = \hat{Y}y' - h\hat{Z} \tag{74}$$

$$\bar{H} = \hat{X}X_{Al} - H_A'\hat{Z} \tag{75}$$

where the terrain point height h and aircraft altitude H_A' are treated as positive quantities when located on the -Z axis. The aircraft, terrain point, and the illumination plane are shown in Fig. 44. Note that the Y axis is defined by the terrain point location. By means of vector algebra, it is seen that

$$\bar{A} = \bar{H} + r\hat{P} + s\hat{B} \tag{76}$$

where r and s are constants to be determined. From this expression three independent equations can be written, one for each dimension. The equations are

$$0 = X_{Al} + rP_X + sB_X \tag{77}$$

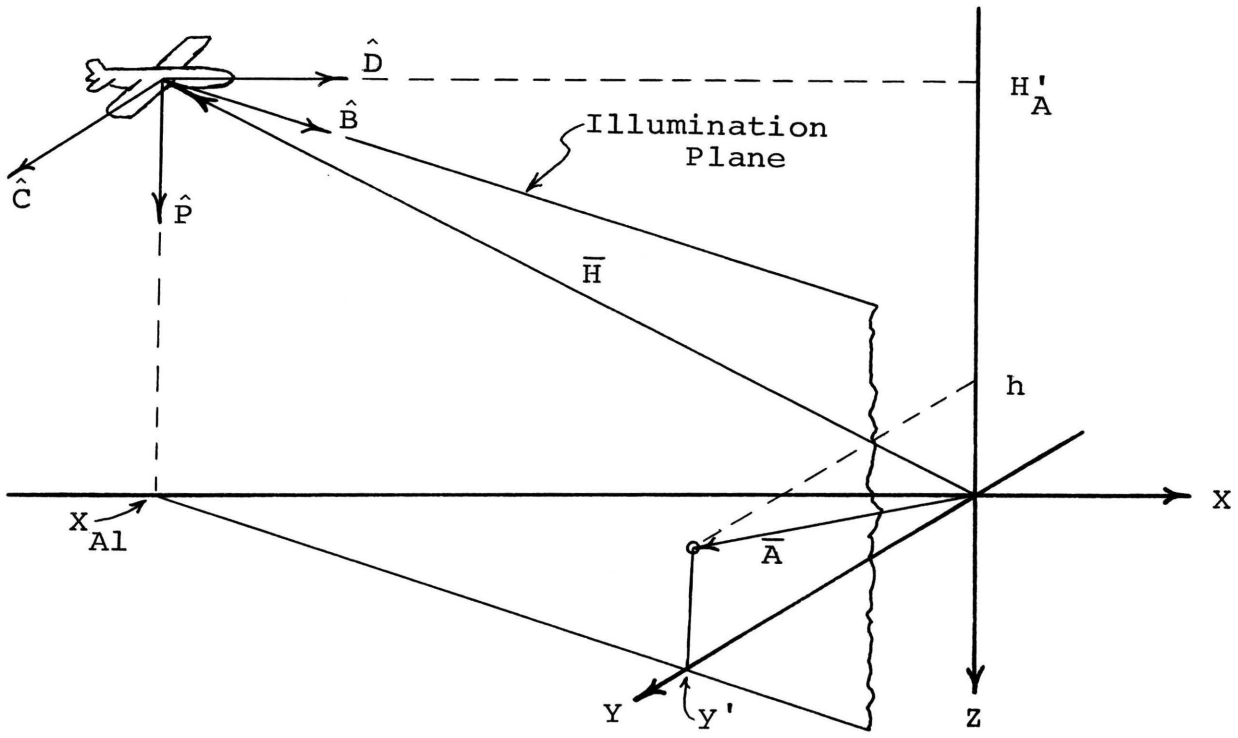

Fig. 44 Illustration of the Fan Beam Illumination Plane, Aircraft Position Vector $\bar{H}$, and Terrain Point Position Vector $\bar{A}$

$$y' = rP_Y + sB_Y \tag{78}$$

$$h = H'_A - rP_Z - sB_Z \ . \tag{79}$$

These equations can be solved simultaneously to obtain values for the unknown quantities r, s, and X_{Al}. These solutions are

$$X_{Al} = \frac{y'(B_X P_Z - B_Z P_X) + (H'_A - h)(B_Y P_X - B_X P_Y)}{B_Z P_Y - B_Y P_Z} \tag{80}$$

$$r = \{y'B_Z - B_Y(H'_A - h)\}/(B_Z P_Y - B_Y P_Z) \tag{81}$$

$$s = \{P_Y(H'_A - h) - y'P_Z\}/(B_Z P_Y - B_Y P_Z) \ . \tag{82}$$

The meaning of aircraft position during fan beam illumination, X_{Al}, is apparent from previous discussions, but the physical meaning of r and s is not direct and requires some explanation. Refer to Fig. 45, where a plan view of the P, B plane (illumination plane) is shown. The point A denotes the intersection of the terrain point with this plane. Analysis shows that the coordinates describing the point in this plane are (r, s). Thus, the slant range to the terrain point is given by

$$R_1 = (r^2 + s^2)^{\frac{1}{2}} \ . \tag{83}$$

Before continuing, the effect of the fan beam slant-range error, ΔR_1, must be included. To do this, the previously calculated slant range is altered by adding the slant-range error which gives

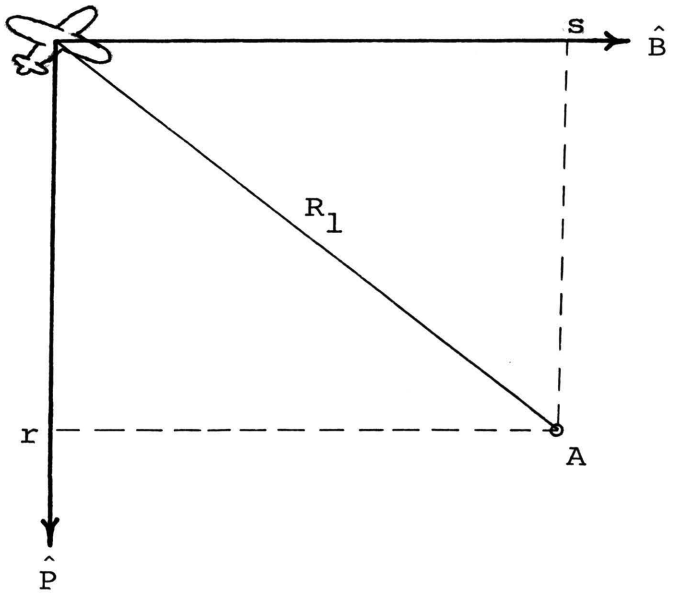

Fig. 45 Interpretation of the Parameters r and s

$$R'_1 = (r^2 + s^2)^{\frac{1}{2}} + \Delta R_1 \quad . \tag{84}$$

The slant-range image parameters for the fan beam image have been determined and are given by Eqns. 80, 81, 82, and 84. These slant-range quantities must be converted to ground-range terms using the equations previously derived (Eqns. 1, 2, and 3) with the correct value of H_A since the conversion is performed without knowledge of the aircraft altitude error. It is necessary to subtract ΔX_A from the expression for X_1 to include the effect of aircraft along-track position error as discussed previously. Also, to include the effect of data imaging errors these expressions are further changed by adding the along-track data imaging error ΔX_I to X_1 and adding the cross-track data imaging error ΔY_I to Y_1. The final expressions for the terrain point image coordinates are

$$X_1 = X_{A1} + R_{G1}\text{Cos } \theta_1 - \Delta X_A + \Delta X_I \tag{85}$$

$$Y_1 = R_{G1}\text{Sin } \theta_1 + \Delta Y_I \tag{86}$$

where $R_{G1} = (R'^2_1 - H^2_A)^{\frac{1}{2}}$.

The analysis of the conical beam image is not as straightforward as that for the fan beam image. Attempts to derive the general solution including the effects of all angular errors have not been successful. The problem here is that the conical beam case does not lend itself to vector methods so that the only alternative methods involve many radicals. The problem is further complicated by the way the

aircraft position during illumination varies with terrain point position and error quantities. To overcome this, two different solutions are derived. One solution is valid for a yaw angle error while the second solution is valid for a pitch angle error. There is no special solution necessary when a roll angle error is present since no image error results due to the symmetry of the conical beam illumination about the D axis.

Refer to Fig. 46 for the discussion of the analysis of the conical beam case with a yaw error. The quantity ϕ_2' refers to the conical beam cone angle including the effect of incorrect electrical phasing as defined previously. The other quantities are defined to aid in the analysis. It should be noted that the occurence of radicals requires treating the aircraft position during conical beam illumination, X_{A2}, as a magnitude. In actuality, the quantity is always less than zero with the reference frame used here. Also note that again the terrain point orthographic location is used to define the Y axis and that the appropriate terms for the aircraft and terrain point position are used in order to include the aircraft position errors. Referring to Fig. 46, the equations for L, M, and N can be written

$$L = (X_{A2}^2 + y'^2)^{\frac{1}{2}} \tag{87}$$

$$M = \{(H_A' - h)^2 + L^2\}^{\frac{1}{2}} \tag{88}$$

$$N = M\text{Cos } \phi_2' \ . \tag{89}$$

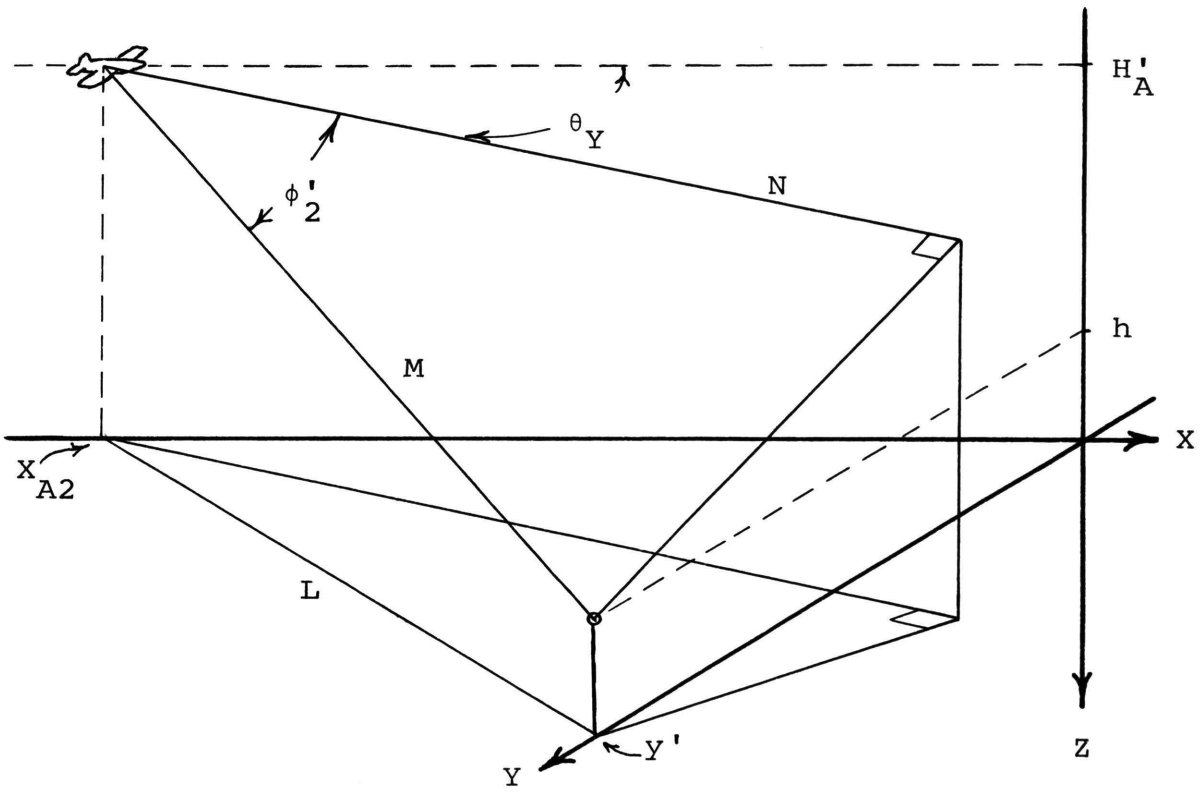

Fig. 46 Conical Beam Geometry Including the Effect of a Yaw Error

Combining these equations gives

$$N = \text{Cos } \phi_2' \{(H_A' - h)^2 + X_{A2}^2 + y'^2\}^{\frac{1}{2}} . \qquad (90)$$

It is possible to write another equation for N which is independent of Eqn. 90. This is given by

$$N = X_{A2} \text{Cos } \theta_Y + y' \text{Sin } \theta_Y . \qquad (91)$$

Both expressions for N contain only one unknown, X_{A2}. The expressions are equated, and result in a quadratic equation with the solutions

$$X = -y' \text{Sin } \theta_Y \text{Cos } \theta_Y / (\text{Cos}^2 \theta_Y - \text{Cos}^2 \phi_2') \pm \frac{\{y'^2 \text{Sin}^2 \phi_2' + (H_A' - h)^2 (\text{Cos}^2 \theta_Y - \text{Cos}^2 \phi_2')\}^{\frac{1}{2}}}{\text{Sec } \phi_2' (\text{Cos}^2 \theta_Y - \text{Cos}^2 \phi_2')} . \qquad (92)$$

The correct solution can be determined by noting that the denominator is always greater than zero and that X_{A2} must be positive when $\theta_Y = 0$. Thus, the plus sign is retained on the radical. To be consistent, X_{A2} is negated when used to designate aircraft position; therefore, the final equation for aircraft position during illumination by the conical beam is given by

$$X_{A2} = y' \text{Sin } \theta_Y \text{Cos } \theta_Y / (\text{Cos}^2 \theta_Y - \text{Cos}^2 \phi_2') - \frac{\{y'^2 \text{Sin}^2 \phi_2' + (H_A' - h)^2 (\text{Cos}^2 \theta_Y - \text{Cos}^2 \phi_2')\}^{\frac{1}{2}}}{\text{Sec } \phi_2' (\text{Cos}^2 \theta_Y - \text{Cos}^2 \phi_2')} . \qquad (93)$$

The slant range, R_2, can now be determined from X_{A2}. The

expression is obtained by combining Eqns. 87 and 88 to give

$$R_2 = M = \{X_{A2}^2 + y'^2 + (H_A' - h)^2\}^{\frac{1}{2}} . \qquad (94)$$

R_2 is altered in order to include the effect of the slant-range error ΔR. This gives

$$R_2' = \{X_{A2}^2 + y'^2 + (H_A' - h)^2\}^{\frac{1}{2}} + \Delta R . \qquad (95)$$

The solution of the conical beam case with pitch error is quite similar to the yaw error case. The method of solution is identical. That is, two independent equations for N are written. These equations are set equal and a solution for X_{A2} is obtained. Computation of the slant range follows directly by substituting X_{A2} back into one of the original equations for N. Note again that ϕ_2' is used in determining the slant-range quantities. Using the geometry shown in Fig. 47, L, M, and N are given by Eqns. 87, 88, 89, and 90 which were previously defined. The second equation for N is determined from Fig. 47 and is

$$N = X_{A2}\text{Cos } \theta_P - (H_A' - h)\text{Sin } \theta_P . \qquad (96)$$

The two equations for N are combined and solved for X_{A2} to give

$$X_{A2} = -(H_A' - h)\text{Sin } \theta_P\text{Cos } \theta_P/(\text{Cos}^2 \theta_P - \text{Cos}^2 \phi_2') - \frac{\{y'^2(\text{Cos}^2 \theta_P - \text{Cos}^2 \phi_2') + (H_A' - h)^2\text{Sin}^2 \phi_2'\}^{\frac{1}{2}}}{\text{Sec } \phi'(\text{Cos}^2 \theta_P - \text{Cos}^2 \phi_2')} . \qquad (97)$$

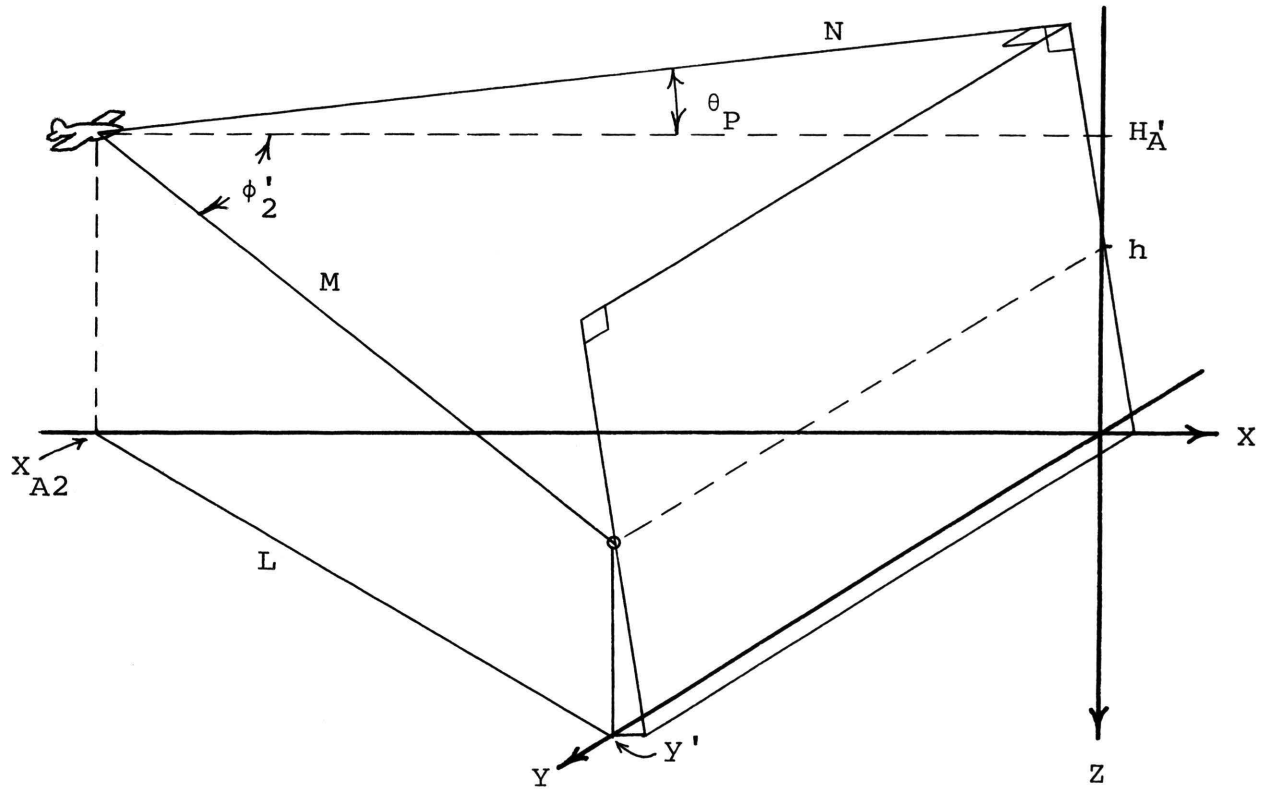

Fig. 47 Conical Beam Geometry Including the Effect of a Pitch Error

where the correct signs have been chosen as before. Again, it is possible to determine the slant range with error, R_2', by using Eqn. 95.

The expressions given by Eqns. 93, 95, and 97 represent the conical beam slant-range image parameters under any condition. When a yaw error is present Eqns. 93 and 95 are used and Eqns. 95 and 97 are used when a pitch error is present. When an aircraft position, data imaging, or any other error is present either set of equations may be used. However, in the work that follows Eqns. 93 and 95 are used to determine the effect of all errors except aircraft pitch error.

To conclude the analysis of the conical beam image, the slant-range quantities are converted to ground-range quantities. This is done with Eqns. 4, 5, and 6 which have been previously defined. Note that this calculation is made using ϕ_2 and H_A in order to include the total effect of incorrect antenna phasing and aircraft altitude error. Also, the expressions are altered, as in the fan beam case to include the effect of aircraft along-track position error ΔX_A and the data imaging errors ΔX_I and ΔY_I. Thus, the conical beam image position coordinates are

$$X_2 = X_{A2} + R_2' \text{Cos } \phi_2 + \Delta X_I - \Delta X_A \tag{98}$$

$$Y_2 = R_{G2} + \Delta Y_I \tag{99}$$

where $R_{G2} = \{(R_2' \text{Sin } \phi_2)^2 - H_A^2\}^{\frac{1}{2}}$.

The equations describing the images produced by the improved single flight technique including the effects of errors have been derived in this section. The complete set is summarized below:

Fan Beam Image

$$X_{Al} = \frac{y'(B_X P_Z - B_Z P_X) + (H'_A - h)(B_Y P_X - B_X P_Y)}{B_Z P_Y - B_Y P_Z}$$

$$r = \{y' B_Z - B_Y (H'_A - h)\}/(B_Z P_Y - B_Y P_Z)$$

$$s = \{P_Y (H'_A - h) - y' P_Z\}/(B_Z P_Y - B_Y P_Z)$$

$$R'_1 = (r^2 + s^2)^{\frac{1}{2}} + \Delta R$$

$$R_{G1} = (R'^2_1 - H^2_A)^{\frac{1}{2}}$$

$$X_1 = X_{Al} + R_{G1} \text{Cos } \theta_1 + \Delta X_I - \Delta X_A$$

$$Y_1 = R_{G1} \text{Sin } \theta_1 + \Delta Y_I$$

where

$$P_X = \text{Sin } \theta_P \qquad B_X = \text{Cos } \theta_1 \text{Cos } \theta_P \text{Cos } \theta_Y - \text{Sin } \theta_Y \text{Sin } \theta_1$$

$$P_Y = -\text{Sin } \theta_R \qquad B_Y = \text{Cos } \theta_1 \text{Sin } \theta_Y + \text{Sin } \theta_1 \text{Cos } \theta_R \text{Cos } \theta_Y$$

$$P_Z = \text{Cos } \theta_R \text{Cos } \theta_P \qquad B_Z = -\text{Cos } \theta_1 \text{Sin } \theta_P + \text{Sin } \theta_1 \text{Sin } \theta_R$$

$$y' = y - \Delta Y_A \qquad H'_A = H_A + \Delta H_A$$

Conical Beam Image

With any error except an aircraft pitch angle error

$$X_{A2} = y' \sin \theta_Y \cos \theta_Y / (\cos^2 \theta_Y - \cos^2 \phi_2') - \frac{\{y'^2 \sin^2 \phi_2' + (H_A' - h)^2 (\cos^2 \theta_Y - \cos^2 \phi_2')\}^{\frac{1}{2}}}{\sec \phi_2' (\cos^2 \theta_Y - \cos^2 \phi_2')} .$$

With pitch error only

$$X_{A2} = -(H_A' - h) \sin \theta_P \cos \theta_P / (\cos^2 \theta_P - \cos^2 \phi_2') - \frac{\{y'^2 (\cos^2 \theta_P - \cos^2 \phi_2') + (H_A' - h)^2 \sin^2 \phi_2'\}^{\frac{1}{2}}}{\sec \phi_2' (\cos^2 \theta_P - \cos^2 \phi_2')} .$$

For both cases

$$R_2' = \{X_{A2}^2 + y'^2 + (H_A' - h)^2\}^{\frac{1}{2}} + \Delta R$$

$$R_{G2} = (R'^2 \sin^2 \phi_2 - H_A^2)^{\frac{1}{2}}$$

$$X_2 = X_{A2} + R_2' \cos \phi_2 + \Delta X_I - \Delta X_A$$

$$Y_2 = R_{G2} + \Delta Y_I ,$$

where $\phi_2' = \phi_2 + \Delta\phi_2$.

2. IMAGE ERROR SENSITIVITIES

The equations summarized in the previous section give the image positions of a terrain point on each image for the improved single flight technique where all possible errors are included. These equations are used in this section

to determine the image error sensitivities and magnitudes for this technique.

A brief look at the mathematics to be used in the error analysis is instructive. Let z be a quantity of interest. Further, assume that z is a nonlinear function F of the variables $s_1, s_2, \ldots, s_n$. That is,

$$z = F(s_1, s_2, \ldots, s_n) \ . \tag{100}$$

An expression for the total differential of z is given by

$$dz = \frac{\partial z}{\partial s_1} ds_1 + \frac{\partial z}{\partial s_2} ds_2 + \ldots + \frac{\partial z}{\partial s_n} ds_n \ . \tag{101}$$

If $ds_1, ds_2, \ldots, ds_n$ are replaced by the incremental values $\Delta s_1, \Delta s_2, \ldots, \Delta s_n$, then the incremental change in z, Δz, is

$$\Delta z = \frac{\partial z}{\partial s_1} \Delta s_1 + \frac{\partial z}{\partial s_2} \Delta s_2 + \ldots + \frac{\partial z}{\partial s_n} \Delta s_n + \varepsilon_1 \Delta s_1 + \varepsilon_2 \Delta s_2 + \ldots + \varepsilon_n \Delta s_n \tag{102}$$

where $\varepsilon_1, \varepsilon_2, \ldots, \varepsilon_n$ represent values approaching zero as $\Delta s_1, \Delta s_2, \ldots, \Delta s_n$ approach zero. For this error analysis a good approximation can be obtained by limiting the size of $\Delta s_1, \Delta s_2, \ldots, \Delta s_n$ so that $\varepsilon_1, \varepsilon_2, \ldots, \varepsilon_n$ are negligible. If the partials exhibit very small variations in the region of parameter variation of interest, then it is possible to consider them constant and write

$$\Delta z \approx a_1 \Delta s_1 + a_2 \Delta s_2 + \ldots + a_n \Delta s_n \tag{103}$$

where the expressions $a_1, a_2, \ldots, a_n$ are referred to as

sensitivities. If Δs_1, Δs_2, ..., Δs_n are independent random variables representing errors in each of the variables, then Δz is a random variable which represents the error in the quantity z, and it follows that for large n the Central Limit Theorem can be applied to give the variance of Δz as

$$\sigma^2_{\Delta z} = \sum_{i=1}^{n} a_i^2 \sigma^2_{\Delta s_i} \quad . \tag{104}$$

The sensitivities, a_i, are the partial derivatives of the quantity z with respect to each of its variable parameters. A glance at the previously derived equations for the image position coordinates shows that the calculation of the partial derivatives would be a very difficult and time consuming task. Instead of doing this an alternate approach is taken. A computer program is written which uses the equations noted previously to determine image positions. This program is given a specific terrain point location and calculates the corresponding image positions. A single error is added and the positions are calculated again. As an example, consider the calculations corresponding to X_1. Call the first calculation without error X_1 and the second calculation, which includes the effect of an error ΔE, X_1'. Then the sensitivity a_1 as defined above is given by the approxmation to the partial derivative which is

$$a_1 = (X_1' - X_1)/\Delta E \quad . \tag{105}$$

If the error is kept small enough then these quantities will give a good approximation. A flow chart describing

the operation of the simulation program used is given in Fig. 48 and the program listing and a sample output are given in the Appendix.

The plots of Figs. 49, 50, 51, and 52 show the variation of X_1, Y_1, X_2, and Y_2 with each error quantity as a function of terrain point cross-track position for the set of system parameters given in Table III. The reason these quantities are displayed as a function of cross-track distance is because their only variation is with cross-track distance. Variation with terrain point altitude in all cases is negligible. Note that an additional subscript (1 for fan beam, 2 for conical beam) has been added to the error quantity identifiers to indicate the illumination to which they apply.

The plots indicate considerable similarity between the conical beam image coordinate sensitivities and the fan beam image coordinate sensitivities. The only major deviation between the two is in the fact that θ_R results in no error for the conical beam case. As noted earlier, this is due to the symmetry of the conical beam about the D axis around which θ_R is defined. A comparison of the equations used to arrive at the sensitivities gives no hint of this similarity between the conical beam and the fan beam cases. The similarity results from the fact that ϕ_2 is chosen so large, $\phi_2 = 75^o$ for the case being considered here, that the conical beam illumination across the swath approaches a plane. The very slight difference for sensitivities in the two cases results primarily from the fact that, with no error present, the aircraft

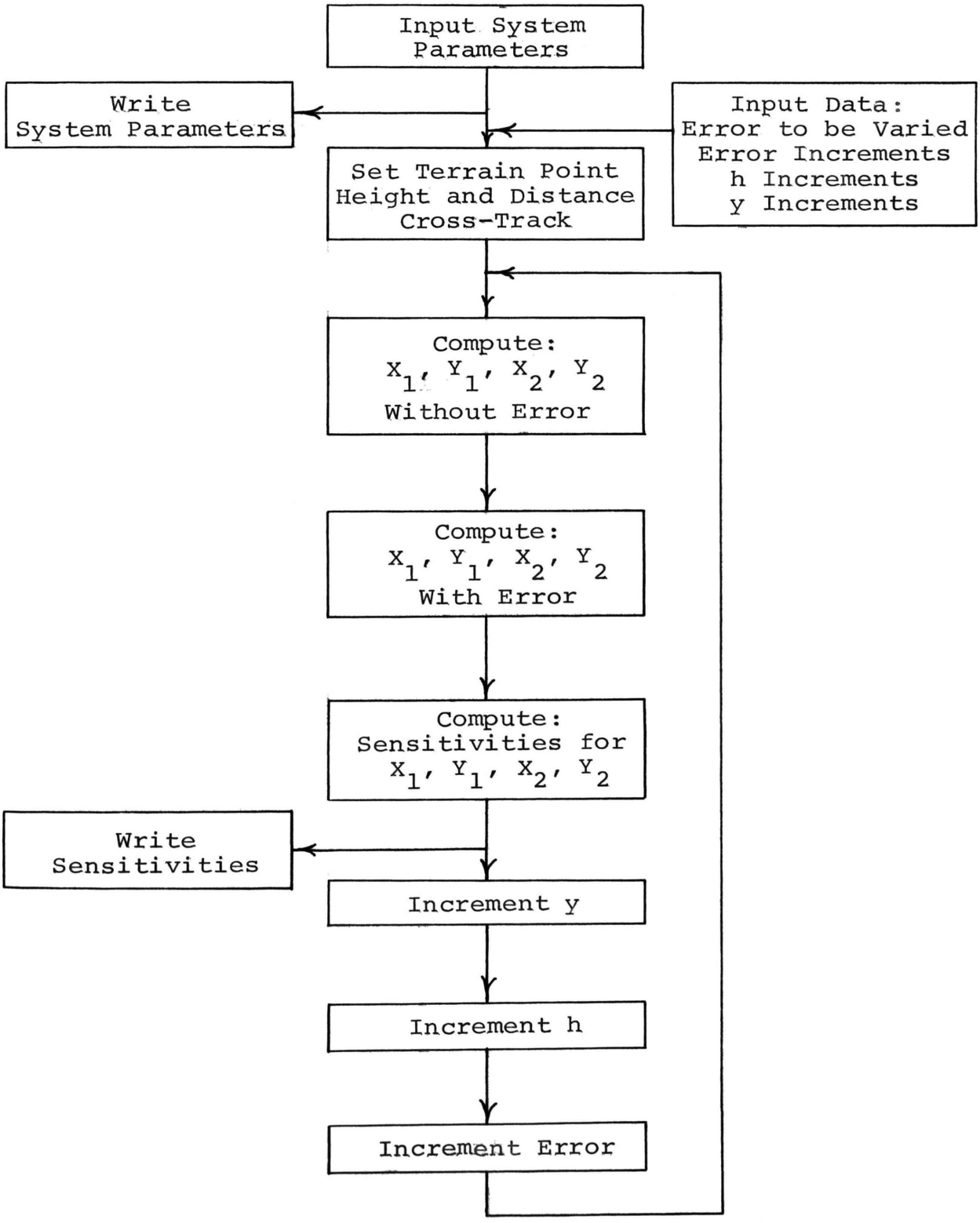

Fig. 48 Flow Chart of Computer Program Used to Obtain Error Sensitivities of Image Coordinates

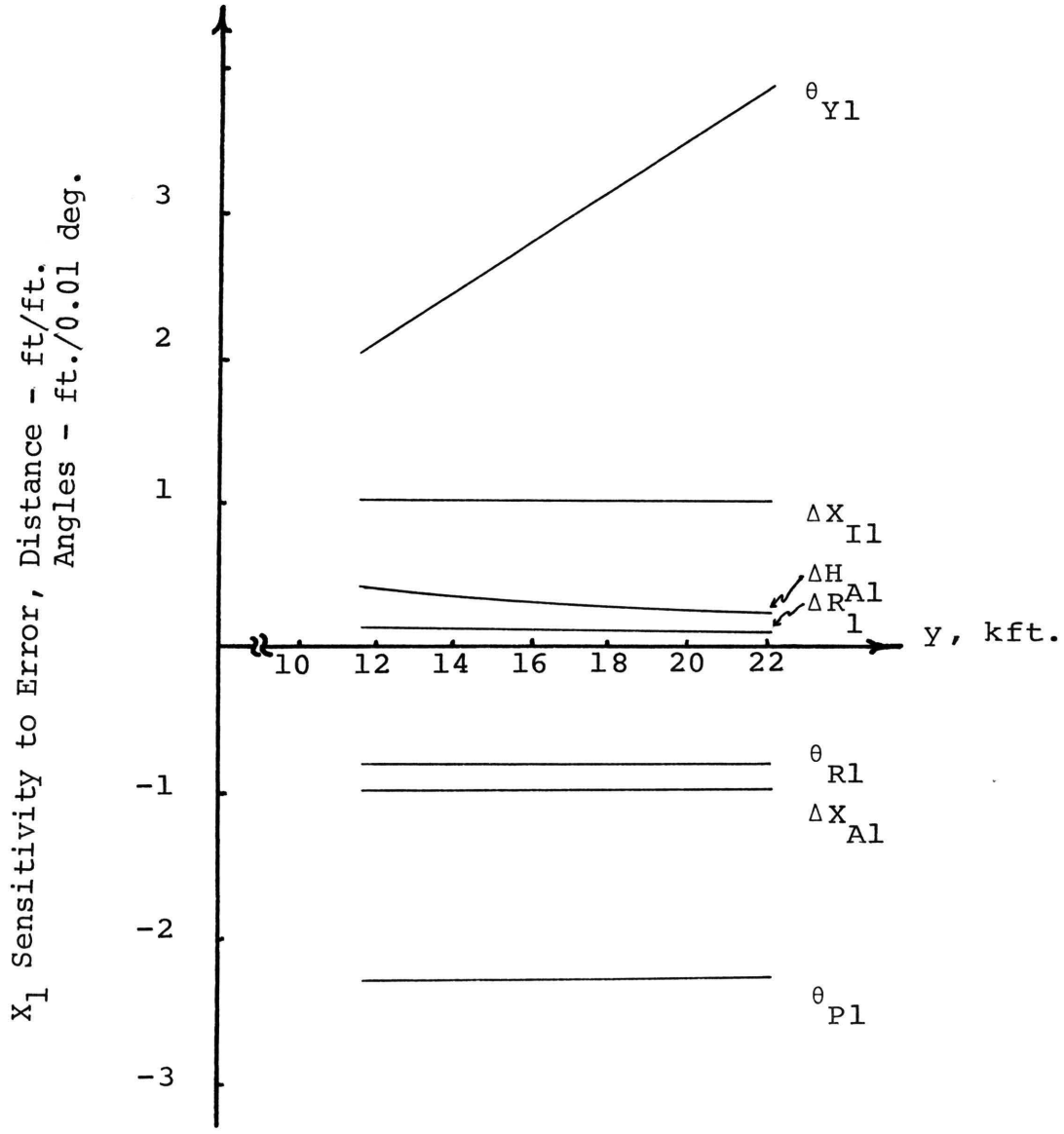

Fig.49 Error Sensitivities of Image Position Coordinate X_1

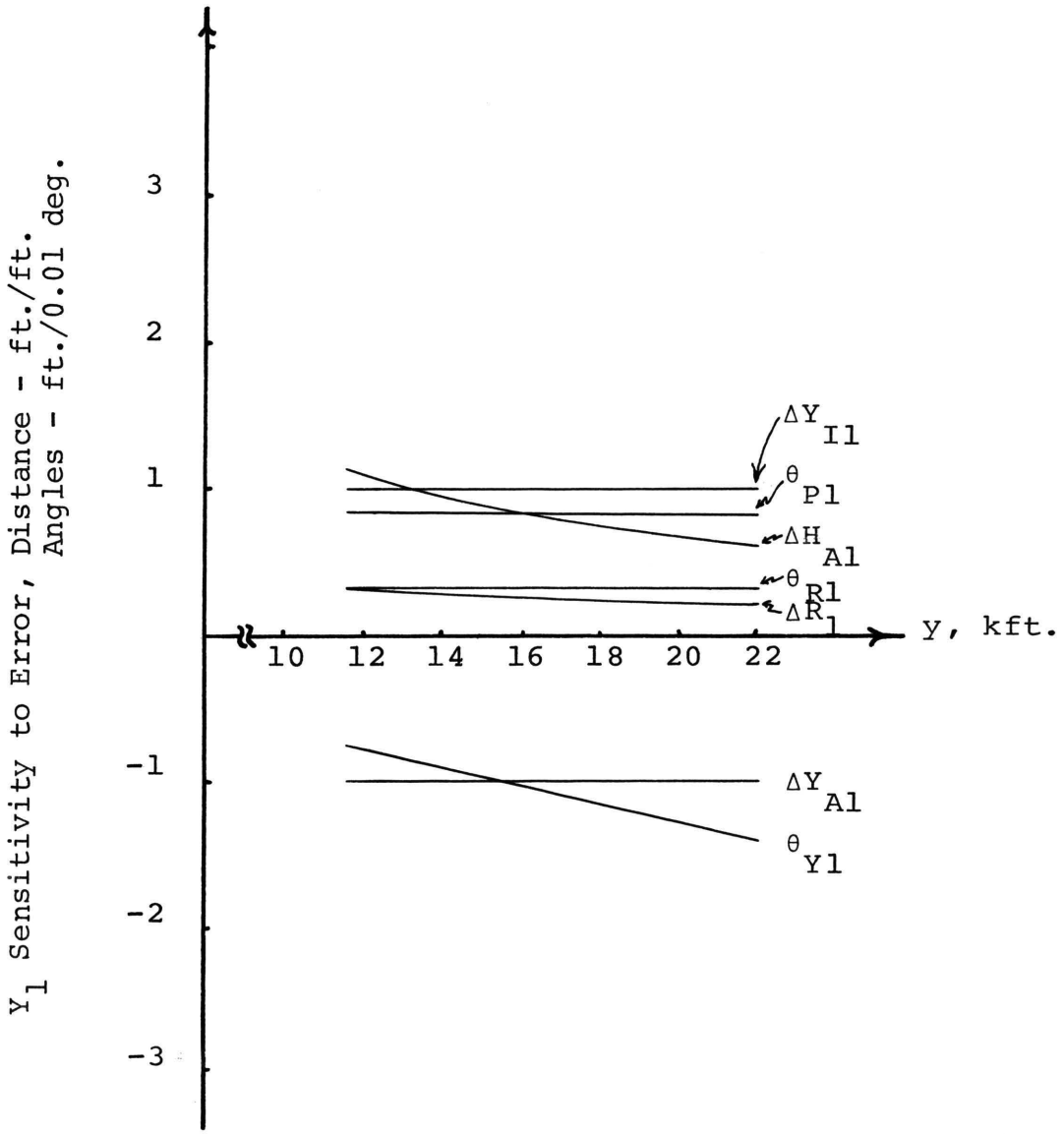

Fig. 50 Error Sensitivities of Image Position Coordinate Y_1

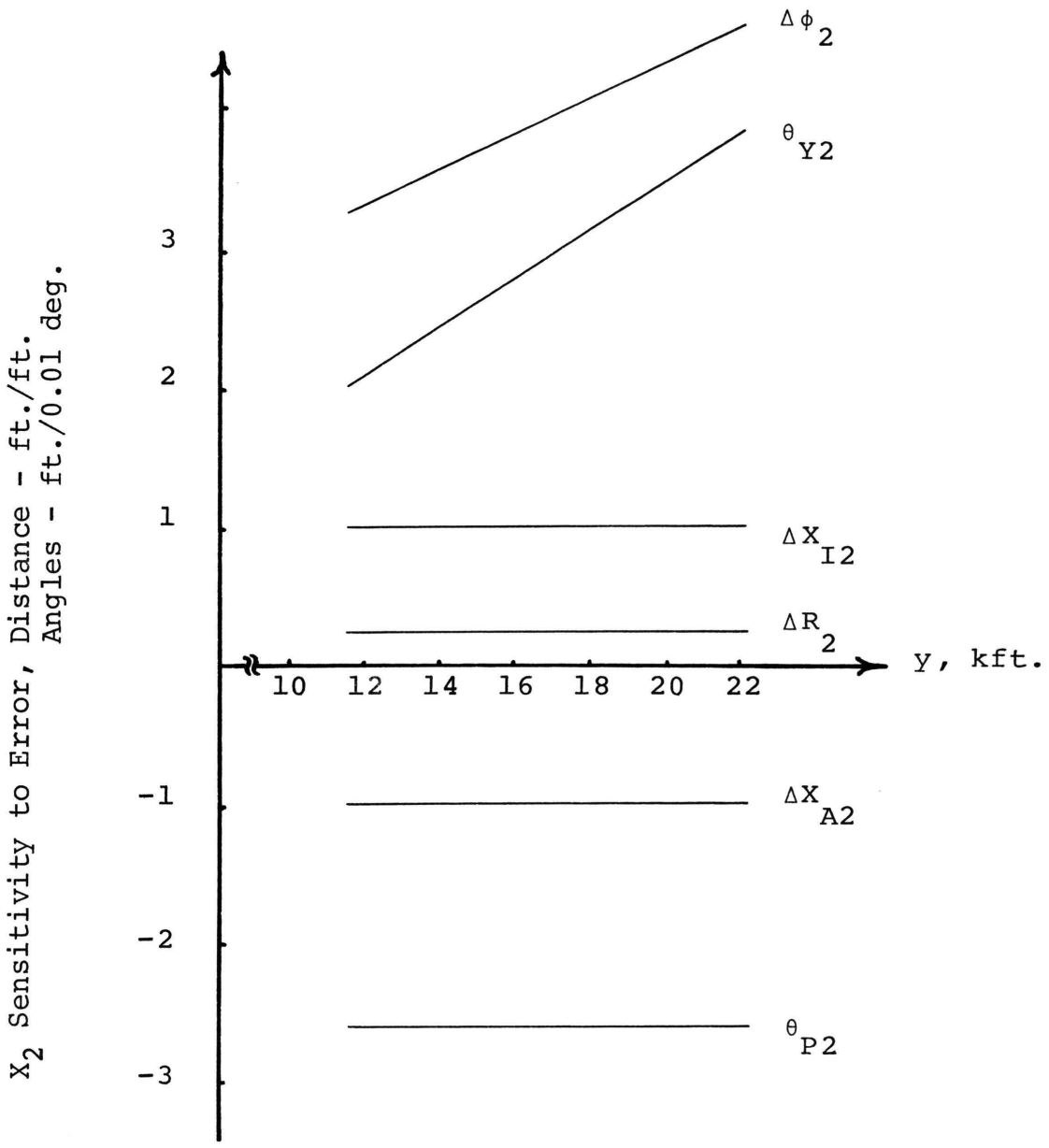

Fig. 51 Error Sensitivities of Image Position Coordinate X_2

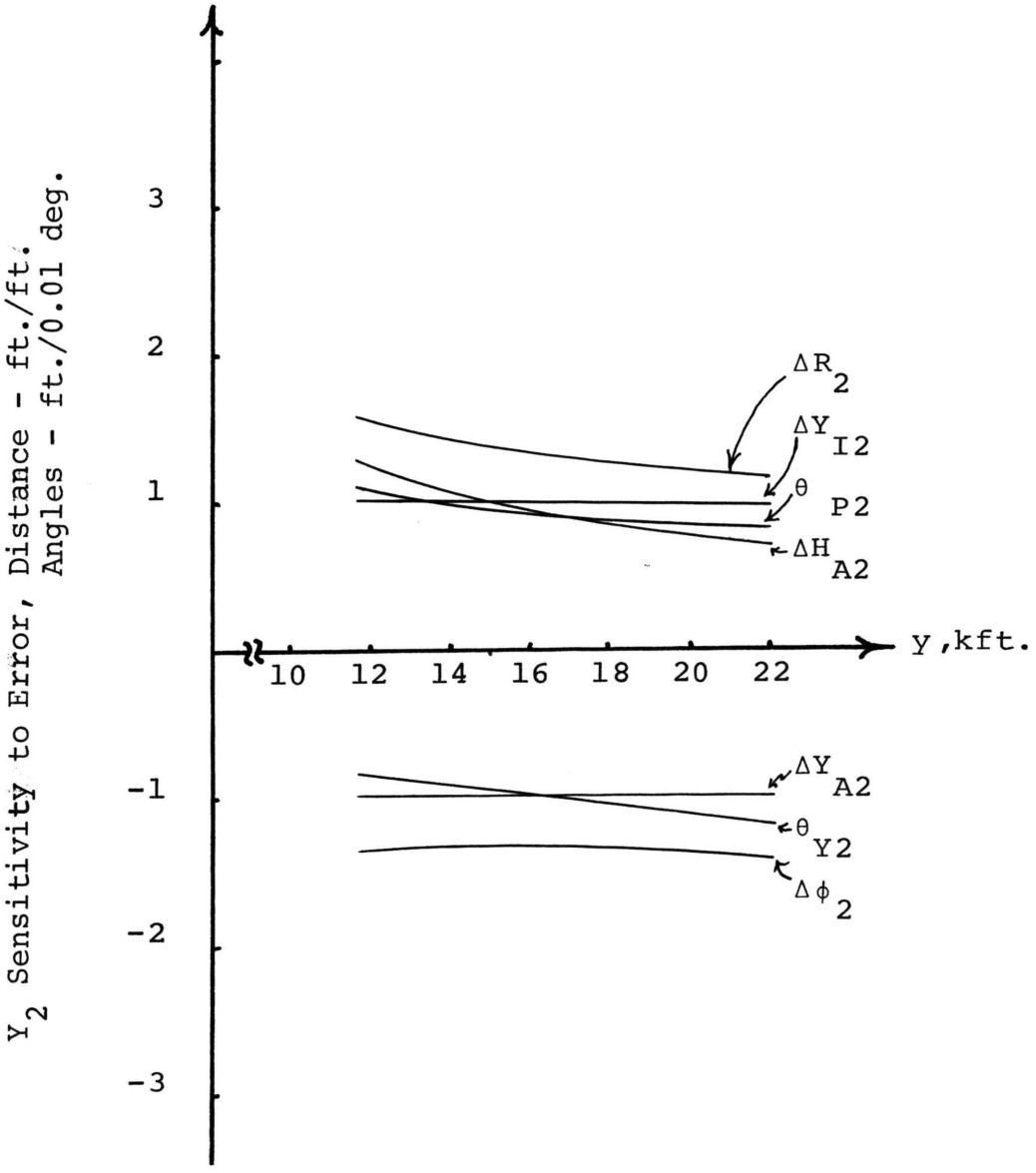

Fig. 52 Error Sensitivities of Image Position Coordinate Y_2

along-track position during conical beam illumination is a function of both aircraft altitude and terrain point height. This is not true in the fan beam case. Even though the introduction of any aircraft angular error causes the aircraft position during fan beam illumination to become a function of terrain point height and aircraft altitude, the effect is still nearly negligible. As a final point, it is noted that the sensitivities of all errors are shown in the figures except for Y_1 with respect to ΔH_{A2}. This sensitivity is less than 0.01 ft./ft. and so its contribution is negligible.

In several cases the sensitivities are a function of the cross-track distance. This is particularly true of the contribution of θ_Y. It is noted from the plot that this error sensitivity increases linearly with y for all cases. However, θ_P's contribution deviates slightly from a linear relationship in several instances. In order to compute single performance numbers, an average sensitivity is calculated by averaging the sensitivity for five points across the swath including the inside and outside edges of the swath. The reason that this is valid is that it can be assumed that the terrain points are uniformly distributed across the swath. Thus, errors are weighted equally throughout the swath width. The resulting average sensitivities are summarized in Table VI.

As previously noted, the sensitivities determined can be used to compute the standard deviations of the image

Table VI Sensitivities of the Image Coordinates for the Improved Single Flight Technique

Error	X_1 Sens.	Y_1 Sens.	X_2 Sens.	Y_2 Sens.
ΔH_{A2}	0.00	0.00	0.00	0.94
ΔH_{A1}	0.30	0.83	0.00	0.00
ΔR_2	0.00	0.00	0.25	1.34
ΔR_1	0.09	0.25	0.00	0.00
ΔY_{A2}	0.00	0.00	0.00	-1.00
ΔY_{A1}	0.00	-1.00	0.00	0.00
ΔY_{I2}	0.00	0.00	0.00	1.00
ΔY_{I1}	0.00	1.00	0.00	0.00
ΔX_{I2}	0.00	0.00	1.00	0.00
ΔX_{I1}	1.00	0.00	0.00	0.00
ΔX_{A2}	0.00	0.00	-1.00	0.00
ΔX_{A1}	-1.00	0.00	0.00	0.00
θ_{R1}	-84.12	30.62	0.00	0.00
θ_{P2}	0.00	0.00	-261.78	92.74
θ_{P1}	-231.80	84.18	0.00	0.00
θ_{Y2}	0.00	0.00	294.55	-101.77
θ_{Y1}	294.55	-107.15	0.00	0.00
$\Delta\phi_2$	0.00	0.00	396.33	-137.57

Units: Distance Quantities - ft./ft.
Angles - ft./deg.

position errors when the standard deviations of each error are known. The standard deviations for the error quantities used for this analysis are chosen to conform with present day capabilities.[17] All angular errors are assumed to have short-term standard deviations of 0.01 degree which appears to be within the state-of-the-art for antenna stabilization. All aircraft position errors are assumed to have short-term standard deviations of one foot. This appears to be an attainable short-term navigation error for a high quality inertial navigation system. Ranging and imaging errors are assumed to have standard deviations of five feet. This corresponds to approximately 0.10 % accuracy with respect to one-half of the swath width. The average values of the image position error standard deviations are:

$$\sigma_{X1} = 6.40 \text{ ft.}$$
$$\sigma_{Y1} = 5.49 \text{ ft.}$$
$$\sigma_{X2} = 7.66 \text{ ft.}$$
$$\sigma_{Y2} = 8.68 \text{ ft.}$$

3. SELECTION OF OPTIMUM RECONSTRUCTION EQUATIONS

Before the effect of errors on the reconstructed terrain point orthographic position and height (x_r, y_r, h_r) can be determined, a set of reconstruction equations must be selected. Several possible equations to solve for these quantities were previously presented but no selection was made. To perform the selection, the effects of errors will be considered so a set of equations can be chosen which

minimizes errors. To accomplish this, partial derivatives are obtained and the standard deviations of the terrain point coordinate errors are determined using the image coordinate standard deviations given in the previous section.

To perform these calculations several approximations are made. Once the expression for a partial derivative is reached, the quantities Y_1 and Y_2 are replaced by y_r. This is because in all cases discussed here, y is constrained to 12,000 ft. < y < 22,000 ft. and a terrain point of reasonable height gives a deviation of Y_1 and Y_2 from y_r which can be considered negligible. Similarly, the expression $(H_A - h_r)^2$ can be replaced by H_A^2. It can be assumed in most cases that $X_1 = X_2$. In the cases for which y_r appears in the final partial derivative, it is necessary to choose an average value as was done in the previous section. This value is 16,900 ft. and corresponds to the center of the swath.

Consider first the solutions for x_r. The standard deviation for $x_r(X_2)$ can be written immediately since it is just that of X_2 and is

$$\sigma_{x_r} = 7.66 \text{ ft.}$$

The solution $x_r(X_1, Y_1, Y_2)$ for x_r requires the calculation of the partial derivatives

$$\frac{\partial x_r}{\partial X_1} = 1$$

$$\frac{\partial x_r}{\partial Y_1} = -\text{Cot } \theta_1 + Y_1 \text{Sec } \theta_1 / (Y_1^2 - Y_2^2 \text{Sin}^2 \theta_1)^{\frac{1}{2}}$$

$$\frac{\partial x_r}{\partial X_2} = 0$$

$$\frac{\partial x_r}{\partial Y_2} = -Y_2 \text{Sec } \theta_1 \text{Sin}^2 \theta_1 / (Y_1^2 - Y_2^2 \text{Sin}^2 \theta_1)^{\frac{1}{2}} .$$

Applying the approximations noted above gives

$$\frac{\partial x_r}{\partial X_1} = 1 \qquad \frac{\partial x_r}{\partial Y_1} \simeq 8.22 \qquad \frac{\partial x_r}{\partial X_2} = 0 \qquad \frac{\partial x_r}{\partial Y_2} \simeq -7.55 .$$

Using these partial derivatives as sensitivities and using the image position standard deviations computed in the last section, the approximate standard deviation of x_r is computed to be

$$\sigma_{x_r} = 80.5 \text{ ft.}$$

Comparison of the standard deviations for each solution shows that the solution $x_r(X_2)$ is obviously the best.

Consider secondly the solutions for y_r. The partial derivatives for the solution $y_r(Y_1, Y_2)$ for y_r are

$$\frac{\partial y_r}{\partial X_1} = 0$$

$$\frac{\partial y_r}{\partial Y_1} = Y_1 \text{Sec } \theta_1 / (Y_1^2 - Y_2^2 \text{Sin}^2 \theta_1)^{\frac{1}{2}} \simeq 8.55$$

$$\frac{\partial y_r}{\partial X_2} = 0$$

$$\frac{\partial y_r}{\partial Y_2} = -Y_2 \text{Sec } \theta_1 \text{Sin}^2 \theta_1 / (Y_1^2 - Y_2^2 \text{Sin}^2 \theta_1)^{\frac{1}{2}} \simeq -7.55 .$$

The resulting approximate standard deviation of y_r is

$$\sigma_{y_r} = 81.0 \text{ ft.}$$

The partial derivatives for the solution $y_r(X_1, X_2, Y_2)$ are

$$\frac{\partial y_r}{\partial X_1} = -\text{Sec } \theta_1 \text{Csc } \theta_1 + X_2 \text{Csc}^2 \theta_1 / \{(X_1 - X_2)^2 \text{Csc}^2 \theta_1 + Y_2^2\}^{\frac{1}{2}} \simeq -3.11$$

$$\frac{\partial y_r}{\partial Y_1} = 0$$

$$\frac{\partial y_r}{\partial X_2} = \text{Sec } \theta_1 \text{Csc } \theta_1 - X_2 \text{Csc}^2 \theta_1 / \{(X_1 - X_2)^2 \text{Csc}^2 \theta_1 + Y_2^2\}^{\frac{1}{2}} \simeq 3.11$$

$$\frac{\partial y_r}{\partial Y_2} = Y_2 / \{(X_1 - X_2)^2 \text{Csc}^2 \theta_1 + Y_2^2\}^{\frac{1}{2}} \simeq 1.0 \text{ .}$$

The resulting standard deviation for y_r is

$$\sigma_{y_r} = 32.2 \text{ ft.}$$

The partial derivatives for the solution $y_r(X_1, X_2, Y_1)$ are

$$\frac{\partial y_r}{\partial X_1} = -\text{Tan } \theta_1 = -2.75$$

$$\frac{\partial y_r}{\partial Y_1} = 1$$

$$\frac{\partial y_r}{\partial X_2} = \text{Tan } \theta_1 = 2.75$$

$$\frac{\partial y_r}{\partial Y_2} = 0 \text{ .}$$

As before, the partial derivatives may be used as the

sensitivities and the image coordinate standard deviations used to approximate the standard deviation of y_r which for this solution is computed to be

$$\sigma_{y_r} = 28.0 \text{ ft.}$$

Comparison of the standard deviations for each solution shows that the solution $y_r(X_1, X_2, Y_1)$ is the best choice.

Finally, consider the calculation of h_r. The partial derivatives for the solution $h_r(Y_1, Y_2)$ are

$$\frac{\partial h_r}{\partial X_1} = 0$$

$$\frac{\partial h_r}{\partial Y_1} = Y_1 \text{Sec}^2 \theta_1 / H_A \simeq 9.63$$

$$\frac{\partial h_r}{\partial X_2} = 0$$

$$\frac{\partial h_r}{\partial Y_2} = -Y_2 \text{Sec}^2 \theta_1 / H_A \simeq -9.63 \ .$$

The resulting approximate standard deviation for h_r is

$$\sigma_{h_r} = 98.8 \text{ ft.}$$

To consider the last two solutions for h_r, the problem of y_r appearing in these solutions has to be overcome. To do this, the partial derivative of h_r with respect to y_r is calculated and the standard deviation previously determined for y_r for each specific solution is used in the same manner as the standard deviations of the image positions. The

partial derivatives for the solution $h_r(X_1, X_2, Y_2)$ are

$$\frac{\partial h_r}{\partial X_1} = 0$$

$$\frac{\partial h_r}{\partial Y_1} = 0$$

$$\frac{\partial h_r}{\partial X_2} = 0$$

$$\frac{\partial h_r}{\partial Y_2} = -Y_2/(H_A^2 - y_r^2 + Y_2^2)^{\frac{1}{2}} \simeq -1.13$$

$$\frac{\partial h_r}{\partial Y_r} = y_r/(H_A^2 - y_r^2 + Y_2^2)^{\frac{1}{2}} \simeq 1.13 \ .$$

The resulting approximate standard deviation for h_r is

$$\sigma_{h_r} = 37.7 \text{ ft.}$$

The partial derivatives for the solution $h_r(X_1, X_2, Y_1)$ are

$$\frac{\partial h_r}{\partial X_1} = 0$$

$$\frac{\partial h_r}{\partial Y_1} = -Y_1 \text{Csc}^2\ \theta_1/\{H_A^2 - (y_r^2 - Y_1^2)\text{Csc}^2\ \theta_1\}^{\frac{1}{2}} \simeq -1.28$$

$$\frac{\partial h_r}{\partial X_2} = 0$$

$$\frac{\partial h_r}{\partial Y_2} = 0$$

$$\frac{\partial h_r}{\partial Y_r} = y_r \text{Csc}^2\ \theta_1/\{H_A^2 - (y_r^2 - Y_1^2)\text{Csc}^2\ \theta_1\}^{\frac{1}{2}} \simeq 1.28 \ .$$

The resulting approximate standard deviation for h_r is

$$\sigma_{h_r} = 36.5 \text{ ft.}$$

The solutions $h_r(X_1, X_2, Y_2)$ and $h_r(X_1, X_2, Y_1)$ for h_r yield about the same result. Because of the many approximations involved, it is not reasonable to choose one of the solutions over the other. However, analysis of the two solutions shows that if y_r associated with the solution $h_r(X_1, X_2, Y_1)$ is substituted into the solution $h_r(X_1, X_2, Y_2)$ a new solution results which is superior to either method. This appears to be the only case where a combination of results achieve a better answer. The resulting standard deviation for the combined solution is

$$\sigma_{h_r} = 33.1 \text{ ft.}$$

In summary, the resulting optimum reconstruction equations are

$$x_r = X_2 \tag{106}$$

$$y_r = Y_1 + (X_2 - X_1)\text{Tan } \theta_1 \tag{107}$$

$$h_r = H_A - (H_A^2 - y_r^2 + Y_2^2)^{\frac{1}{2}} . \tag{108}$$

No physical interpretation has been given yet for the solutions. It can be shown that a graphical solution using the radar data coordinates will yield the optimum solution arrived at above for x_r and y_r. If these solutions are used to calculate the conical beam parallax, and h_r is obtained

in terms of this quantity, then the optimum solution for h_r will result. This is shown in Fig. 53 and described below.

The conical beam geometry is such that no along-track image displacement is introduced. This means that the reconstructed terrain point must lie somewhere on the line A as shown in Fig. 53. The fan beam introduces image displacement only in the direction parallel to the illumination plane. This means that the reconstructed terrain point must lie somewhere on the line B as shown in Fig. 53. These two conditions are sufficient to solve for x_r and y_r and give Eqns. 106 and 107 shown above. The conical beam image parallax, ΔR_{G2}, can be determined by

$$\Delta R_{G2} = Y_2 - y_r. \tag{109}$$

Substituting this equation into Eqn. 22 derived in the section covering reconstruction equations and solving for h_r results in Eqn. 108 above. Thus, the optimum solution obtained and the graphical solution are identical.

4. RECONSTRUCTED STEREO MODEL ERRORS

The optimum reconstruction equations determined in the previous section are used to convert the measured image coordinates X_1, Y_1, X_2, and Y_2 to the reconstructed terrain point coordinates x_r, y_r, and h_r. The errors in this final reconstructed stereo model position could be obtained by using the standard deviations of the image position errors which were previously established and the sensitivities computed in the last section. However, the computer simulation used to obtain

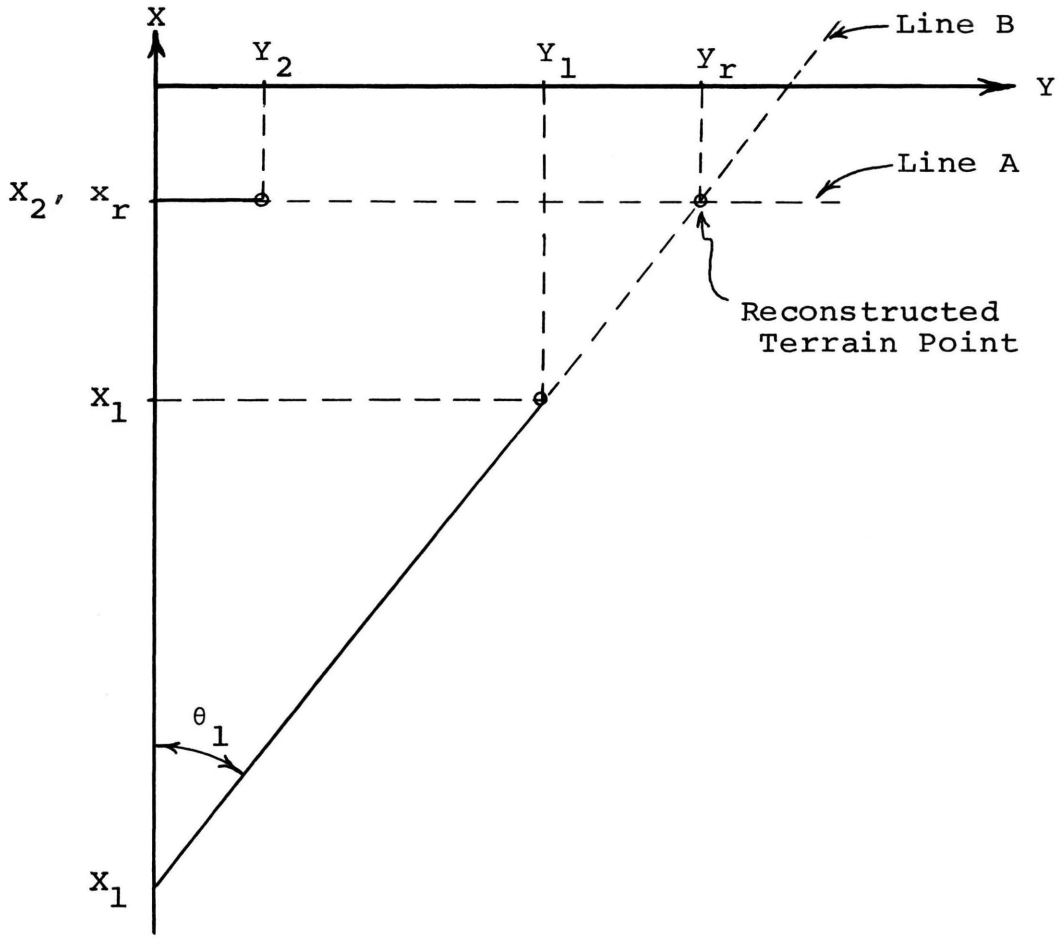

Fig. 53 Graphical Interpretation of the Optimum Reconstruction Equations

image position sensitivities is easily modified to compute the stereo model position errors without the approximations required in the previous section. All that is necessary in addition to the existing simulation program is calculation of the reconstructed terrain point position with error using the equations obtained in the previous section, comparison of each individual terrain point coordinate value with the corresponding value without error, and calculation of the sensitivity of the reconstructed terrain point to the error used. Let x, y, and h define the original terrain point position and x_r, y_r, and h_r define the reconstructed terrain point position with error present. Then the final data from the program are the expressions

$$\frac{\partial x_r}{\partial E} \simeq (x_r - x)/\Delta E \tag{110}$$

$$\frac{\partial y_r}{\partial E} \simeq (y_r - y)/\Delta E \tag{111}$$

$$\frac{\partial h_r}{\partial E} \simeq (h_r - h)/\Delta E \tag{112}$$

where ΔE denotes a single instantaneous error as defined earlier. Also, it is necessary to differentiate between whether the error occurs during fan beam or conical beam illumination. This is done by adding a subscript 1 or 2 to the error identifiers as before. A flow chart describing the modified simulation program is shown in Fig. 54. Additional discussion of the program is given in the Appendix.

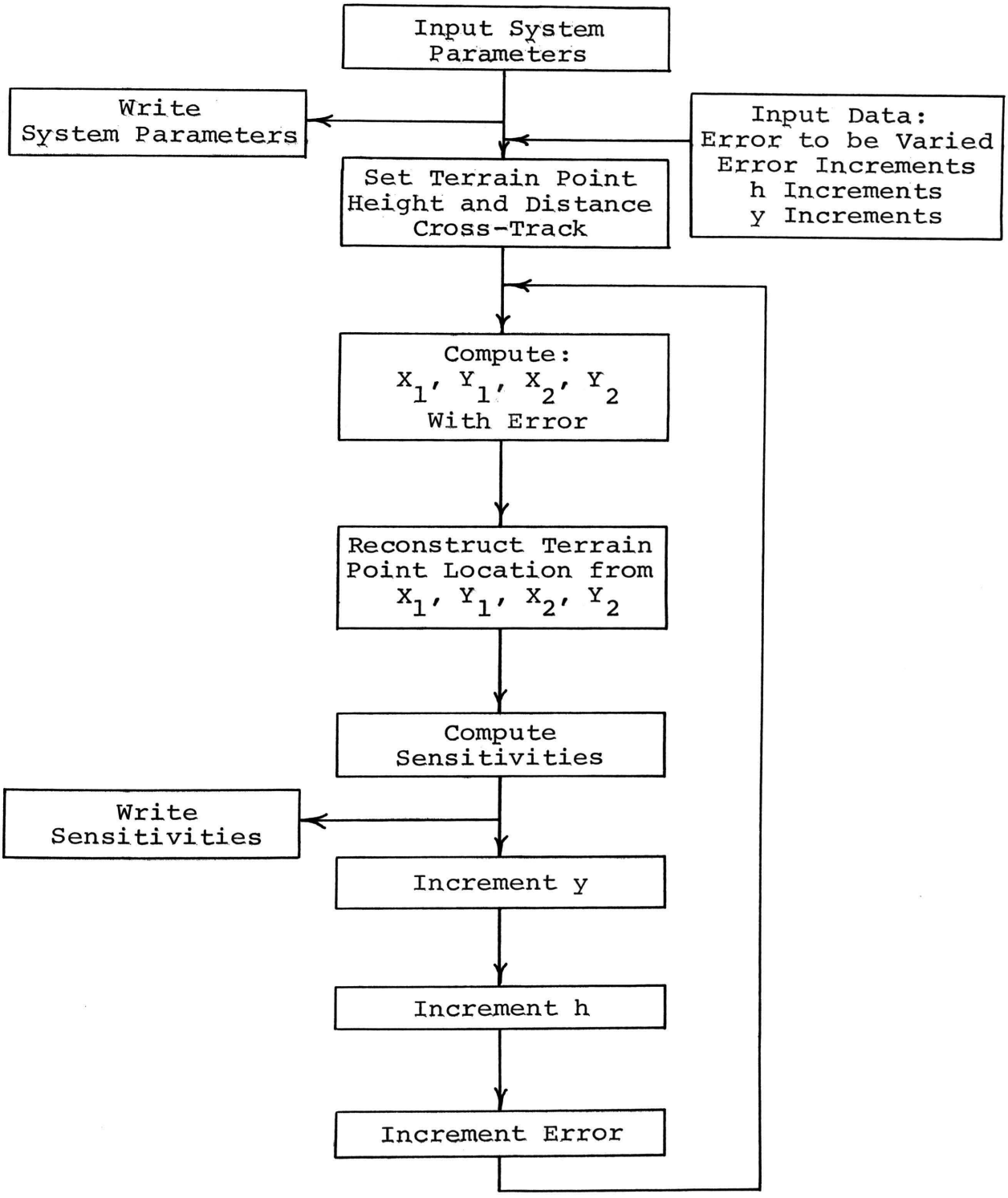

Fig. 54 Flow Chart Describing Computer Program Used to Obtain Error Sensitivities of Terrain Point Coordinates

The results of the simulation are presented in Figs. 55, 56, and 57. This data was obtained using the system parameters corresponding to the optimum system presented earlier and given in Table III. Note that the plots present the quantities $\alpha \cdot \sigma$ where α refers to the sensitivity to an individual error and σ is the standard deviation assigned to the error. The purpose for presenting the data in this manner is to provide an indication of the relative effect upon system performance of each error for the error values assumed. Again, all angular errors are assigned standard deviations of 0.01 degree, aircraft position errors are assigned standard deviations of one foot, and ranging and imaging errors are assigned standard deviations of five feet.

The error quantities in Figs. 55, 56, and 57 are plotted as a function of cross-track distance. The reason for this is that the variation of all errors with terrain point height is negligible. Initial analysis of the plots tends to show that the rank of overall sensitivity to error is x_r, y_r, and h_r. That is, x_r is quite insensitive to error, while y_r is fairly sensitive to error, and h_r is very sensitive to error. From the plots it can be concluded that the effect of aircraft position errors on x_r, y_r, and h_r is much smaller than the effect of the other errors. Most of the error results from the angular errors, particularly the conical beam phasing error, and the imaging errors.

The average sensitivities are calculated, again by averaging five points equidistant across the swath, and are

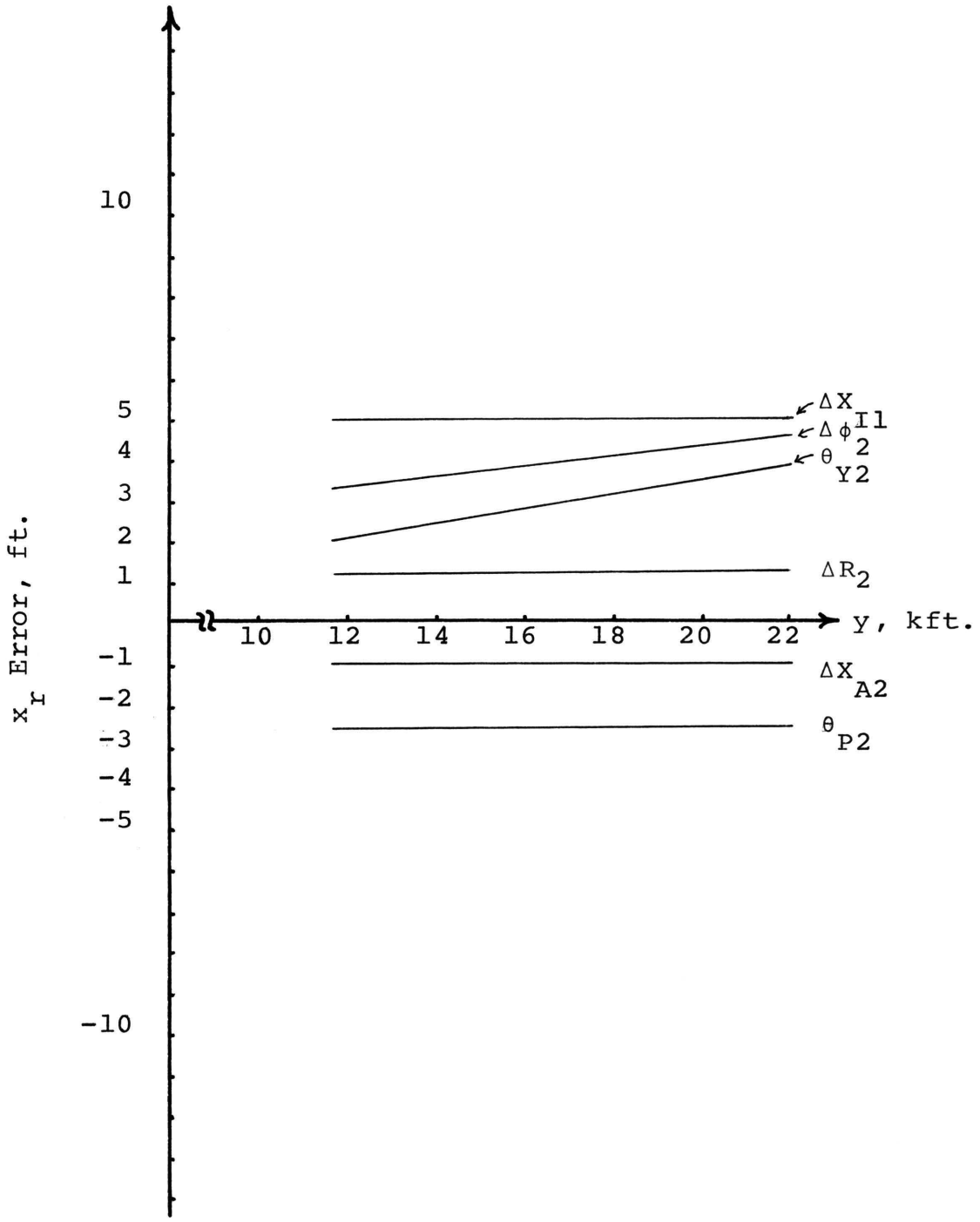

Fig. 55 Error of Reconstructed Terrain Point Along-Track Position x_r for the Improved Single Flight Technique

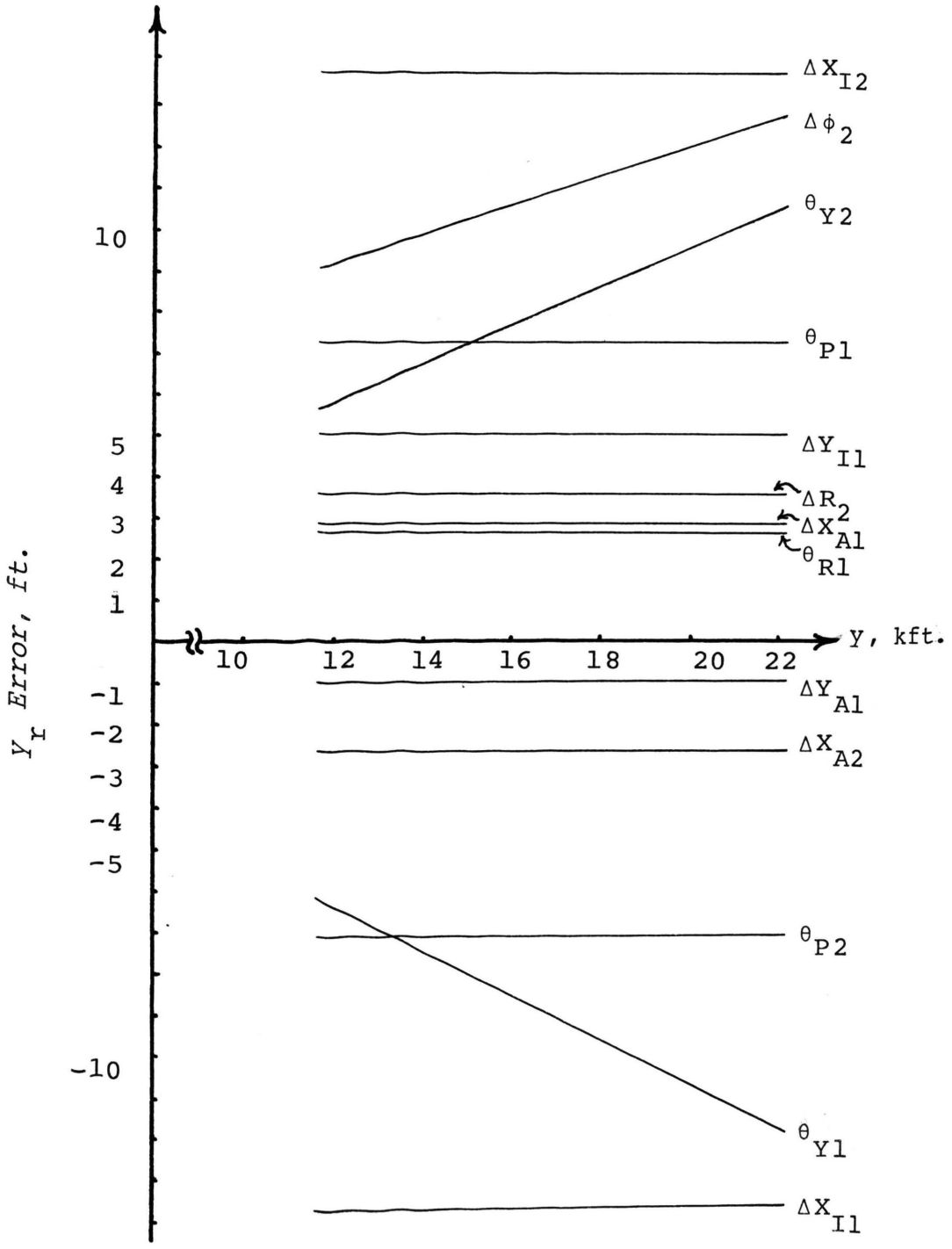

Fig. 56 Error of Reconstructed Terrain Point Cross-Track Position y_r for the Improved Single Flight Technique

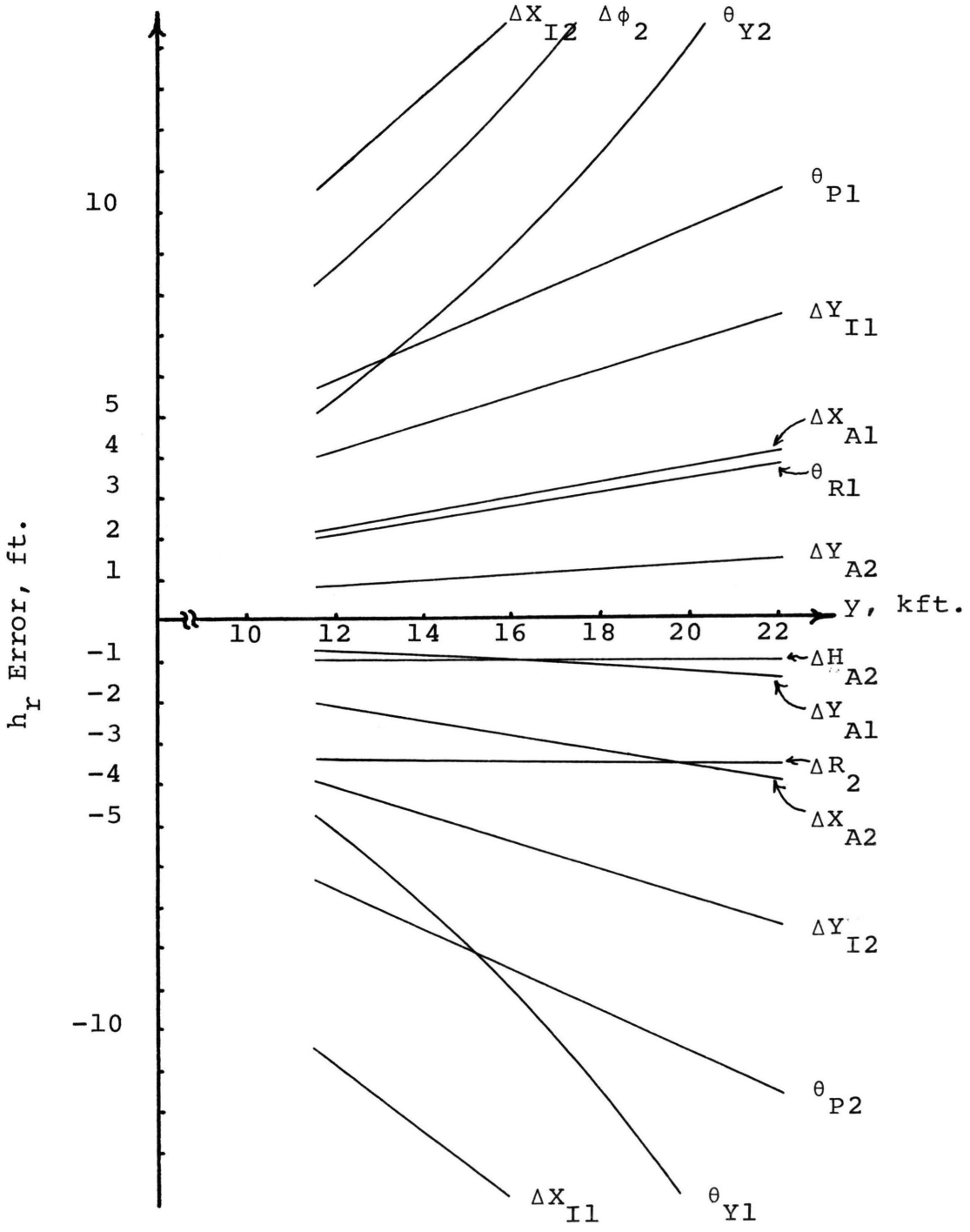

Fig. 57 Error of Reconstructed Terrain Point Height h_r for the Improved Single Flight Technique

listed in Table VII. The final overall system error standard deviations can be determined from the sensitivities shown in Table VII. Using the same error magnitudes as before, the error standard deviations for the reconstructed terrain point position are:

$$\sigma_{x_r} = 7.7 \text{ ft.}$$
$$\sigma_{y_r} = 28.4 \text{ ft.}$$
$$\sigma_{h_r} = 34.2 \text{ ft.}$$

The errors shown are short-term errors which means that the aircraft altitude and position errors are different for the two illuminations. Note that long-term aircraft altitude and position errors are constant errors for the two illuminations and (with the exception of the roll angle) will only significantly affect the along-track position since the other sensitivities nearly cancel. The height measuring error of 34.2 ft. compares favorably with the theoretical value of 50 ft. given in Sec. V, A. Also, the along-track and cross-track coordinate errors are quite reasonable for radar mapping of this sort. These facts indicate that the error magnitudes chosen are approximately the stabilization and position accuracies required for the system. However, if a system employing this technique is developed, the primary concern should be angular stabilization because this is the primary source of the errors and the aircraft position sensors' specifications can be relaxed to some extent without much degradation in system performance. In summary,

Table VII Sensitivities of the Reconstructed Terrain Point Coordinates for the Improved Single Flight Technique

Error	x_r Sens.	y_r Sens.	h_r Sens.
ΔH_{A2}	0.00	0.00	-1.00
ΔH_{A1}	0.00	0.00	0.00
ΔR_2	0.25	0.68	-0.70
ΔR_1	0.00	0.00	0.00
ΔY_{A2}	0.00	0.00	1.13
ΔY_{A1}	0.00	-1.00	-1.13
ΔY_{I2}	0.00	0.00	-1.13
ΔY_{I1}	0.00	1.00	1.13
ΔX_{I2}	1.00	2.75	3.10
ΔX_{I1}	0.00	-2.75	-3.10
ΔX_{A2}	-1.00	-2.75	-3.10
ΔX_{A1}	0.00	2.75	3.10
θ_{R1}	0.00	261.75	294.60
θ_{P2}	-261.78	-719.24	-910.23
θ_{P1}	0.00	719.34	810.19
θ_{Y2}	294.55	809.27	1073.85
θ_{Y1}	0.00	-916.42	-1079.85
$\Delta\phi_2$	396.33	1088.92	1436.50

Units: Distance Quantities - ft./ft.
Angles - ft./deg.

this technique is feasible and can be implemented using present day state-of-the-art sensing and stabilization equipment.

D. PREVIOUSLY PROPOSED SINGLE FLIGHT TECHNIQUE

In this section the error analysis for the previously proposed single flight technique is considered. The techniques and equations developed in the previous section for the improved single flight technique can also be applied to the previous single flight technique and are used here. The system parameters to be used for this analysis are described in Sec. V, A and shown in Table IV.

The forward beam geometry is identical to that of the fan beam used by the improved single flight technique and so the error equations developed in Sec. V, C can also be used here. Thus the expressions for the forward beam illumination including the effect of all errors are given by Eqns. 80, 81, 82, 84, 85, and 86.

The rear beam considered for this analysis is chosen to be a side-looking fan beam. As shown previously in Sec. IV,A where the reconstruction equations for the previous single flight technique were developed, the rear beam image has exactly the same geometry as the conical beam illumination for the improved single flight technique (with $\theta_2 = 90^\circ$). This is because the conical beam functions much like a side-looking beam except that the illumination occurs when the aircraft is in a different position. However, the error

equations for the fan beam illumination of the improved single flight technique must be used because the rear beam is a vertical fan beam with an azimuth angle of 90°.

Due to the similarity in the characteristics and geometry of the single flight techniques, it is assumed for the purpose of this analysis that the optimum reconstruction equations determined in the previous section for the improved single flight technique also give optimum results for the previous single flight technique. Thus Eqns. 106, 107, and 108 are used for reconstructing the terrain model from the image coordinates for the previous single flight technique. The computer simulation developed for determining the error sensitivities of the reconstructed terrain point coordinates for the improved single flight technique can also be used here with only slight modifications. The modifications are given and described in the Appendix.

The results of the error analysis for the previous single flight technique are presented in Figs. 58, 59, and 60. These data were obtained using the system parameters given earlier. The plots again present the quantities $\alpha \cdot \sigma$, where α is the sensitivity and σ is the standard deviation of the error. As noted previously, the purpose for presenting the data in this manner is to provide an indication of the relative effect of each error on system performance for the error values assumed. Again, angular errors are assigned standard deviations of 0.01 deg., aircraft position errors are assigned standard deviations of one foot, and ranging

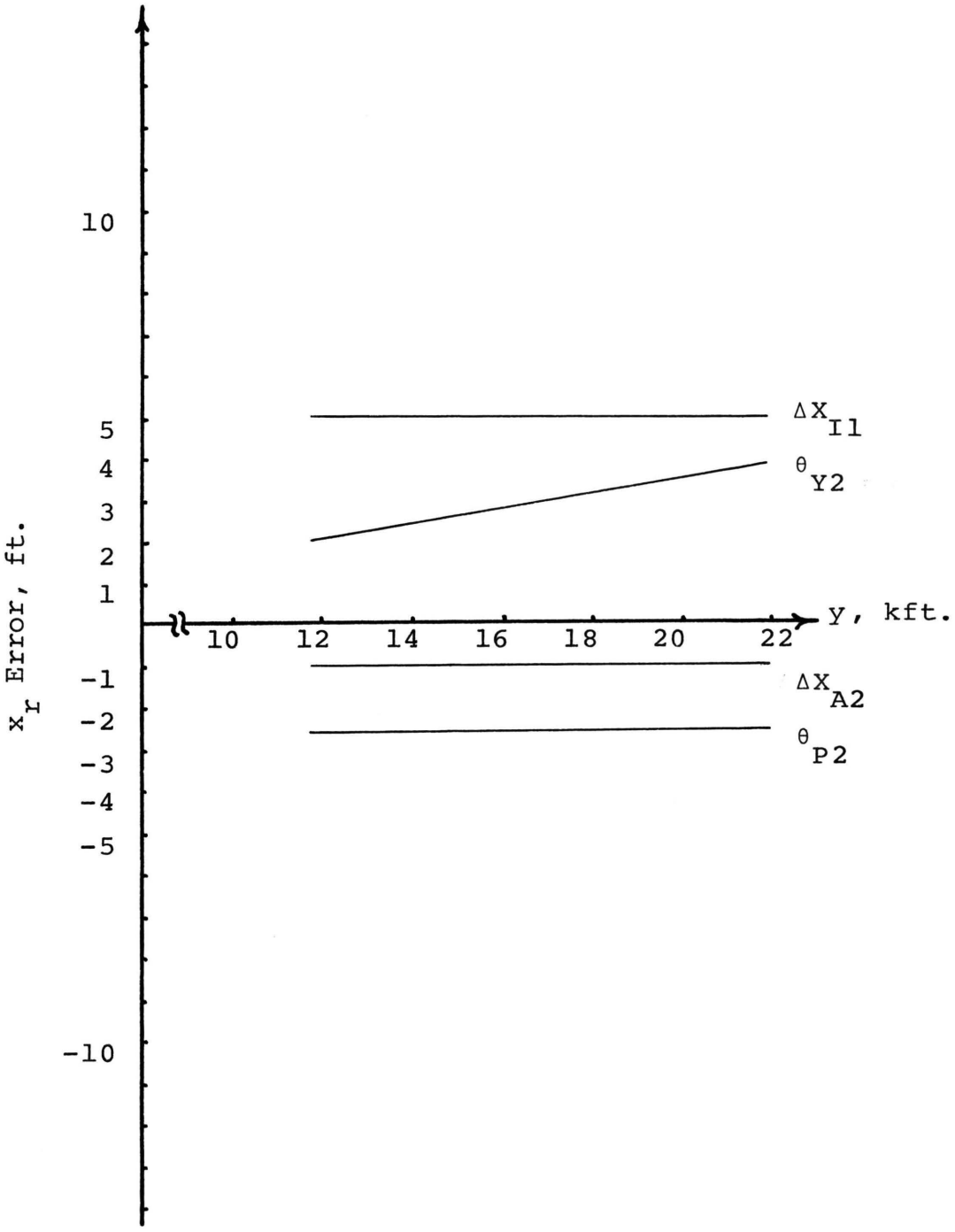

Fig. 58 Error of Reconstructed Terrain Point Along-Track Position, x_r, for the Previous Single Flight Technique

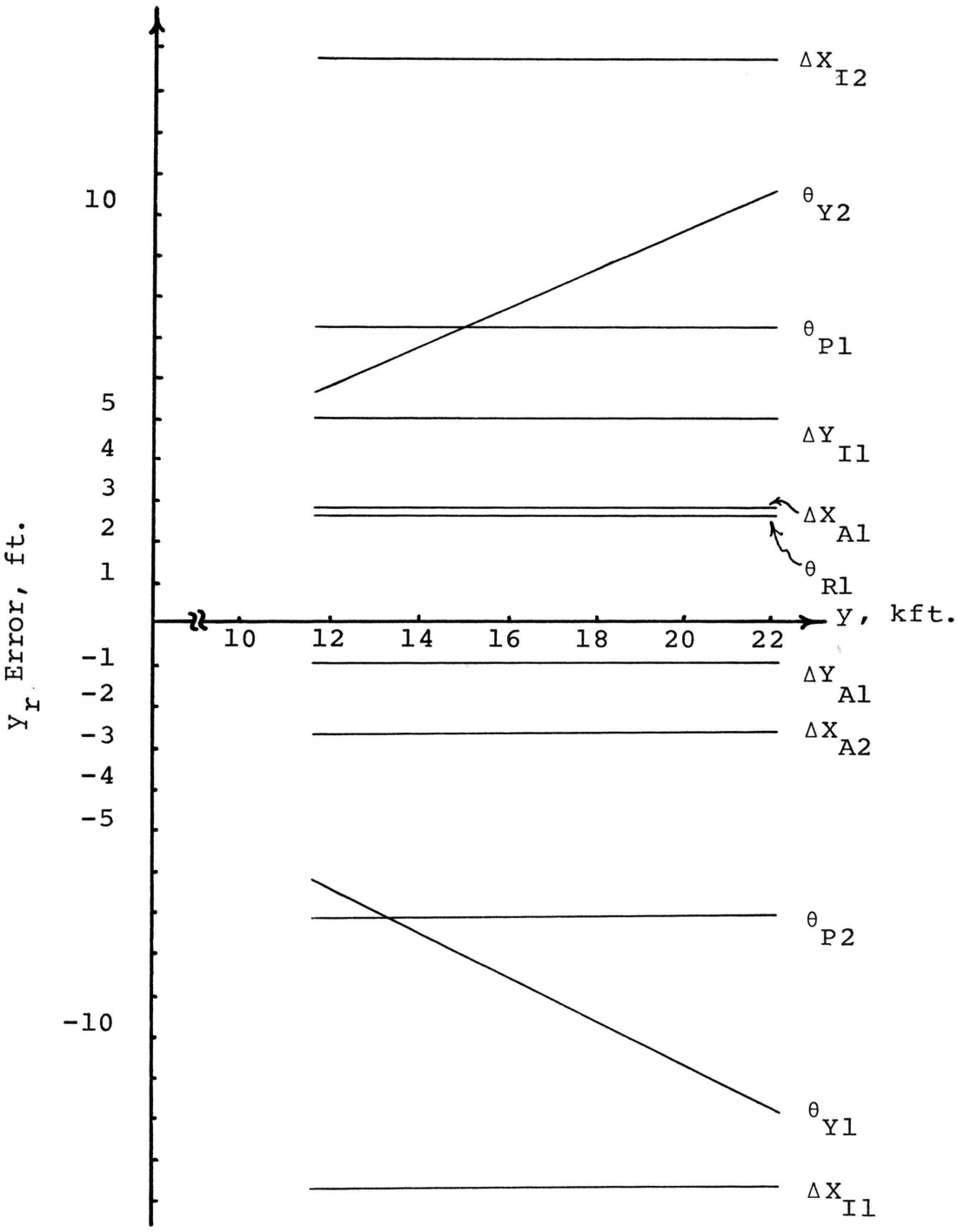

Fig. 59 Error of Reconstructed Terrain Point Cross-Track Position y_r for the Previous Single Flight Technique

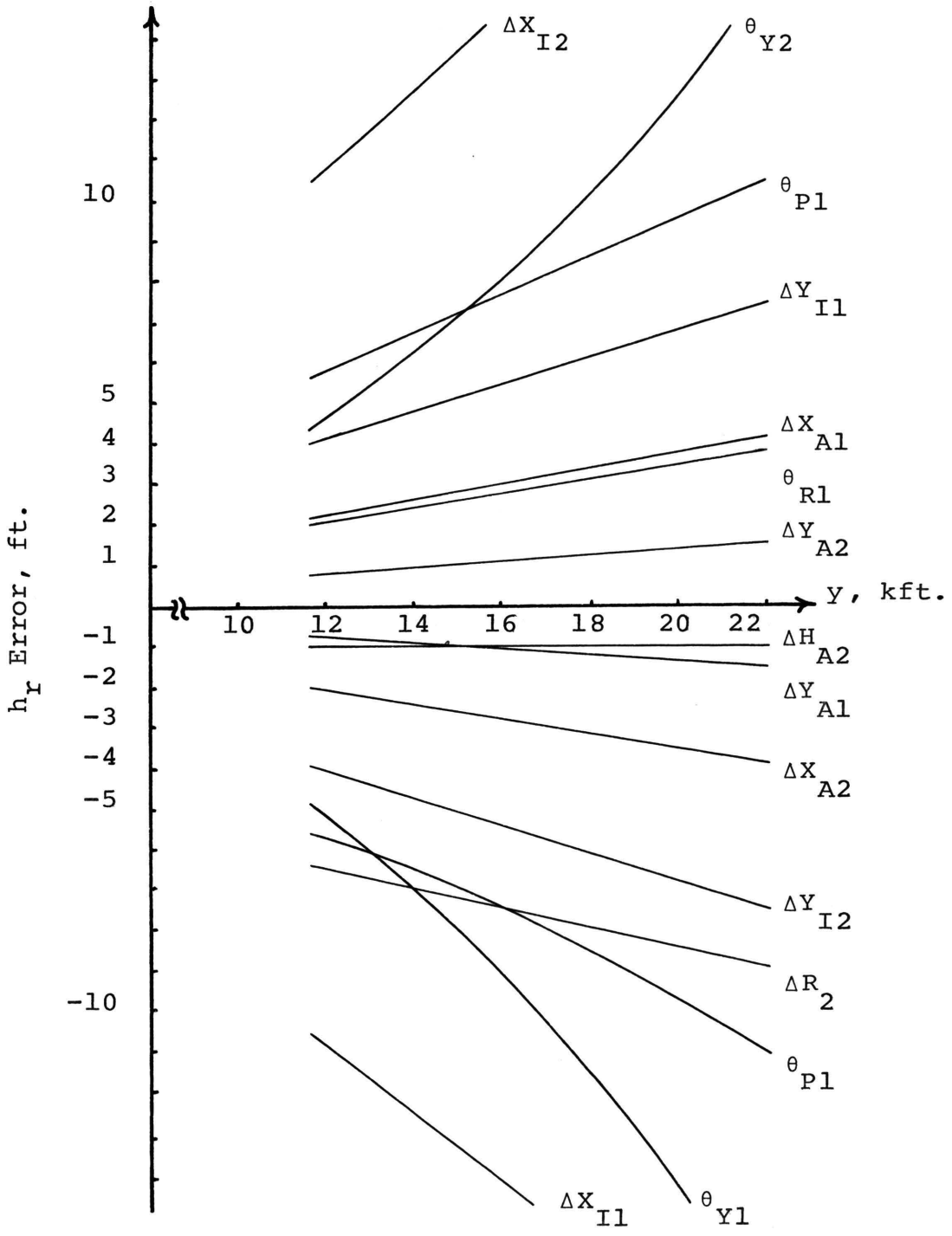

Fig. 60 Error of Reconstructed Terrain Point Height h_r for the Previous Single Flight Technique

and imaging errors are assigned standard deviations of five feet. The error quantities have been plotted as a function of cross-track distance. The reason for this, as for the improved single flight technique, is that the variation of all errors with terrain point height is negligible.

The plots of the errors in the reconstructed terrain point coordinates for the previous single flight technique are very similar to those of the improved single flight technique and so most of the previous remarks concerning the error quantities are also applicable here. Specifically, the plots show that the reconstructed terrain point coordinates are most sensitive to aircraft angular errors and data imaging errors. Also, the effect of aircraft position errors is small. Again, the plots show that the rank of the overall sensitivity to error is x_r, y_r, and h_r.

The average value for each sensitivity for the previous single flight technique can now be determined, again by averaging sensitivity values for five equidistant points across the swath. The results are given in Table VIII. Note that these values are almost exactly the same as those given in Table VII for the improved single flight technique. Using the same error magnitudes as before, the error standard deviations for the reconstructed terrain coordinates are:

$$\sigma_{x_r} = 6.4 \text{ ft.}$$
$$\sigma_{y_r} = 26.0 \text{ ft.}$$
$$\sigma_{h_r} = 31.2 \text{ ft.}$$

Table VIII Sensitivities of Reconstructed Terrain Point Coordinates for the Previous Single Flight Technique

Error	x_r Sens.	y_r Sens.	h_r Sens.
ΔH_{A2}	0.00	0.00	-1.00
ΔH_{A1}	0.00	0.00	0.00
ΔR_2	0.00	0.00	-1.51
ΔR_1	0.00	0.00	0.00
ΔY_{A2}	0.00	0.00	1.13
ΔY_{A1}	0.00	-1.00	-1.13
ΔY_{I2}	0.00	0.00	-1.13
ΔY_{I1}	0.00	1.00	1.13
ΔX_{I2}	1.00	2.75	3.10
ΔX_{I1}	0.00	-2.75	-3.10
ΔX_{A2}	-1.00	-2.75	-3.10
ΔX_{A1}	0.00	2.75	3.10
θ_{R1}	0.00	261.75	294.61
θ_{P2}	-261.80	-719.29	-808.57
θ_{P1}	0.00	719.34	810.19
θ_{Y2}	294.57	809.32	956.10
θ_{Y1}	0.00	-916.42	-1079.85

Units: Distance Quantities - ft./ft.
Angles - ft./deg.

The height measuring error compares favorably with the theoretical value of 50 feet. Also, the along-track and cross-track coordinate errors are quite reasonable for radar mapping of this sort. Thus the previous single flight technique is capable of providing reasonable performance with the stabilization and position accuracies assumed. In summary, the previous single flight technique is feasible and can be implemented using present day state-of-the-art sensing and stabilization equipment.

E. EXISTING TWO FLIGHT TECHNIQUE

The error analysis for the existing two flight technique is shown in this section. The reconstructed terrain point coordinate sensitivities and errors are computed in the same manner as previously for the single flight techniques.

As discussed earlier, the two flight technique uses a single side-looking beam and the radar images are obtained by making two flights past the terrain at different terrain offsets. The fan beam error equations for the improved single flight technique (Eqns. 80, 81, 82, 84, 85, and 86) can be used for each of the illuminations with only minor modifications. Specifically, $\theta_1 = \theta_2 = 90^\circ$ for both illuminations, the terrain point cross-track distance y' for the far pass illumination is changed by adding the offset distance Y_0 (defined in Fig. 22) when computing the image coordinates resulting from the far pass illumination, and

the cross-track image coordinate Y_2 is altered by subtracting the terrain offset.

The reconstruction equations for the two flight technique are given in Table II. Since there is only a single solution for terrain point cross-track position and height, y_r and h_r, it is not necessary to determine the image coordinate sensitivities in order to obtain the optimum equations. Also, since both the illuminations have the same geometry and result in two along-track position equations having the same form (see Table II), it is assumed for the purpose of this analysis that the average of the two solutions for the along-track reconstructed position x_r, as shown below, is the optimum solution:

$$x_r = \tfrac{1}{2}(X_1 + X_2) \quad . \tag{113}$$

Thus none of the image coordinate sensitivities or the partial derivatives of the reconstruction equations need to be determined.

The computer simulation used for determining the sensitivities of the terrain point coordinates for the single flight techniques can be used here with slight changes to compensate for the difference in imaging geometry. The modifications are described in the Appendix. The results of the error analysis are shown in Figs. 61, 62, and 63. These data were obtained using the system parameters shown earlier and, as before, the quantities $\alpha \cdot \sigma$ are presented so that an indication of the relative effect of each error on system

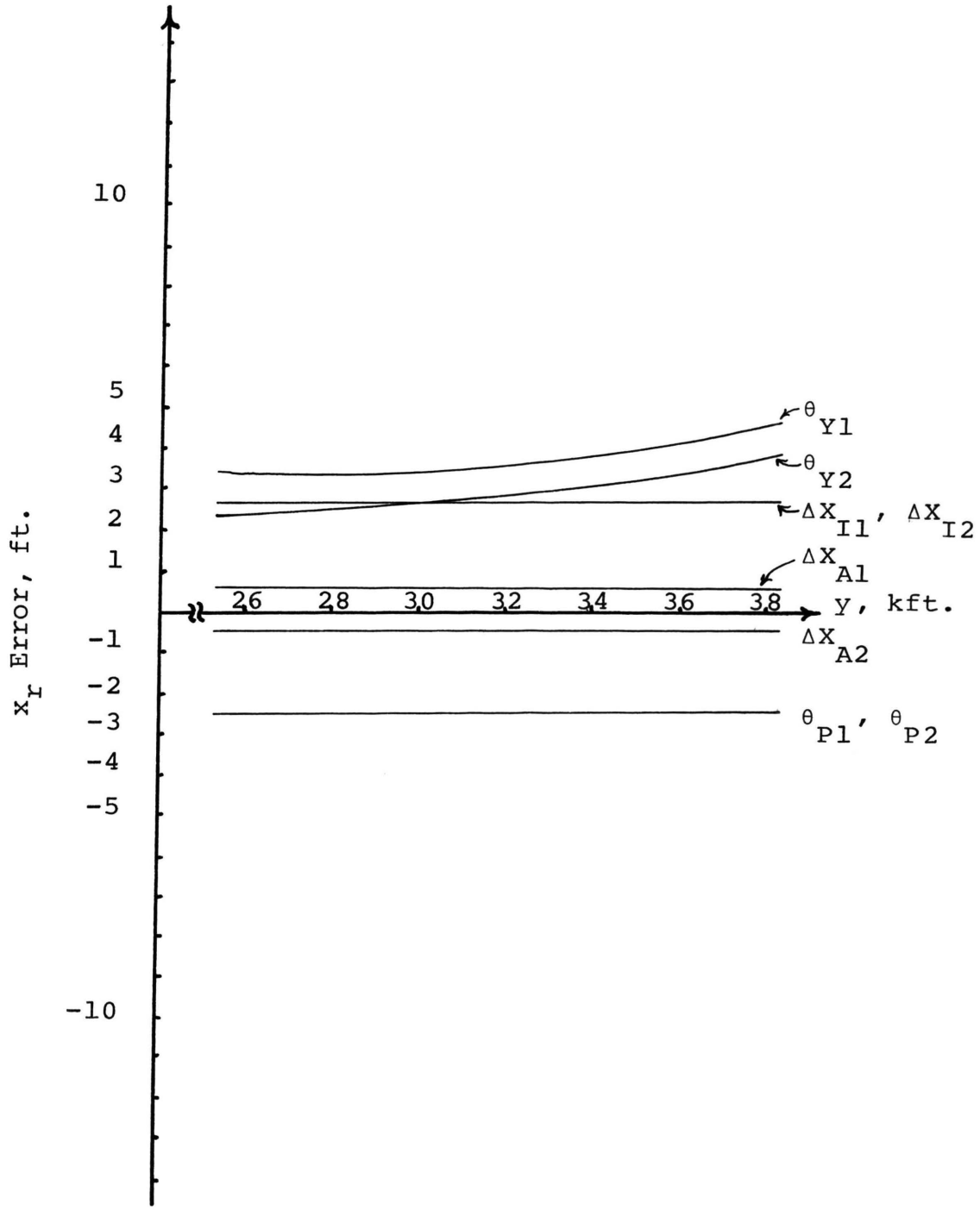

Fig. 61 Error of Reconstructed Terrain Point Along-Track Position x_r for the Two Flight Technique

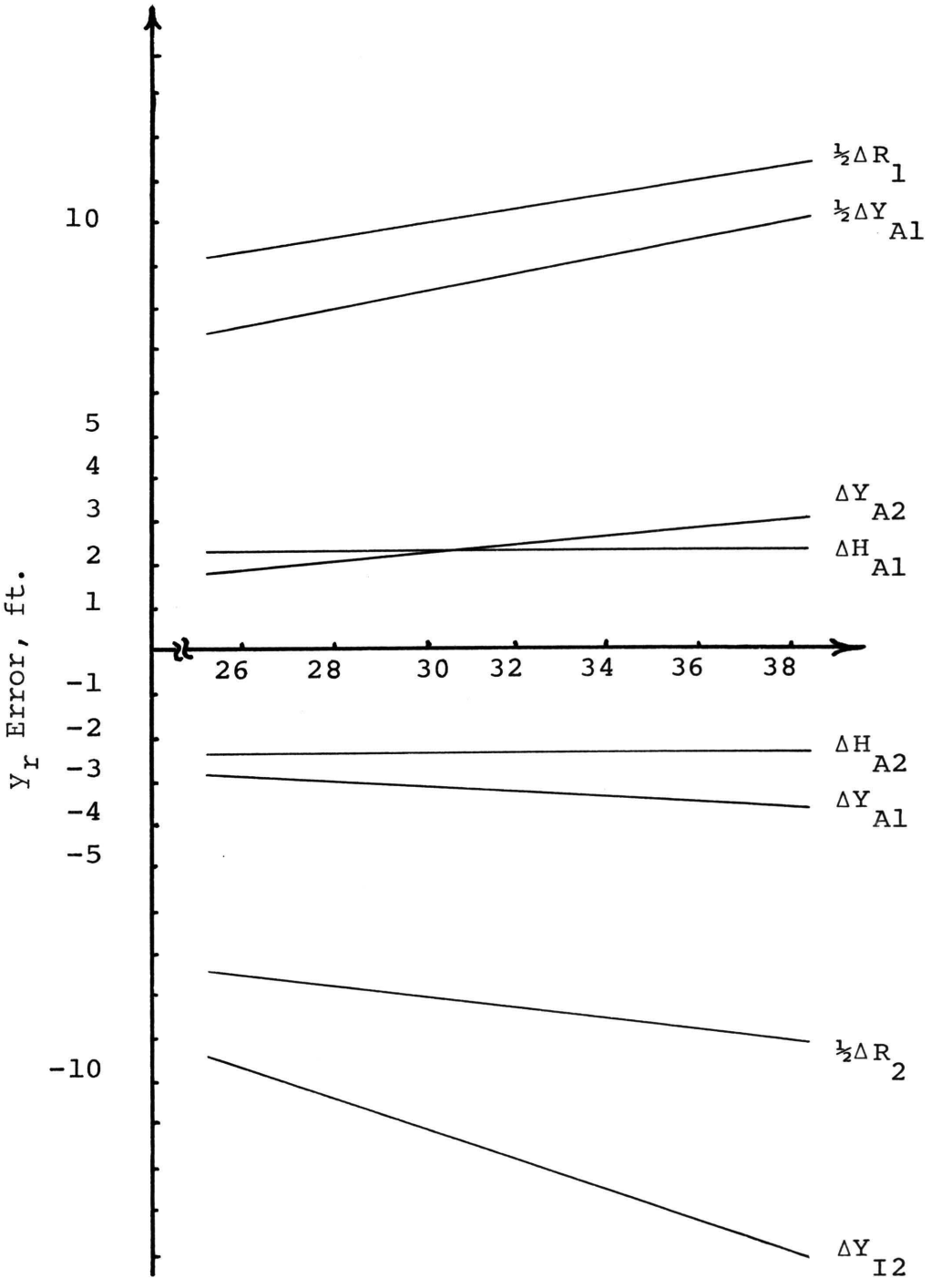

Fig. 62 Error of Reconstructed Terrain Point Cross-Track Position y_r for the Two Flight Technique

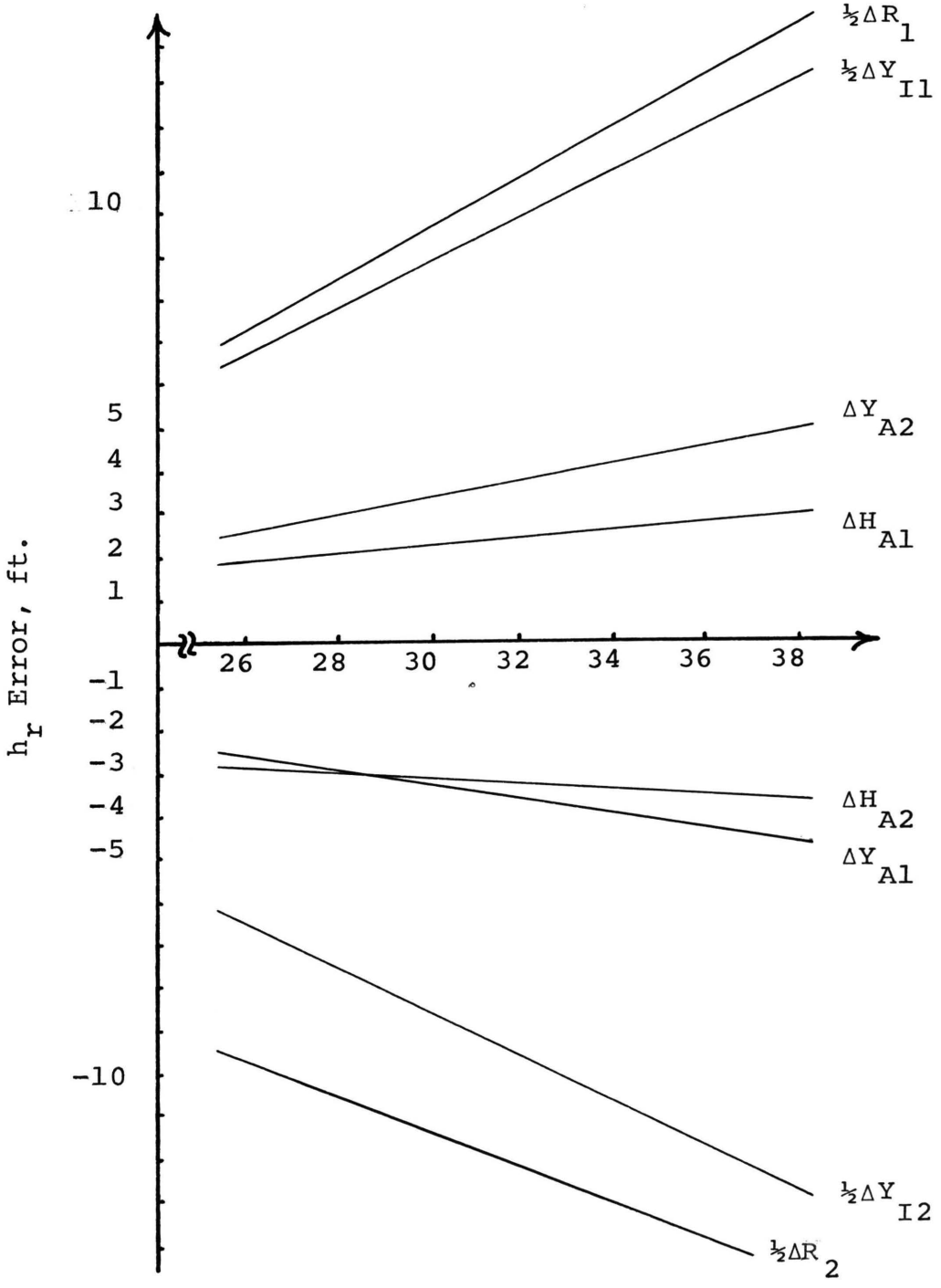

Fig. 63 Error of Reconstructed Terrain Point Height h_r for the Two Flight Technique

performance is apparent. In some instances the quantity $\frac{1}{2}\alpha \cdot \sigma$ is plotted so that the same scale used previously can be used. The previously assumed error standard deviations are used. Again, the error quantities are plotted as a function of cross-track distance because the variation with terrain height is negligible.

The plots show that y_r and h_r are most sensitive to aircraft position and ranging errors. The effect of aircraft angular errors is negligible for y_r and h_r and the errors are not plotted. Also, x_r is most sensitive to angular and imaging errors. It is not affected by aircraft altitude, cross-track position, and cross-track imaging errors. Again, the rank of overall error sensitivity is x_r, y_r, and h_r.

As before, points across the swath are averaged to obtain average sensitivities. The results are shown in Table IX. The sensitivities of y_r and h_r appear small. However, it is important to note that the sensitivities are given in units ft./deg. and ft./ft. and the standard deviations for the angular errors are two orders of magnitude smaller than distance errors.

Using the same error magnitudes as before, the error standard deviations for the reconstructed terrain position are

$$\sigma_{x_r} = 7.1 \text{ ft.}$$
$$\sigma_{y_r} = 34.0 \text{ ft.}$$
$$\sigma_{h_r} = 42.7 \text{ ft.}$$

Table IX Sensitivities of the Reconstructed Terrain Point Coordinates for the Two Flight Technique

Error	x_r Sens.	y_r Sens.	h_r Sens.
ΔH_{A2}	0.00	-2.27	-3.40
ΔH_{A1}	0.00	2.27	2.41
ΔR_2	0.00	-3.32	-5.01
ΔR_1	0.00	4.10	4.39
ΔY_{A2}	0.00	2.41	3.67
ΔY_{A1}	0.00	-3.41	-3.67
ΔY_{I2}	0.00	-2.41	-3.67
ΔY_{I1}	0.00	3.41	3.67
ΔX_{I2}	0.50	0.00	0.00
ΔX_{I1}	0.50	0.00	0.00
ΔX_{A2}	-0.50	0.00	0.00
ΔX_{A1}	-0.50	0.00	0.00
θ_{P2}	-261.80	-0.21	-0.26
θ_{P1}	-261.80	0.21	0.22
θ_{Y2}	277.27	-0.24	-0.37
θ_{Y1}	392.46	0.47	0.52

Units: Distance Quantities - ft./ft.
Angles - ft./deg.

VI. COMPARISON OF THE PERFORMANCE OF THE THREE STEREO RADAR TECHNIQUES

In the previous section the sensitivities and standard deviations of the reconstructed terrain point coordinates for each of the three stereo radar techniques were determined. In this section these quantities are used to compare the capabilities of the three techniques.

The terrain point coordinate errors for the improved single flight technique are shown in Figs. 55, 56, and 57, and the terrain point coordinate errors for the previous single flight technique are shown in Figs. 58, 59, and 60. Comparison of these plots shows that the errors of the two techniques are very similar. The primary difference is that the conical beam phase error $\Delta\phi_2$ is not present for the previous single flight technique. This is due to the way the systems are implemented with different antenna beam patterns. The slant ranging error ΔR_2 does not affect y_r for the previous single flight technique but does affect y_r for the improved single flight technique. This is because the rear beam geometry of the previous single flight technique is such that the slant range measurement from the rear beam illumination is not used to calculate y_r while the conical beam geometry of the improved single flight technique is such that the slant range measurement must be used. The only other major difference between the errors of the two techniques is that several of the error quantities for h_r of the previous single flight technique are slightly

less than those for the improved single flight technique. All of these differences are because the conical beam of the improved single flight technique produces images with the same geometry as the side-looking beam of the previous single flight technique, but the aircraft is at a position slightly farther away from the terrain at the time of illumination.

The sensitivities of the reconstructed terrain point coordinates for the improved single flight technique are given in Table VII and those for the previous single flight technique are given in Table VIII. Comparison of these quantities points out more clearly the slight differences between the two techniques.

The terrain point coordinate errors for the two flight technique are shown in Figs. 61, 62, and 63. The figures show that the errors for the two flight technique are markedly different from those for the single flight techniques. The errors for the along-track position are quite similar for the two flight technique and the single flight techniques. For all three techniques the main sources of error for x_r are the angular errors and the imaging. However, the main source of errors for y_r and h_r for the two flight technique are ranging, imaging, and aircraft position errors while the main source of errors for y_r and h_r for the single flight techniques are angular errors and imaging errors. Also, in general, angular errors are negligible for the two flight technique, while for the single flight

techniques aircraft position errors are negligible. The main reason for this vast difference in error sources is due to the way that the two flight technique relies only on cross-track ranges for terrain point position information while the single flight techniques must rely on terrain point position information obtained by a combination of ranges in both the along-track and cross-track directions.

The sensitivities of the reconstructed terrain point coordinates for the two flight technique are given in Table IX. Comparison of these quantities with those of the single flight techniques given in Tables VII and VIII shows even more distinctly the differences between the techniques.

The standard deviations of the reconstructed terrain point coordinates for the three stereo radar techniques are shown in Table X. These quantities show that the previous single flight technique gives slightly better performance than the improved single flight technique and that both single flight techniques give performance superior to that of the two flight technique. Actually, the comparison shown in Table X is somewhat unfair as far as the improved single flight technique is concerned. Analysis of the three techniques shows that the distance the aircraft travels between the two illuminations of a specific terrain point is quite different for each technique. For the improved single flight technique this distance is less than 1,000 feet. For the previous single flight technique this distance has a maximum value of approximately 10,000 feet. For the two flight

Table X Standard Deviations of the Reconstructed Terrain Point Coordinates for the Three Radar Techniques Using the Initially Assigned Error Standard Deviations

	Technique		
Standard Deviation of	Improved Single Flight	Previous Single Flight	Two Flight
x_r	7.66 ft.	6.44 ft.	7.05 ft.
y_r	28.40 ft.	26.00 ft.	34.00 ft.
h_r	42.70 ft.	31.20 ft.	42.70 ft.

Table XI Standard Deviations of the Reconstructed Terrain Point Coordinates for the Three Radar Techniques Using Error Standard Deviations Adjusted to Account for Differences in Distances Flown Between Terrain Point Illumination

	Technique		
Standard Deviation of	Improved Single Flight	Previous Single Flight	Two Flight
x_r	7.66 ft.	8.50 ft.	18.60 ft.
y_r	28.40 ft.	34.70 ft.	83.30 ft.
h_r	34.20 ft.	41.00 ft.	105.00 ft.

technique this distance is likely to be quite large because of the necessity of making two flights past the terrain point. For example, if a map fifteen miles long were made, then the average distance flown between illuminations would be about 100,000 feet.

Since the previous single flight and the two flight techniques have significantly (orders of magnitude) greater time between the two illuminations, the aircraft altitude and position errors and the slant ranging errors will be long-term errors and will have a larger standard deviation than those used for the improved single flight technique. For comparison purposes, it is assumed that the standard deviation of these errors is twice as large for the previous single flight technique as for the improved single flight technique, and three times as large for the two flight technique as for the improved single flight technique. The standard deviations for the reconstructed terrain point position with these assumptions are shown in Table XI. The data show that, with these assumptions, the improved single flight technique holds an edge in terms of error performance. Also, the previous single flight technique still performs considerably better than the two flight technique. The error values for the two flight technique shown in Table XI are of the same order of magnitude as the error values obtained using this technique in uncontrolled mapping experiments.[18]

Because the limiting error sources are different for the single flight techniques than for the two flight technique it is not possible to assess anything further about the comparative ability of the three techniques. This is because any assumption regarding the size of the angular errors has only a limited effect on the two flight technique while having a direct effect on the performance of the single flight techniques. Also, the aircraft position error assumptions have a direct effect on the performance of the two flight technique while having only a limited effect on the performance of the single flight techniques. Finally, without actual error data, it is difficult to quantitatively assess the effect of the difference in the distance the aircraft travels between illuminations for the three techniques. However, it is apparent that the single flight techniques will perform at least as good and very likely better than the existing two flight technique. Also, the improved single flight technique will perform at least as well and very likely better than the previous single flight technique.

VII. SUMMARY AND CONCLUSIONS

An improved single flight technique, a previously proposed single flight technique, and a previously implemented two flight technique for obtaining stereo radar image pairs are described and their performance in the presence of system errors analyzed. The analysis consists of error analyses to determine the effect of system errors on terrain point position measurement accuracy. Also, equations for determining the terrain point position from image data are analyzed for the techniques and the optimum equations are determined. The feasibility of the single flight techniques is established and a comparative analysis of the capabilities of all techniques is made.

System parameters are chosen to give the techniques the same theoretical height measuring capabilities so that the analysis may be used to give unbiased results. The system parameters and the resulting image parameters for each of the three stereo radar techniques are shown in Tables III, IV, and V.

Reconstruction equations are derived for each of the three stereo radar techniques. A computer simulation is developed to determine the image coordinate variation for the improved single flight technique. The sensitivity of the reconstructed terrain point coordinates using each of the reconstruction equations are determined using the results from this simulation. Using the assumed error values the

optimum (least sensitive to system errors) set of reconstruction equations for the improved single flight technique is determined. Since the previous single flight technique geometry and reconstruction are very similar to that of the improved single flight technique, the optimum reconstruction equations are the same. The optimum reconstruction equations for the two flight technique are readily available since there is but one solution for the terrain point cross-track position and height, and the along-track position has two similar but independent solutions which can readily be combined.

The error analysis for the stereo radar techniques considers aircraft attitude and position errors, ranging errors, image position errors, and conical beam cone angle error. The average sensitivities to these errors for each of the three stereo radar techniques are shown in Tables VII, VIII, and IX. The standard deviations for the errors are assigned to be: angular errors 0.01 degree, aircraft position errors one foot, and image position and ranging errors five feet. These values can be obtained using present day state-of-the-art stabilizing and sensing equipment. The resulting standard deviations of the terrain point coordinate errors for the three techniques are given in Table X. The errors of the single flight techniques are compatible with the theoretical capabilities of the two systems. This indicates that the systems are feasible and the initially assigned error magnitudes are approximately the stabilization and

position accuracies required to efficiently implement these proposed techniques.

Comparison of the error performance of the three techniques indicates that the previous single flight technique performs slightly better than the improved single flight technique and that both single flight techniques perform better than the two flight technique. However, these comparisons are somewhat unfair as far as the improved single flight technique is concerned since the distance traveled between obtaining the two images is much greater for the other techniques. To assess this effect, the aircraft attitude and position errors and ranging errors are increased by factors of two and three for the previous single flight technique and the two flight technique respectively. The resulting terrain point coordinate error standard deviations are given in Table XI. This error data indicates that the improved single flight technique is best in terms of error performance and the both single flight techniques show a large improvement over the two flight technique. Even if these assumed error ratios are too large, it is apparent that the improved single flight technique provides error performance which is at least as good as the previous single flight technique and the single flight techniques perform at least as good as the existing two flight technique.

In conclusion, the improved single flight and the previously proposed single flight techniques are feasible in that they could be implemented using present day state-

of-the-art sensors and stabilization equipment. The improved single flight technique gives the best error performance and both single flight techniques perform better than the existing two flight technique.

BIBLIOGRAPHY

1. Thompson, Morris M., ed. Manual of Photogrammetry, 3d ed. Falls Church, Va.: Society of Photogrammetry, 1966.

2. Thomas R. Beveridge, Frank C. Whaley, and Lawrence E. Lamelet, Topographic Maps of Missouri. Rolla, Mo.: Missouri State Geological Survey, 1957.

3. Crandall, Clifford J. "Radar Mapping in Panama," Photogrammetric Engineering, 35, (July, 1969), 641-646.

4. Col. M. V. Jonah and C. DiCarlo, "DOD Data Processing Equipment for Radar," Proceedings of ACSM-ASP Technical Conference, Denver, Colorado, (October, 1970)

5. McCoy, Roger M. "Drainage Network Analysis with K-Band Radar Imagery," Geolographical Review, 59, (October,1969), 493-512.

6. LaPrade, G. L. "An Analytic and Experimental Study of Stereo for Radar," Photogrammetric Engineering, 29, (March, 1963), 294-300.

7. Advertising Literature. Goodyear Aerospace Corporation, Litchfield Park, Arizona.

8. Advertising Literature. Westinghouse Aerospace Corporation. Baltimore, Maryland.

9. Carlson, Gordon E. "An Improved Single Flight Technique for Radar Stereo," IEEE Transactions on Geoscience Electronics, GE-11, 4, (October, 1973).

10. Gordon E. Carlson and George L. Bair, "Single Flight Radar Using a Mechanically Slewed Array and an Electrically Squinted Array," University of Mo.-Rolla Electrical Engineering Communication Sciences Report, CSR-73-5, (AD-771434), (Nov., 1973).

11. Gordon E. Carlson and George L. Bair, "Comparative Evaluation of an Improved Single Flight Stereo Radar Technique," University of Mo.-Rolla Electrical Engineering Communication Sciences Report, CSR-74-1, (AD-774762), (Feb., 1974).

12. Skolnik, M. I. Introduction to Radar Systems. New York: mcGraw-Hill, 1962.

13. Skolnik, M. I. Radar Handbook. New York: McGraw-Hill, 1970.

Bibliography (Continued)

14. Levine, Daniel, Radargrammetry. New York: McGraw-Hill, 1960.

15. Moore, R. K. "Imaging Radars for Geoscience Use," IEEE Transactions on Geoscience Electronics, GE-9, 3, (July, 1971), 155-164.

16. Carlson, Gordon E. "Topographic Earth Observations Using Radar Techniques with a Single Flight," IEEE 1972 NTC Record, (December, 1972), 14D-1-14D-6.

17. Chastant, Lloyd. Telephone conversation with Dr. Gordon E. Carlson. June 4, 1973.

18. Graham, Lee. Telephone conversation with Dr. Gordon E. Carlson. July 26, 1973.

VITA

George L. Bair, Jr. was born on December 18, 1948 in Springfield, Missouri. He received his primary and secondary education in Springfield, Missouri. From June 1968 to June 1970 he served with the United States Navy in the Western Pacific. He has received his college education from Southwest Missouri State University, Springfield, Missouri and the University of Missouri-Rolla, Rolla, Missouri and received the Bachelor of Science in Electrical Engineering from the University of Missouri-Rolla in May 1973.

Since June 1973 he has been enrolled in the Graduate School of the University of Missouri-Rolla and has held the Chancellor's Fellowship for the period August 1973 to June 1974.

APPENDIX

COMPUTER PROGRAM LISTINGS

The computer program described here is a combination of the two programs used in the error analysis and described by the flow charts in Figs. 48 and 54. It is capable of computing image coordinate sensitivities and also the reconstructed terrain point coordinate sensitivities. The program consists of a main body which performs basic routing and input-output operations and several subroutines which perform the error definition, error equation calculations, and reconstruction.

Definitions and explanations of the variables used in the program follow:

H - aircraft altitude, feet.

IND - integer indicating the error being used.

NUMBR - number of error values to be used.

NOCT - number of terrain points used across the track.

NOTAL - number of terrain point altitudes to be used.

PHI2 - conical beam cone angle, degrees.

TAL - terrain point altitude, feet.

SWAW - swath width, feet.

SWIN - distance from flight track to inside edge of the swath, feet.

SWOUT - distance from flight track to outside edge of the swath, feet.

XO, YO, HO - true terrain point position, feet.

X1O, Y1O, X2O, Y2O - true image coordinates, feet.

X1, Y1, X2, Y2 - image coordinates with error, feet.

XR, YR, HR - reconstructed terrain point coordinates, feet.

DELYA1, DELHA1 - aircraft position errors for the illumination #1, feet.

DELR1, DELR2 - slant ranging errors, feet.

DELXI1, DELYI1 - imaging errors for the illumination #1, feet.

DELYA2, DELHA2 - aircraft position errors for the illumination #2, feet.

DELPI2 - conical beam cone angle error, degrees.

DELXI2, DELYI2 - imaging errors for the illumination #2, feet.

TETR1, TETP1, TETY1 - angular errors for the illumination #1, degrees.

TETR2, TETP2, TETY2 - angular errors for the illumination #2, degrees.

SENSX1, SENSY1, SENSX2, SENSY2 - image coordinate sensitivities, feet.

SENSX, SENSY, SENSH - reconstructed terrain point coordinate sensitivities, feet/feet or feet/degree.

The main body and error increment subroutine are common to the computer programs used to generate the error sensitivities for all three radar techniques. They are listed in Fig. 64. The main body performs the input-output operations, incrementation of the terrain point height and cross-track position, and basic routing. The error increment subroutine performs error definition, identification, and incrementation.

The subroutines specific to each of the three radar techniques are listed in Figs. 65, 66, and 67. Subroutine Beam 1 performs the calculation of the image coordinates including the effect of error for illumination 1. Subroutine

Beam 2 performs the calculation of the image coordinates including the effect of error for illumination 2. The subroutine Recon performs the reconstruction of the terrain point position and calculates the sensitivities.

A simplified sample output of the computer program (for the improved single flight technique) is shown in Fig. 68. Only the reconstructed terrain point sensitivities are shown for simplicity. The programs listed also output the image coordinate sensitivities in a similar manner. The outputs of the computer programs for the other techniques are identical except that the image coordinate sensitivities are not calculated. Note that since the main body is common to all computer programs and contains a provision for printing out the image coordinate sensitivities, the outputs for the previous single flight and two flight techniques will contain some type of output for the sensitivities unless revised. These sensitivities are not to be mistaken for meaningful data.

```
C      ERROR ANALYSIS MAIN DRIVE
       IMPLICIT REAL*8 (A-H,O-Z)
       COMMON /SUBR/ SWAW,SWOUT,SWIN,ERROR,X1,Y1,X2,Y2,XR,YR,
      1    HR,X1O,Y1O,Y2O,SENSX,SENSY,SENSH,SENSX1,SENSY1,
      2    SENSX2,SENSY2
       COMMON /ILLUM1/ TETR1,TETP1,TETY1,DELXI1,DELYI1,DELYA1,
      1    DELHA1,DELR1,TET1
       COMMON /ILLUM2/ TETR2,TETP2,TETY2,DELXI2,DELYI2,DELYA2,
      1    DELHA2,DELR2,DELPI2,TET2
       NAMELIST /INPUT/ TET1,TET2,TETR2,TETR1,TETP2,TETP1,
      1    TETY2,TETY1,IND,H,DELHA2,DELHA1,DELXI2,DELXI1,DELYI1,
      2    DELYI2,NUMBR,SIZE,NOCT,TAL,NOTAL,SIZTAL,DELYA2,DELYA1,
      3    DELPI2,DELR2,DELR1,PHI2,SWOUT,SWIN,SWAW
    1  READ(1,INPUT,END=5)
       TET1R=TET1/57.29578
       TET2R=TET2/57.29578
       PHI2R=PHI2/57.29578
       WRITE(3,100) TET1,TET2,TETR2,TETR1,TETP2,TETP1,TETY2,
      1    TETY1,IND,H,DELYA2,DELYA1
  100  FORMAT(1HO/16X,4HTET1,5X,4HTET2,5X,5HTETR2,5X,5HTETR1,
      1    6X,4HAALT,4X,6HDELYA2,4X,DELYA1/1H ,10X,8F10.2,I10,3F10.2)
       WRITE(3,101) DELHA2,DELHA1,DELXI2,DELXI1,DELYI2,DELYI1,
      1    NUMBR,SIZE,NOCT,TAL,NOTAL,SIZTAL,DELPI2
  101  FORMAT(1H0//4X,6HDELHA2,4X,6HDELHA1,4X,6HDELXI2,4X,
      1    6HDELXI1,4X,6HDELYI2,4X,6HDELYI1,5X,5HNUMBR,6X,4HSIZE,
      2    6X,4HNOCT,7X,4HTAL,5X,5HNOTAL,4X,6HSIZTAL,4X,
      3    6HDELPI2,4X/1H ,6F10.2,I10,F10.2,I10,F10.2,I10,2F10.2)
       WRITE(3,102) H,SWOUT,SWIN,SWAW,TET1,TET2,PHI2,DELR2,DELR1
  102  FORMAT(1H0//28X,4HAALT,7X,5HSWOUT,8X,4HSWIN,8X,4HSWAW,
      1    8X,4HTET1,6X,4HTET2,6X,6HDELPI2,5X,5HDELR2,5X,5HDELR1/
      2    1H ,20X,8F12.2,2F10.2)
       Do 2 K=1,NUMBR
       HINC=SIZE
C      ERROR INCREMENTATION
       CALL ERRINC(IND,HINC)
C      TERRAIN POINT HEIGHT INCREMENTATION
       NO=NOTAL+1
       DO 3 J=1,NO
       HO=TAL+(J-1)*SIZTAL
       WRITE(3,103)
  103  FORMAT(1H0/ ,31HORIGINAL TERRAIN POINT LOCATION,7X,33H
      1    TERRAIN POINT LOCATION WITH ERROR,11X,13HSENSITIVITIES/
      2    1H ,8X,14X,1HY,8X,1HH,17X,1HX,8X,1HY,4X,1HH,17X,
      3    6HSENSX2,3X,6HSENSY2,3X,6HSENSX1,3X,6HSENSY1)
C      TERRAIN POINT CROSS-TRACK POSITION INCREMENTATION
       INCRY=SWAW/(NOCT-1)
       DO 4 I=1,NOCT
       XO=0.0
```

Fig. 64. Listing of the Main Body and Error Increment Subroutine Which are Common to All Computer Programs

```
      YO=SWOUT-(I-1)*INCRY
C     COMPUTATION OF THE RECONSTRUCTED TERRAIN POINT POSITION
      CALL BEAM2(YO,PHI2R,HO,H)
      CALL BEAM1(TETR1,YO,HO,H)
      CALL RECON(TET1R,H,XO,YO,HO)
      WRITE(3,104) YO,HO,XR,YR,HR,SENSX,SENSY,SENSH,SENSX2,
     1   SENSY2,SENSX1,SENSY1
  104 FORMAT(F10.2,F7.1,3F9.1,7F9.2)
    4 CONTINUE
    3 CONTINUE
    2 CONTINUE
      GO TO 1
    5 STOP
      END


      SUBROUTINE ERRINC(IND,HINC)
      IMPLICIT REAL*8 (A-H,O-Z)
      COMMON /SUBR/
      COMMON /ILLUM1/
      COMMON /ILLUM2/
  101 FORMAT(1H0///30X,6HERROR:,2X,1A8,F10.2)
      DIMENSION ERRORS(17)
      DATA ERRORS/'TETR2','TETR1','TETP2','TETP1','TETY2',
     1   'TETY1','DELHA2','DELHA1','DELXI2','DELXI1','DELYI2'
     2   'DELYI1','DELYA2','DELYA1','DELPI2','DELR2','DELR1'/
      GO TO (1,2,3,4,5,6,7,8,9,10,11,12,13,14,15,16,17),IND
    1 TETR2=TETR2+HINC
      WRITE(3,101) ERRORS(1),TETR2
      ERROR=TETR2
      GO TO 130
    2 TETR1=TETR1+HINC
      WRITE(3,101) ERRORS(2),TETR1
      ERROR=TETR1
      GO TO 130
    3 TETP2=TETP2+HINC
      WRITE(3,101) ERRORS(3),TETP2
      ERROR=TETP2
      GO TO 130
    4 TETP1=TETP1+HINC
      WRITE(3,101) ERRORS(4),TETP1
      ERROR=TETP1
      GO TO 130
    5 TETY2=TETY2+HINC
      WRITE(3,101) ERRORS(5),TETY2
      ERROR=TETY2
      GO TO 130
    6 TETY1=TETY1+HINC
      WRITE(3,101) ERRORS(6),TETY1
      ERROR=TETY1
```

Fig. 64 (Continued)

```
      GO TO 130
    7 DELHA2=DELHA2+HINC
      WRITE(3,101) ERRORS(7),DELHA2
      ERROR=DELHA2
      GO TO 130
    8 DELHA1=DELHA1+HINC
      WRITE(3,101) ERRORS(8),DELHA1
      ERROR=DELHA1
      GO TO 130
    9 DELXI2=DELXI2+HINC
      WRITE(3,101) ERRORS(9),DELXI2
      ERROR=DELXI2
      GO TO 130
   10 DELXI1=DELXI1+HINC
      WRITE(3,101) ERRORS(10),DELXI1
      ERROR=DELXI1
      GO TO 130
   11 DELYI2=DELYI2+HINC
      WRITE(3,101) ERRORS(11),DELYI2
      ERROR=DELYI2
      GO TO 130
   12 DELYI1=DELYI1+HINC
      WRITE(3,101) ERRORS(12),DELYI1
      ERROR=DELYI1
      GO TO 130
   13 DELYA2=DELYA2+HINC
      WRITE(3,101) ERRORS(13),DELYA2
      ERROR=DELYA2
      GO TO 130
   14 DELYA1=DELYA1+HINC
      WRITE(3,101) ERRORS(14),DELYA1
      ERROR=DELYA1
      GO TO 130
   15 DELPI2=DELPI2+HINC
      WRITE(3,101) ERRORS(15),DELPI2
      ERROR=DELPI2
      GO TO 130
   16 DELR2=DELR2+HINC
      WRITE(3,101) ERRORS(16),DELR2
      ERROR=DELR2
      GO TO 130
   17 DELR1=DELR1+HINC
      WRITE(3,101) ERRORS(17),DELR1
      ERROR=DELR1
  130 RETURN
      END
```

Fig. 64 (Continued)

```
      SUBROUTINE BEAM1(TET1R,YO,H,HO)
      IMPLICIT REAL*8 (A-H,O-Z)
      COMMON /SUBR/
      COMMON /ILLUM1/
      TETR1R=TETR1/57.29578
      TETP1R=TETP1/57.29578
      TETY1R=TETY1/57.29578
      YM=YO-DELYA1
      PX=DSIN(TETP1R)
      PY=-DSIN(TETR1R)
      PZ=DCOS(TETP1R)*DCOS(TETR1R)
      BX=DCOS(TETY1R)*DCOS(TETP1R)*DCOS(TET1R)-DSIN(TET1R)*
     1    DSIN(TETY1R)
      BY=DCOS(TET1R)*DSIN(TETY1R)+DSIN(TET1R)*DCOS(TETR1R)*
     2    DCOS(TETY1R)
      BZ=-DCOS(TET1R)*DSIN(TETP1R)+DSIN(TET1R)*DSIN(TETR1R)
      OM=PY*BZ-BY*PZ
      Q=H+DELHA1
      HXM=(YM*(BX*PZ-PX*BZ)+(Q-HO)*(PX*BY-PY*BX))/OM
      R=(YM*BZ-BY*(Q-HO))/OM
      S=(PY*(Q-HO)-YM*PZ)/OM
      SLRM=DSQRT(R**2+S**2)+DELR1
      RRM=DSQRT(SLRM**2-H**2)
      X1=HXM+RRM*DCOS(TET1R)+DELXI1
      Y1=RRM*DSIN(TET1R)+DELYI1
      DELRM=-YO/DSIN(TET1R)+DSQRT((YO/DSIN(TET1R))**2+HO**2-
     1    2.0*H*HO)
      Y1O=YO+DELRM*DSIN(TET1R)
      X1O=DELRM*DCOS(TET1R)
      RETURN
      END


      SUBROUTINE BEAM2(YO,PHI2R,HO,H
      IMPLICIT REAL*8 (A-H,O-Z)
      COMMON /SUBR/
      COMMON /ILLUM2/
      TETR2R=TETR2/57.29578
      TETP2R=TETP2/57.29578
      TETY2R=TETY2/57.29578
      Y2O=DSQRT(YO**2-2*H*HO**2)
      Q=H+DELHA2
      YE=YO-DELYA2
      AE=(DCOS(TETY2R)**2)*(DCOS(TETP2R)**2)-DCOS(PHI2R)**2
      IF(TETP2R.NE.0.0) GO TO 1000
      AD=(YE**2)*DSIN(PHI2R)**2+((Q-HO)**2*(DCOS(TETY2R)**2-
     1    DCOS(PHI2R)**2)
      HXE=(YE*DSIN(TETY2R)*DCOS(TETY2R)-DCOS(PHI2R)*DSQRT(AD))/AE
      PN=-HXE*DCOS(TETY2R)+YE*DSIN(TETY2R)
      RRE=DSQRT((PN**2)*DTAN(PHI2R)**2-Q**2)
```

Fig. 65 Listing of the Subroutines Used for the Improved Single Flight Technique Computer Programs

```
      GO TO 1100
1000  AD=(YE**2)*(DCOS(TETR2R)**2-DCOS(PHI2R)**2)+((Q-HO)**2)*
     1    DSIN(PHI2R)**2
      HXE=((HO-Q)*DSIN(TETP2R)*DCOS(TETP2R)-DCOS(PHI2R)*DSQRT(AD))/
     1    AE
      PN=DCOS(PHI2R)*DSQRT((Q-HO)**2+YE**2+HXE**2)
      RRE=DSQRT(((Q-HO)/DCOS(TETP2R)+PN*DTAN(TETP2R))**2+
     1    YE**2-Q**2)
1100  CONTINUE
      IF(DELYA2.NE.0.0) GO TO 2
      IF(DELHA2.NE.0.0) GO TO 2
      IF(DELPI2.NE.0.0) GO TO 2
      IF(DELR2.NE.0.0) GO TO 2
      X2=HXE+PN+DELXI2
      Y2=RRE+DELYI2
      GO TO 3
    2 PHIRR=PHI2R+DELPI2/57.29578
      RB=DSQRT(YE**2+(Q-HO)**2)
      SR=RB/DSIN(PHIRR)+DELR2
      HXE=-RB/DTAN(PHIRR)
      X2=HXE+SR*DCOS(PHI2R)
      Y2=DSQRT((SR**2)*(DSIN(PHI2R)**2)-H**2)
    3 RETURN
      END


      SUBROUTINE RECON(TET1R,H,XO,YO,HO)
      IMPLICIT REAL*8 (A-H,O-Z)
      COMMON /SUBR/
      XR=X2
      YR=Y1+(X2-X1)*DTAN(TET1R)
      DELRE=Y2-YR
      HR=H-DSQRT(H**2+DELRE*(2*YR+DELRE))
      IF(ERROR.NE.0.0) GO TO 1
      SENSX=0.0
      SENSY=0.0
      SENSH=0.0
      SENSX1=0.0
      SENSX2=0.0
      SENSY1=0.0
      SENSY2=0.0
      GO TO 2
    1 SENSX=(XR-XO)/ERROR
      SENSY=(YR-YO)/ERROR
      SENSH=(HR-HO)/ERROR
      SENSX1=(X1-X10)/ERROR
      SENSX2=X2/ERROR
      SENSY1=(Y1-Y10)/ERROR
      SENSY2=(Y2-Y20)/ERROR
    2 RETURN
      END
```

Fig. 65 (Continued)

```
      SUBROUTINE BEAM1(TET1R,YO,H,HO)
      IMPLICIT REAL*8 (A-H,O-Z)
      COMMON /SUBR/
      COMMON /ILLUM1/
      TETR1R=TETR1/57.29578
      TETP1R=TETP1/57.29578
      TETY1R=TETY1/57.29578
      YM=YO-DELYA1
      PX=DSIN(TETP1R)
      PY=-DSIN(TETR1R)
      PZ=DCOS(TETP1R)*DCOS(TETR1R)
      BX=DCOS(TETY1R)*DCOS(TETP1R)*DCOS(TET1R)-DSIN(TET1R)*
     1   DSIN(TETY1R)
      BY=DCOS(TET1R)*DSIN(TETY1R)+DSIN(TET1R)*DCOS(TETR1R)*
     1   DCOS(TETY1R)
      BZ=-DCOS(TET1R)*DSIN(TETP1R)+DSIN(TET1R)*DSIN(TETR1R)
      OM=PY*BZ-BY*PZ
      Q=H+DELHA1
      HXM=(YM*(BX*PZ-PX*BZ)+(Q-HO)*(PX*BY-PY*BX))/OM
      R=(YM*BZ-BY*(Q-HO))/OM
      S=(PY*(Q-HO)-YM*PZ)/OM
      SLRM=DSQRT(R**2+S**2)+DELR1
      RRM=DSQRT(SLRM**2-H**2)
      X1=HXM+RRM*DCOS(TET1R)+DELXI1
      Y1=RRM*DSIN(TET1R)+DELYI1
      RETURN
      END


      SUBROUTINE BEAM2(YO,TET2R,HO,H)
      IMPLICIT REAL*8 (A-H,O-Z)
      COMMON /SUBR/
      COMMON /ILLUM2/
      TETR2R=TETR2/57.29578
      TETP2R=TETP2/57.29578
      TETY2R=TETY2/57.29578
      Q=H+DELHA2
      YE=YO-DELYA2
      PX=DSIN(TETP2R)
      PY=-DSIN(TETR2R)
      PZ=DCOS(TETP2R)*DCOS(TETR2R)
      BX=-DSIN(TETY2R)
      BY=DCOS(TETR2R)*DCOS(TETY2R)
      BZ=DSIN(TETR2R)
      OM=PY*BZ-BY*PZ
      HXM=(YE*(BX*PZ-PX*BZ)+(Q-HO)*(PX*BY-PY*BX))/OM
      R=(YE*BZ-BY*(Q-HO))/OM
      S=(PY*(Q-HO)-YE*PZ)/OM
      SLRE=DSQRT(R**2+S**2)+DELR2
      RRM=DSQRT(SLRE**2-H**2)
```

Fig. 66 Listing of the Subroutines Used for the Previous Single Flight Technique Computer Program

```
      X2=HXM+DELXI2
      Y2=RRM+DELYI2
      RETURN
      END


      SUBROUTINE RECON(TET1R,H,XO,YO,HO)
      IMPLICIT REAL*8 (A-H,O-Z)
      COMMON /SUBR/
      XR=X2
      YR=Y1+(Y2-Y1)*DTAN(TET1R)
      DELRE=Y2-YR
      DELRM=(X1-XR)/DCOS(TET1R)
      HR=H-DSQRT(H**2+DELRE*(2*YR+DELRE))
      IF(ERROR.NE.0.0) GO TO 1
      SENSX=0.0
      SENSY=0.0
      SENSH=0.0
      GO TO 2
    1 SENSX=(XR-XO)/ERROR
      SENSY=(YR-YO)/ERROR
      SENSH=(HR-HO)/ERROR
    2 CONTINUE
      RETURN
      END
```

Fig. 66 (Continued)

```
      SUBROUTINE BEAM1(YO,H,HO)
      IMPLICIT REAL*8 (A-H,O-Z)
      COMMON /SUBR/
      COMMON /ILLUM1/
      TETR1R=TETR1/57.29578
      TETP1R=TETP1/57.29578
      TETY1R=TETY1/57.29578
      YM=YO-DELYA1
      PX=DSIN(TETP1R)
      PY=-DSIN(TETR1R)
      PZ=DCOS(TETP1R)*DCOS(TETR1R)
      BX=-DSIN(TETY1R)
      BY=DCOS(TETR1R)*DCOS(TETY1R)
      BZ=DSIN(TETR1R)
      OM=PY*BZ-BY*PZ
      Q=H+DELHA1
      HXM=(YM*(BX*PZ-PX*BZ)+Q-HO)*(PX*BY-PY*BX))/OM
      R=(YM*BZ-BY*(Q-HO))/OM
      S=(PY*(Q-HO)-YM*PZ)/OM
      SLRM=DSQRT(R**2+S**2)+DELR1
      RRM=DSQRT(SLRM**2-H**2)
      X1=HXM+DELXI1
      Y1=RRM+DELYI1
      RETURN
      END


      SUBROUTINE BEAM2(YO,HO,H)
      IMPLICIT REAL*8 (A-H,O-Z)
      COMMON /SUBR/
      COMMON /ILLUM2/
      TETR2R=TETR2/57.29578
      TETP2R=TETP2/57.29578
      TETY2R=TETY2/57.29578
      Q=H+DELHA2
      YE=YO-DELYA2+SWAW
      PX=DSIN(TETP2R)
      PY=-DSIN(TETR2R)
      PZ=DCOS(TETP2R)*DCOS(TETR2R)
      BX=-DSIN(TETY2R)
      BY=DCOS(TETR2R)*DCOS(TETY2R)
      BZ=DSIN(TETR2R)
      OM=PY*BZ-BY*PZ
      HXM=(YE*(BX*PZ-PX*BZ)+(Q-HO)*(PX*BY-PY*BX))/OM
      R=(YE*BZ-BY*(Q-HO))/OM
      S=(PY*(Q-HO)-YE*PZ)/OM
      SLRE=DSQRT(R**2+S**2)+DELR2
      RRM=DSQRT(SLRE**2-H**2)
      X2=HXM+DELXI2
```

Fig. 67 Listing of the Subroutines Used for the Two Flight Technique Computer Program

```
      Y2=RRM+DELYI2-SWAW
      RETURN
      END


      SUBROUTINE RECON(H,XO,YO,HO)
      IMPLICIT REAL*8(A-H,O-Z)
      COMMON /SUBR/
      XR=(X2+X1)/2.0
      YR=(Y1**2-Y2**2+2*Y1*SWAW)/(2*SWAW)
      HR=H-DSQRT(H**2+Y2**2-YR**2)
      IF(ERROR.NE.0.0) GO TO 1
      SENSX=0.0
      SENSY=0.0
      SENSH=0.0
      GO TO 2
    1 SENSX=(XR-XO)/ERROR
      SENSY=(YR-YO)/ERROR
      SENSH=(HR-HO)/ERROR
    2 CONTINUE
      RETURN
      END
```

Fig. 67 (Continued)

TET1	TET2	TETR2	TETR1	TETP2	TETP1	TETY2	TETY1	IND	AALT	DELYA2	DELYA1
70.0	****	0.0	0.0	0.0	0.0	0.0	0.0	2	15000.0	0.0	0.0

DELHA2	DELHA1	DELXI2	DELXI1	DELYI2	DELYI1	NUMBR	SIZE	NOCT	TAL	NOTAL	SIZTAL
0.0	0.0	0.0	0.0	0.0	0.0	10	0.01	5	0.0	5	50.00

AALT	SWOUT	SWIN	SWAW	TET1	PHI2
15000.00	21804.67	11609.80	10194.87	70.00	75.63

ERROR: TETR1

ORIGINAL TERRAIN POINT LOCATION			TERRAIN POINT LOCATION WITH ERROR			SENSITIVITIES		
X	Y	H	X	Y	H	X	Y	H
0.0	21804.67	0.0	0.0	21807.29	3.81	0.0	261.77	380.59
0.0	19256.67	0.0	0.0	19259.29	3.36	0.0	261.77	336.12
0.0	16708.67	0.0	0.0	16711.29	2.92	0.0	261.77	291.64
0.0	14160.67	0.0	0.0	14163.29	2.47	0.0	261.77	247.17
0.0	11612.67	0.0	0.0	11615.29	2.03	0.0	261.77	202.70

ORIGINAL TERRAIN POINT LOCATION			TERRAIN POINT LOCATION WITH ERROR			SENSITIVITIES		
X	Y	H	X	Y	H	X	Y	H
0.0	21804.67	50.0	0.0	21807.28	53.81	0.0	260.89	380.59
0.0	19256.67	50.0	0.0	19259.28	53.36	0.0	260.90	336.12
0.0	16708.67	50.0	0.0	16711.28	52.92	0.0	260.90	291.64
0.0	14160.67	50.0	0.0	14163.28	52.47	0.0	260.90	247.17
0.0	11612.67	50.0	0.0	11615.28	52.03	0.0	260.90	202.70

ORIGINAL TERRAIN POINT LOCATION			TERRAIN POINT LOCATION WITH ERROR			SENSITIVITIES		
X	Y	H	X	Y	H	X	Y	H
0.0	21804.67	100.0	0.0	21807.27	103.81	0.0	260.02	380.59
0.0	19256.67	100.0	0.0	19259.27	103.36	0.0	260.02	336.11
0.0	16708.67	100.0	0.0	16711.28	102.92	0.0	260.03	291.64

Fig. 68 Sample Output of the Error Analysis Computer Program